GRAIN BOUNDARY MOBILITY AND SEGREGATION IN NON-STOICHIOMETRIC SOLID SOLUTIONS OF MAGNESIUM ALUMINATE SPINEL

by

Yet-Ming Chiang
S. B., Massachusetts Institute of Technology
(1980)

SUBMITTED IN PARTIAL FULFILLMENT
OF THE REQUIREMENTS FOR THE
DEGREE OF

DOCTOR OF SCIENCE

at the

MASSACHUSETTS INSTITUTE OF TECHNOLOGY

JANUARY 11, 1985

Signature of Author_____
Department of Materials Science and Engineering
January 11, 1985

Certified by_____
W. D. Kingery
Thesis Supervisor

Accepted by_____
B. J. Wuensch
Chairman, Departmental Committee on Graduate Students

GRAIN BOUNDARY MOBILITY AND SEGREGATION IN NON-STOICHIOMETRIC SOLID SOLUTIONS OF MAGNESIUM ALUMINATE SPINEL

by

YET-MING CHIANG

Submitted to the Department of Materials Science and Engineering on January 11, 1985 in partial fulfillment of the requirements for the degree of Doctor of Science

ABSTRACT

The grain boundary mobility in dense single phase magnesium aluminate spinel of magnesia-excess, nearly stoichiometric, and alumina-excess compositions has been measured from normal grain growth in hot-pressed samples. Grain boundary compositions as a function of stoichiometry have also been measured, using scanning transmission electron microscopy (STEM), and the variation in mobility with stoichiometry and boundary composition is interpreted using a defect structure model developed from the literature.

At constant temperature between 1400° and 1800°C, the boundary mobility in magnesia rich spinel is 10^2 to 10^3 greater than that in nearly stoichiometric or alumina rich compositions. The greater mobility of magnesia rich spinel persists across the magnesia-excess portion of the spinel single phase field. On the alumina rich side, the mobility increases slightly and then decreases again with increasing alumina excess, the total variation being less than a factor of five up to compositions of $n = Al_2O_3/MgO = 1.56$.

The boundary mobility in magnesia rich (n=0.957) spinel as a function of temperature from 1450° to 1700°C is (in units of $cm^4/erg.sec$):

$$\ln M_b = -[8.96\ (+/-1.37)] - [3.02\ (+/-0.78)eV/kT]$$

The mobility in a nearly stoichiometric (n=1.013) composition in the temperature range 1250° to 1650°C is:

$$\ln M_b = -[6.05\ (+/-0.67)] - [4.37\ (+/-0.10)eV/kT]$$

and that in an alumina rich (n=1.56) spinel from 1500° to

1700°C is:

$$\ln M_b = -[17.93(+/-1.88)] - [2.57\ (+/-0.30)eV/kT]$$

A striking feature of grain boundary mobilities in nearly stoichiometric compositions is the good agreement, within a factor of 5 at temperatures in the range 1400° to 1800°C, amongst several sources of literature data and the present measurements. Such reproducibility of grain boundary mobility measurements has not been reported for any other ionic systems.

The lattice defect structure of nearly stoichiometric spinel is dominated by cation inversion, with secondary defects being cation Frenkel pairs. Analysis of literature data shows that aluminum Frenkel pairs are more abundant than magnesium Frenkel pairs at low temperatures. Excess alumina is accomodated by aluminium substituting on magnesium sites, compensated by cation vacancies for charge neutrality. Excess magnesia is accomodated by magnesium substituting for aluminum ions, compensated by cation interstitials.

STEM measurements of grain boundary compositions in the above samples show Ca and Si segregation in minor amounts which do not vary systematically with sample stoichiometry. The impurity segregation has been quantified using forsterite and calcium aluminate standards to correspond to at most 0.20 monolayers of each segregant at the boundary. More significantly, an increase in the Al/Mg ratio is found at all boundaries regardless of sample stoichiometry. This grain boundary concentration change is greater than the impurity segregation and varies with stoichiometry, being least in magnesia rich spinels (≈0.7 equivalent monolayers of excess Al) and increases with the alumina content to ≈1.5 equivalent monolayers in the n=1.56 sample.

The increase in Al/Mg ratio at grain boundaries is a consequence of both segregation of positive defect species and repulsion of negative ones in the space charge, but corresponds to a negative grain boundary charge in all compositions. The potential difference between grain boundary and bulk is estimated to be about 0.25 V. Cation interstitials are expected to segregate strongly in magnesia rich spinel, and the increase in Al is interpreted as resulting predominantly from high concentrations of $Al_i^{\bullet\bullet\bullet}$ species. These defects have a much higher diffusivity compared to the substitutional aluminum defect which is believed to segregate in stoichiometric and alumina rich compositions, $Al_{Mg}^{\bullet}$, and hence the magnesia rich spinel has a correspondingly greater boundary mobility. With increasing alumina excess in the alumina rich compositions, boundary

drag from $Al_{Mg}^{\bullet}$ decreases as the diffusivity is increased from addition of cation vacancies, but this effect is counterbalanced by increased $Al_{Mg}^{\bullet}$ segregation.

In all stoichiometries the concentration of host cation defects is large enough to dominate both the lattice defect structure and solute drag in reasonably pure materials, thereby accounting for the impurity tolerant behavior of magnesium aluminate.

Thesis Supervisor: W. D. Kingery
Professor of Ceramics

TABLE OF CONTENTS

LIST OF FIGURES

LIST OF TABLES

Acknowledgements

It is a great pleasure to thank Professor W. D. Kingery for his thoughtful guidance and generous support throughout the course of this and other research. His teaching, by example as much as by instruction, has been inspirational and has made my time here a most rewarding experience.

I am grateful also to Professor J. B. VanderSande for his enthusiastic support of my activities, dating back to my undergraduate years at MIT. Rowland M. Cannon is thanked for illuminating discussions, leaving me always with a better understanding of the complexities of the topic at hand.

There are many others to whom I am grateful for making graduate life an enjoyable and satisfying experience. Fellow students and associates, in particular Dunbar P. Birnie III, Alexana Roshko, Pam Vandiver, Roger French, Peter Moon, Patti Morris, Masayuki Fujimoto, and Todd Gattuso, have often benefited me with their insight where mine is lacking and have provided much necessary humor along the way. Roger, Peter, Patti and Dunbar are also thanked for their careful readings of drafts of this document. Pat Kearney has willingly contributed his practical knowledge and expertise, smoothing the path to progress.

Mong-Yu and Barry have my deepest appreciation for always providing the warm meal and a willing ear. Joseph Gregor deserves special thanks for a few clarifying observations at critical times and for his continuing

friendship and moral support. Finally, I am thankful to my parents for so enthusiastically supporting my continued education.

Financial support by the Department of Energy and by IBM in the form of a graduate fellowship is gratefully acknowledged. R. D. Bagley of Corning Glass Works is thanked for providing one of the samples used and for generously sharing unpublished data.

I. INTRODUCTION

Grain boundary migration participates in the sequence of kinetic processes that determine polycrystalline microstructures and, ultimately, many material properties of interest. Grain boundary mobilities in oxides, like so many other properties, are often solute controlled due to the impurity segregation phenomena that have now been shown to be pervasive in these materials (1). As modeled by Cahn(2) and Luecke and Stuewe(3), solutes that are attracted to (or repelled from) a boundary exert a viscous drag force upon the moving boundary that can be explicitly calculated if sufficient information regarding the solute diffusivity and solute-boundary interaction energies is available. In detail, ionic solids are distinct in that aliovalent solutes commonly segregate in a space charge layer adjacent to the grain boundary, as opposed to solutes with excess strain energy or chemical driving forces that adsorb in a partial monolayer at the grain boundary core as occurs in metals.

In recent years our understanding of the space charge distribution of solutes in simple ionics such as the alkali halides and MgO has advanced sufficiently in both experimental and theoretical aspects that one can conceive of examining and interpreting more complex systems, such as ternary compounds. This increased understanding combined with the ability to measure grain boundary compositions precisely with analytical tools such as the scanning

transmission electron microscope (STEM) allows a more direct examination of the relationship between grain boundary chemistry and mobility than was previously feasible. The objective of the present work is to: 1) investigate the variation of grain boundary mobility in magnesium aluminate spinel and its correlation with observed grain boundary compositions, and 2) address the relationship of grain boundary chemistry to the lattice defect structure in this ternary sytem.

There are several reasons for choosing magnesium aluminate spinel as a model system. Many of today's technologically useful ceramics, and especially those employed for their electrical, magnetic and optical properties, are oxides with at least two cation components. Ternary compounds in these categories include the ferrites, titanates and niobates. The lattice defect structures of many of these compounds have been or are being studied, and in many cases are understandably more complex than their binary counterparts, since they involve multiple ionic as well as electronic defects. Magnesium aluminate spinel is simpler in that the host cations are of fixed valence, and in addition it has been shown to be strictly an ionic conductor at high temperatures (4). Thus electronic defects need not be considered as potentially segregating defects and the segregation behavior can be treated to a large degree with existing theories for ionic space charges. While the

available information on defects in magnesium aluminate spinel cannot be considered complete, we will review what is available and also extrapolate from other systems to formulate a likely defect structure model.

An advantage in examining a non-stoichiometric system is that highly stoichiometric oxides at presently attainable purities often have multiple solutes in concentrations that are defect structure determining. The work of Glaeser (5) indicated that Al has at least 10^5 greater retarding power per atom than Mg on grain boundary motion in LiF; the existence of such large differences in solute drag increases the likelihood that background impurities at hard-to-detect levels may have a large influence. Unlike properties dependent on lattice defects, where impurity effects are to a large extent proportional to their concentration, boundary behavior can be dominated by strong segregation of very minor impurities. A ternary compound that is stable over a wide composition range allows intentional generation of much larger defect concentrations than are possible by controlled doping of a highly stoichiometric material, and the potential for overwhelming the influence of background impurities is far better.

The segregation-boundary mobility relationship in this system is of particular interest due to recent data of Uematsu et al. (6), which indicated that the 1800°C boundary mobility varies dramatically with composition, being four

orders of magnitude greater in slightly magnesia excess spinel than elsewhere. While data on other systems is scarce, it is possible that an understanding gained of the behavior in spinel may be generalized to other nonstoichiometric, ternary and higher order systems as well.

Finally, let us mention that there is recent practical interest in magnesium aluminate spinel as a first-wall and near first-wall material in fusion reactors (7,8) because of its low swelling and low strength loss when highly irradiated.

II. LITERATURE REVIEW, Part 1.

2.1 Space Charge Segregation

2.1.1 Continuum Models

Frenkel (9) first postulated the existence of a space charge region at lattice discontinuities such as surfaces, grain boundaries and dislocations in ionic solids. Earlier formulations of this problem (9,10,11) were concerned primarily with Schottky defect materials, i.e. the alkali halides. Near a grain boundary that is assumed to be an infinite source and sink for defects, the concentrations of anion and cation vacancies may differ if their respective free energies of formation differ. A charge-compensating excess of ions of one sign (or vacancies of the other) results on the boundary. In the interior of the grain, however, the vacancy concentrations are constrained by the requirement of charge neutrality, and thus a gradient in vacancy concentration exists, leading to a potential difference between the boundary and the crystal interior. At equilibrium this potential difference causes segregation or depletion of other charged defects, such as solute ions. Analogous results obtain for a defect structure dominated by Frenkel pairs, if the respective formation free energies of interstitials and vacancies differ (10,12), and in principle a space charge can exist for any system of oppositely charged defects.

The magnitude of the space charge potential is a

function of temperature and, in pure materials, the difference in formation energies of the majority defects. In aliovalently doped ionics it is in addition a function of the doping level. As an illustrative case which will also be of use later on, consider hypothetically that the dominant defect mechanism in magnesium aluminate spinel is a cation Frenkel mechanism on the aluminum sublattice. The Frenkel free energy can be formally separated into vacancy and interstitial formation energies (12):

$$F^F = F^V + F^I. \tag{2.1}$$

The free energy of defects in the crystal can be written:

$$F = \int_0^l \{n_I F^I + n_V F^V + 1/2[p(x)\bar{g}(x)]\}\, dx - TS_c \tag{2.2}$$

$$p(x) = z_I.e.n_I(x) - z_V.e.n_V(x)$$

where l is the crystal dimension (taken to be much larger than the space charge width), p(x) is the defect charge density, e the charge of an electron, z_I and z_V the effective charges and n_I and n_V the number of interstitials and vacancies respectively, $\bar{g}(x)$ is the space charge electrostatic potential (referenced to zero at the interface), and S_c the configurational entropy which is given by:

$$S_c = k \ln [N_V!N_I! / (N_V-n_V)!(N_I-n_I)!n_V!n_V!]. \tag{2.3}$$

Upon applying Stirling's approximation to the factorial terms in S_c, setting $N_V=2/3(N)$ and $N_I=3N$ where N is the number of normally occupied lattice sites in spinel, assuming dilute concentrations of defects such that n_I, $n_V \ll N$, and making a variation in the free energy, $\delta F=0$, one obtains for the mole fraction of aluminum interstitials and vacancies:

$$n_I/N = [Al_i^{\cdot\cdot\cdot}] = 3\ \exp[-F^I/kT - (3/2kT)e\underline{\phi}(x)] \qquad (2.4)$$

$$n_V/N = [V_{Al}'''] = 3/2\ \exp[-F^V/kT + (3/2kT)e\underline{\phi}(x)] \qquad (2.5)$$

since for charge neutrality far from the interface $[Al_i^{\cdot\cdot\cdot}]=[V_{Al}''']$, equating 2.4 and 2.5 the potential far from the interface is found to be a function of the difference in individual defect formation energies and temperature:

$$e\underline{\phi}(\infty) = 1/3\ [(F^V+F^I) + kT\ln 2]. \qquad (2.6)$$

Often aliovalent solutes are present in ionic solids. In spinel, an excess of alumina or magnesia can be viewed as an aliovalent solute addition; anticipating results to come in Chapter 4, excess alumina is accomodated by aluminum vacancies in concentrations that are a function of the alumina/magnesia molar ratio, n, as follows:

$$[V_{Al}'''] = (n-1)/(9n+3). \qquad (2.7)$$

Similarly, excess magnesia is accomodated by aluminum interstitials with a concentration:

$$[Al_i^{\cdot\cdot\cdot}] = (1-n)/(3n+1). \qquad (2.8)$$

For extrinsic vacancy or interstitial concentrations large compared to the thermally generated Frenkel defect concentration, Eqs. 2.4 and 2.5 still hold and the potential $\bar{\varphi}(\infty)$ can be determined if the defect formation energies are known. In Figure 2.1 is shown the potential as a function of composition in magnesium aluminate spinel at 1600°C, assuming an aluminum Frenkel mechanism to be dominant and taking $F^V = F^I = 1.5$ eV.

It is interesting to note that while the origin of the boundary charge is unique to ionics, the mathematics of the potential distribution are common with other problems such as the distribution of electronic charge in semiconductor materials (13) and of solution ions at charged particle surfaces in colloid systems (14). In each instance the potential distribution away from the charged surface is determined by solving Poisson's equation (in the one-dimensional case):

$$d^2\bar{\varphi}/dx^2 = -4\pi\, p(x)/\epsilon \qquad (2.9)$$

where ϵ is the appropriate dielectric constant, subject to the boundary conditions that the potential and its gradient go to zero far from the charged interface:

$$\bar{\varphi} = 0 \text{ and } d\bar{\varphi}/dx = 0 \text{ as } x \longrightarrow \infty. \qquad (2.10)$$

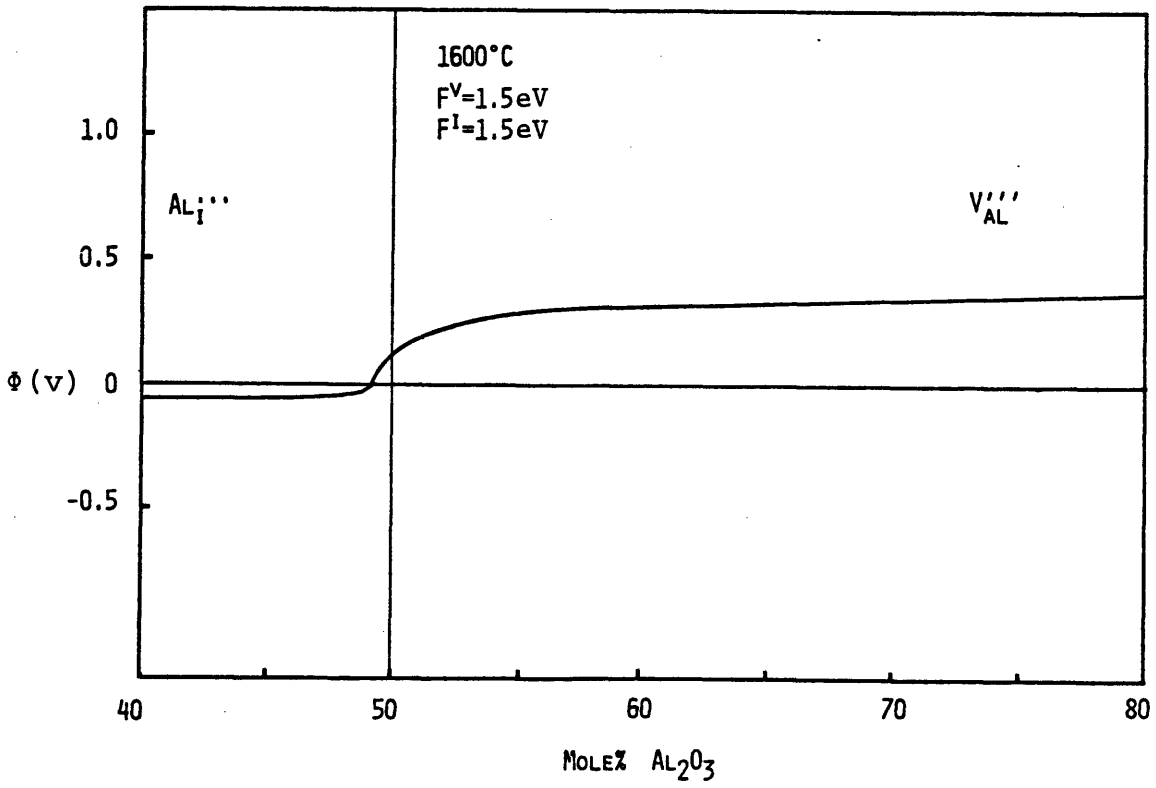

Figure 2.1 Space charge potential derived for an aluminum Frenkel defect model, as a function of spinel composition.

The charge density p(x) contains terms for the concentration of each charged species i in the system:

$$p(x) = \Sigma_i [z_i n_i(x)] \qquad (2.11)$$

where z_i is the effective charge of defect $\underline{i}$ and $n_i(x)$ is the defect concentration. The concentration of each charged defect varies with the electrostatic potential in the space charge according to a Boltzmann distribution function as in Eq. 2.4 and 2.5. The increasing complexity in successive renderings of this problem for ionic solids have resulted partly from consideration of more complex systems of defects, including defect associates that may form. It is simpler to consider a pure or singly doped alkali halide than a binary oxide with multiple solutes for which dimers, trimers, and defect clusters may exist. Analytic solutions to Poisson's equation (Eq. 2.1) can be obtained in the simpler cases (10,14,15); for more complex systems numerical solution methods have been used (16,17).

There are other interactions between the grain boundary and defect species aside from the electrostatic attraction/repulsion. Defect associates which have an electric dipole moment experience an attractive potential due to the steep gradient in electric field in the space charge. Also, solutes often have multiple driving forces, such as strain energy in addition to being charged. These additional factors have been included in the model of Yan et al. (17). Yan et al. (17) have also considered the case where two

aliovalent solutes of the same charge are present, but one has significant strain energy whereas the other does not. Their calculations show that the solute with greater total driving force will segregate preferentially, as it can both satisfy the space charge potential distribution and relieve its strain energy, even if it is present in the lattice in much lower concentrations than the solute with charge only. Under certain conditions, even repulsion of the major solute can occur. This is illustrated in Fig. 2.2, from Yan et al. (17).

2.1.2 Limitations of the Continuum Models

2.1.2.1 High concentrations

For a Boltzmann concentration distribution to be valid, the potential must be sufficiently low that concentrations are dilute everywhere ($n_i << N$). In this case the defects can be assumed to behave as point charges, and the width of the space charge is much greater than the ion size. This is true for electronic charge, and calculations indicate it is applicable for alkali halide systems of high purity at reasonably high temperatures (15,17). However, for oxides such as MgO, that have a higher electrostatic potential than the alkali halides and generally greater impurity levels including defects of greater effective charge, treating the defects as point charges results in calculated near-boundary

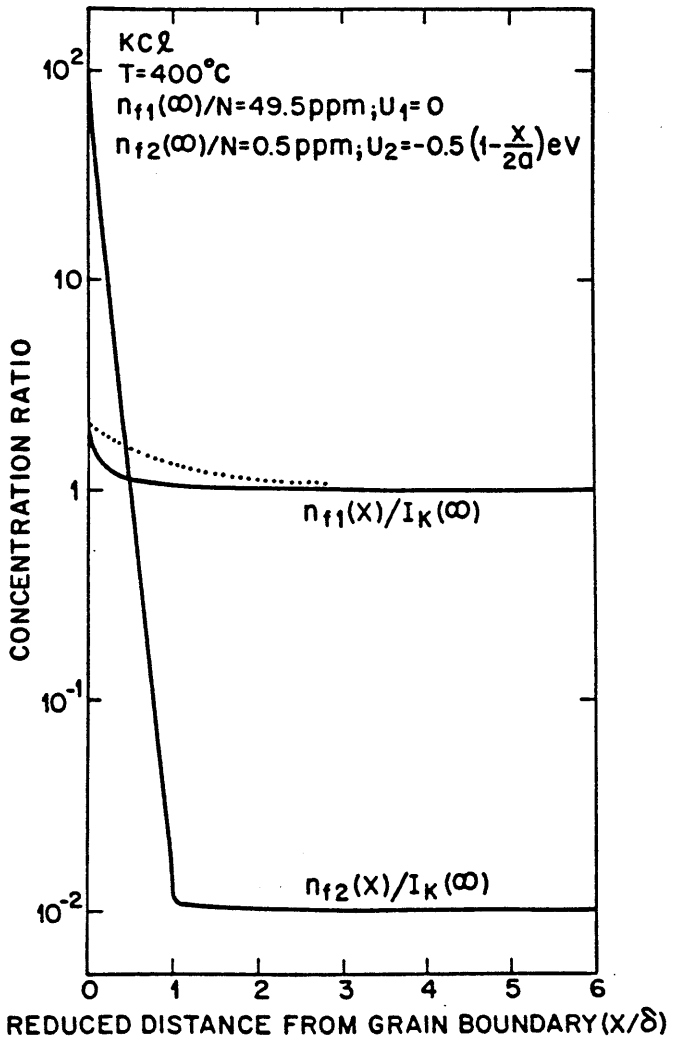

Figure 2.2 Calculated segregation for major and minor aliovalent impurities of the same charge, but where the minor impurity also has significant strain energy and segregates preferentially. From Yan, Cannon and Bowen (ref. 17).

concentrations far greater than the available number of lattice sites and space-charge widths of subatomic dimensions. As an example, the experimentally measured distribution of Sc^{3+} in MgO (18) shows a far broader distribution and lower concentrations than predicted by the continuum models.

One improvement in the model results if we do not assume $n_i << N$ and instead obtain the concentrations as Fermi-Dirac distribution functions:

$$n_i(x)/(N_i-n_i(x)) = [n_{i,\infty}/(N_i-n_{i,\infty})] \exp[z_i e(\underline{\varphi}(x)-\underline{\varphi}(\infty))/kT] \qquad (2.12)$$

in which N_i is the saturation concentration. This is essentially the same as McLean's equation (19) for segregation in partial monolayers at the grain boundary core, and has also been used by Blakely and Danyluk (16) in their work on the somewhat different problem of surface site saturation. With this distribution the concentration of defects does not exceed the available sites, but may rise rapidly to this saturation value as one approaches the boundary. Still the model is unsatisfactory in many cases, for the finite size of charged ions is not accounted for; although concentrations are bounded the calculated depth of the space charge remains far less and the charge density far greater than is physically possible.

Ion size effects have been recognized in colloid science

for some time. Stern (20) suggested that in situations where the potential is too high for a dilute solution model, one could assume an adsorbed monolayer or partial monolayer of ions at the charged particle surface, across which the potential drops linearly to a value small enough to apply the continuum model (known as the Gouy-Chapman model in colloid chemistry). While this approach is adequate for some electrolyte systems, in MgO it has been found that the model fails since experimentally it is found that the first partial monolayer contains insufficient charge to reduce the potential to a manageable level (18). A multiple layer adsorption model analogous to multiple layer gas adsorption seems to describe the data best (18); however, a theory which can predict the solute distribution widths and concentrations from first principles is lacking.

2.1.2.2 Saturation of Grain Boundary Sites

The assumption that the grain boundary is a perfect source and sink for defects, i.e. that there are sufficient grain boundary sites to accomodate the grain boundary charge at thermal equilibrium, is not likely to be valid at high electrostatic potentials and correspondingly high grain boundary charge concentrations. Eshelby (11) pointed out that the individual defect formation energies and thus the magnitude of the space charge potential difference are not independent of the characteristics of the source. Poeppel

and Blakely (21) and Blakely and Danyluk (16) have modeled the case where there is a fixed density of surface sites with a specific binding energy for ions, in analogy with surface electronic states in an intrinsic semiconductor. The potential difference between surface and bulk is determined by the occupation statistics of these surface states, and it is found that saturation of the surface sites causes the magnitude (whether positive or negative) of the space charge potential to decrease, eventually decaying to zero in the limit.

Experimentally, there has been to date no set of data complete enough to indicate saturation of grain boundary segregation in an ionic solid, although at grain boundary charge densities approaching a monolayer (as observed in MgO, 18) it seems likely to occur. There is also insufficient information to indicate what the capacity for charged defects of specific grain boundaries is. It is reasonable to expect special orientation boundaries with a high density of coincidence sites or low angle tilt boundaries that can be modeled as well separated dislocation arrays to have lower capacity for charge than more disordered boundaries.

Recent calculations by Duffy and Tasker (22) for impurity segregation at [110] tilt boundaries in NiO indicate that there are sites at grain boundaries at which the Madelung potential favors segregation of aliovalent solutes; this type of segregation is distinct from both strain energy

and space charge arguments, and introduces another potential source of grain boundary charge.

2.2 Solute Drag

When there is an interaction between solutes and the grain boundary leading to segregation or depletion of solute, the tendency of the solute distribution to migrate along with the boundary leads to a solute drag force. At low velocities the solute cloud is able to remain attached and the mobility is limited by diffusion of solute; at some higher velocity the grain boundary is able to break away from the solute cloud and migrate at an intrinsic velocity. There have been numerous theories proposed to explain the solute drag effect (2,3,23-28), but the simultaneously developed and very similar models of Cahn (2) and Luecke and Stuewe (3) have been found most consistent with experimental results. Cahn's model is more quantitative and concise, and will be reviewed here.

The force a solute atom exerts on the grain boundary is taken to be the gradient of the interaction energy, $-(dU/dx)$. The total solute drag force is

$$P_i = -N \int_{-\infty}^{+\infty} (C-C_o)(dU/dx)dx \qquad (2.13)$$

where N is the number of atoms per unit volume, C the solute concentration near the boundary, and C_o the bulk solute

concentration.

Solutions for C(x) as a function of the steady state velocity have been obtained by Cahn (2) and Luecke and Stuewe (3) for a general triangular potential well U(x), and by Yan (29) for the space charge potential in ionic solids. It is found that with increasing velocity the solute cloud concentration decreases and the asymmetry of the distribution increases; there is more solute trailing the boundary than leading (for attractive solute-boundary potentials) and therefore the force on the boundary opposes its forward motion.

Cahn (2) showed that at low velocities the drag force is given approximately as

$$P_i = 4NC_oVkT \int_{-\infty}^{+\infty} [\sinh^2(U(x)/2kT)/D(x)]\, dx \qquad (2.14)$$

in which D(x) is the spatially varying solute diffusivity. The integrand shows that in this velocity regime slowly diffusing solutes exert greater drag force than faster diffusing ones. Also, the drag force is independent of the sign of U(x), such that solutes depleted from the boundary cause just as much drag per unit concentration as those that segregated.

At higher velocities an approximate expression is

$$P_i = C_o N/kTV \int_{-\infty}^{+\infty} (dU/dx)^2 D(x)\, dx. \qquad (2.15)$$

Note that here the faster diffusing solute exerts more drag; this was an important result of the theory for it gave a plausible explanation for observations in metals systems (30,31) where faster diffusing solutes were found to retard migration more. This result is physically explained by considering that at high velocities the grain boundary is sweeping through a nearly uniform solute concentration field, and any perturbations in the concentration will result in drag. A faster diffusing solute is more able to develop a perturbation about the boundary, and thus causes more drag. The drag force is inversely proportional to velocity in Eq. 2.15; with increasing velocity the drag force decreases instead of increasing as in the low velocity regime (Eq. 2.14), and eventually the intrinsic boundary drag dominates.

Equations 2.14 and 2.15 have been combined into an expression which fits the high and low velocity extremes:

$$P_i = \alpha C_o V/(1+\beta^2 V^2) \qquad (2.16)$$

where

$$\alpha = 4NkT \int_{-\infty}^{+\infty} \{\sinh^2[U(x)/2kT] \,/\, D(x)\}\, dx \qquad (2.17)$$

$$\alpha/\beta^2 = N/kT \int_{-\infty}^{+\infty} (dU/dx)^2 \, D(x) \, dx \qquad (2.18)$$

The parameter α represents the impurity drag per unit dopant concentration per unit velocity, and β^{-1} represents the drift velocity of solute across the grain boundary region (32). The low and high velocity regimes are delineated by $V < \beta^{-1}$ and $V >> \beta^{-1}$ respectively.

At a steady state boundary velocity, the driving force for boundary migration is balanced by the total drag force

$$F = P_o + P_i = V/M_o + \alpha C_o V/(1+\beta^2 V^2) \qquad (2.19)$$

where P_o is the intrinsic grain boundary drag and M_o the intrinsic mobility, given by a simplified form of Turnbull's expression (33):

$$M_o \approx D_b \Omega/wkT \qquad (2.20)$$

where D_b is the rate controlling boundary diffusivity, w the boundary width, and Ω the ionic volume.

Equation 2.19 gives rise to the velocity-driving force relation shown in Fig. 2.3, where the limiting slopes at low and high velocities are respectively the reciprocal solute drag mobility, M_b^{-1}, and the reciprocal intrinsic mobility, M_o^{-1}. In the transition region (dotted line) two stable velocities are possible, the solute drag limited and the intrinsic, and Cahn (2) identified these intermediate

driving forces and velocities as a region where jerky and irregular boundary motion might occur as transitions from one stable velocity to another takes place. When multiple solutes are present, transitions between different solute drag controlled regimes are also possible. In recent work by Glaeser (5), jerky and irregular boundary motion in LiF was attributed to transition behavior. However, in the present work the experimentally interesting regime is the low velocity leg, where the solute drag mobility is

$$M_b = [M_o^{-1} + \alpha C_o]^{-1} \approx [\alpha C_o]^{-1}. \qquad (2.21)$$

2.3 Grain Growth Kinetics

Let us assume a single-phase, fully dense polycrystalline material of narrow grain size distribution in which the grain boundary mobility, M_b, and boundary energy, γ, are the same for all boundaries. The average grain boundary velocity is:

$$V = 1/2(dG/dt) = M_b F \qquad (2.22)$$

where G is the average grain size and F is the driving force for grain growth. The grain boundary energy density is (34):

$$\gamma S_V = 2\gamma/L \approx 3\gamma/G \qquad (2.23)$$

where S_V is the boundary area per unit volume and L the mean linear grain intercept (as measured from a two-dimensional section). The actual driving force is less than the boundary

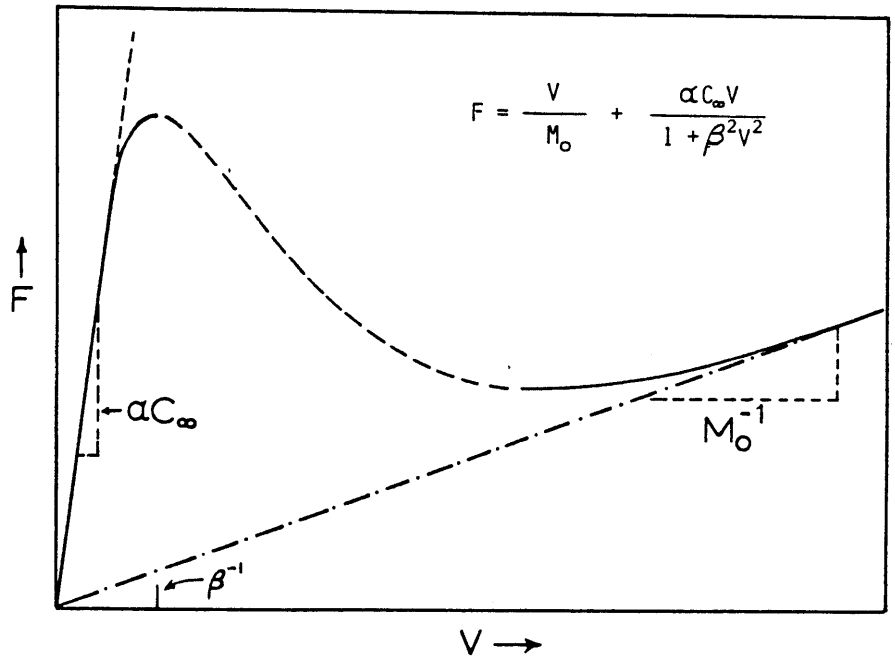

Figure 2.3 Schematic driving force-velocity relation after Cahn (ref. 2).

energy density, however, because the grains are not spherical and the mean boundary curvature is less than 1/G. Hillert (35) has shown that a reasonable approximation for the actual driving force is about one-sixth of that in Eq. 2.23, so that one has:

$$dG/dt = 2M_bF = M_b\gamma/G \qquad (2.24)$$

Integration yields the usual parabolic grain growth equation:

$$G^2-G_o^2 = 2M_b\gamma t. \qquad (2.25)$$

where G_o is the average initial grain size.

For the case of a large grain growing into a fine grained polycrystalline matrix (secondary recrystallization), the driving force is the grain boundary density (Eq. 2.23) so that the velocity of the recrystallization front is:

$$V' = 6M_b\gamma/G_m \qquad (2.26)$$

where G_m is the average matrix grain size.

It is sometimes found that despite uniform or "normal" grain growth the time dependence is not parabolic; instead the average grain size increases according to a relation of the form:

$$G^n-G_o^n = K(T)t \qquad (2.27)$$

where n=3 or 4 and K is a temperature-dependent constant. The derivative of Eq. 2.27 yields:

$$V = 1/2\ dG/dt = K/(2nG^{n-1}) \qquad (2.28)$$

which implies that the mobility is a function of grain size:

$$M_b = V/F = K/(n\gamma G^{n-2}). \qquad (2.29)$$

Brook (36) has shown that for solute drag controlled boundary mobility, if nearly all of the solute is segregated at boundaries rather than dissolved in the grains, a cubic law (n=3) can result as the amount of solute per unit grain boundary area decreases with increasing grain size. To our knowledge this phenomenon has not been unambiguously documented by parallel measurements of grain boundary segregation and grain growth kinetics, although sometimes cubic kinetics are attributed to this effect. Cubic growth can also result when pore drag is the controlling mechanism (37), when coalescence of second phase particles occurs (35), or when grain growth occurs by solution-precipitation in the presence of a liquid phase (38).

Driving force dependent transitions between solute drag controlled and intrinsic boundary mobilities, or between different solute controlled regimes (e.g. in the presence of multiple solutes), are another source of grain size dependent boundary mobilities. In principle, if the mobility is solute-drag controlled the assumption that the mobility is single valued cannot be valid, since shrinking grains must eventually achieve a high enough boundary curvature for solute break-away. If, however, break-away occurs at very small grain sizes compared to the average, its influence on the time-averaged mobility is negligible.

Measurements by Glaeser (5) of the mobilities of individual grain boundaries upon recrystallization of

deformed LiF showed extremely erratic boundary motion whereby a boundary would often remain pinned and immobile for long periods of time, then migrate rapidly and suddenly, and then perhaps stop again. Different segments of the same grain boundary often behaved unpredictably. For grain boundary migration of this character, a macroscopic time averaged mobility is clearly meaningless. The pinning and unpinning events in Glaeser's work (5) were attributed primarily to transitions between intrinsic and solute-drag mobilities, although in other instances the variation in boundary misorientation along a curved boundary or between different boundaries in a polycrystalline structure can lead to mobility variations. Inhomogenous solute distributions can cause similar effects.

Thus, extreme caution is required in interpreting grain boundary mobilities mechanistically. In polycrystals, the uniformity of grain growth (narrowness of the grain size distribution) is one indication of how wide a range of mobilities exist, and it is expected that high purity materials are more susceptible to transition behavior and boundary structural effects than heavily doped (but single phase) materials.

III. LITERATURE REVIEW, Part 2:

Properties of Magnesium Aluminate Spinel

3.1 Crystal Structure

Magnesium aluminate, the mineral spinel for which materials of the spinel structure is named, has a structure based on cubic close-packed oxygen ions in which one-half of the octahedral interstices (B sites) and one-eighth of the tetrahedral interstices (A sites) are occupied by cations. The unit cell contains 32 oxygen ions, i.e. 8 FCC oxygen units. In a "normal" 2-3 spinel, the trivalent and divalent ions occupy B and A sites respectively and it is usually written $A(B_2)O_4$. This structure is shown in Figure 3.1. In an "inverse" spinel, the trivalent cations are equally divided between octahedral and tetrahedral sites, $B(AB)O_4$. These two distributions represent extremes in a continuum of distributions, although most spinel compounds tend more towards one or the other and are defined as "normal" or "inverse" on the basis of their preference as $T \longrightarrow 0K$. Magnesium aluminate is thus considered a normal spinel, although significant disorder occurs upon heating.

The oxygen close-packing in spinels is not quite perfect, and an additional parameter u, known as the oxygen parameter, is used to describe the deviation from perfect packing. For most spinels u is slightly larger than the perfect-packing value of 0.375, which corresponds to enlargement of the tetrahedral interstices by oxygen ion

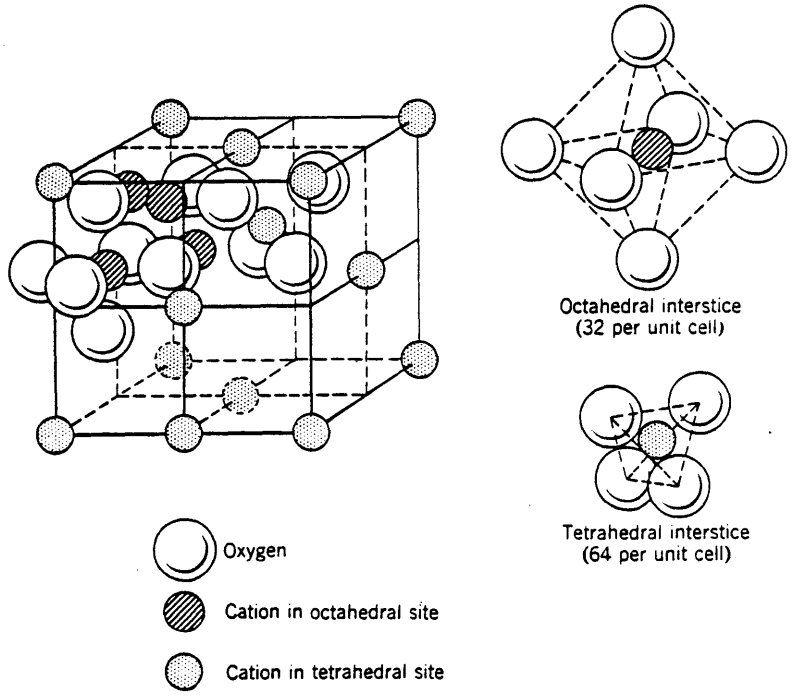

Figure 3.1 Crystal structure of normal spinel.

displacements along [111] directions (39).

The space-group of spinel is usually given as Fd3m, but in recent years there has been some controversy over whether or not it is instead of the lower symmetry $F\bar{4}3m$. This was first suggested by Jagodzinski and Saalfeld (40) and more recently the argument has been revived by work of Grimes (41, 42). Electron diffraction results by Hwang, Heuer and Mitchell (43) and Heuer and Mitchell (44) supported the lower symmetry space group in $MgAl_2O_4$, but neutron diffraction results on Fe_3O_4 (45), $MgCr_2O_4$ (46), and $MgAl_2O_4$ (47) did not. Recent convergent beam diffraction results by Steeds and Evans (48) also show most unequivocally a Fd3m space group for magnesium aluminate. However, it may be that all of these authors are partly right, as Mishra and Thomas (49) claim to have observed a second-order phase transformation from space group $F\bar{4}3m$ to Fd3m upon heating $MgAl_2O_4$ above 450°C. Suzuki and Kumazawa (50) have observed anomalous thermal expansion in $MgAl_2O_4$ at about 660°C in which the linear expansion coefficient follows a second order "lambda" transition, which they suggest is the same transition as observed by Mishra and Thomas (49). This second-order tranformation, if it truly exists, may well be sensitive to impurities and nonstoichiometry in the samples as well as temperature, such that there is sample to sample variability.

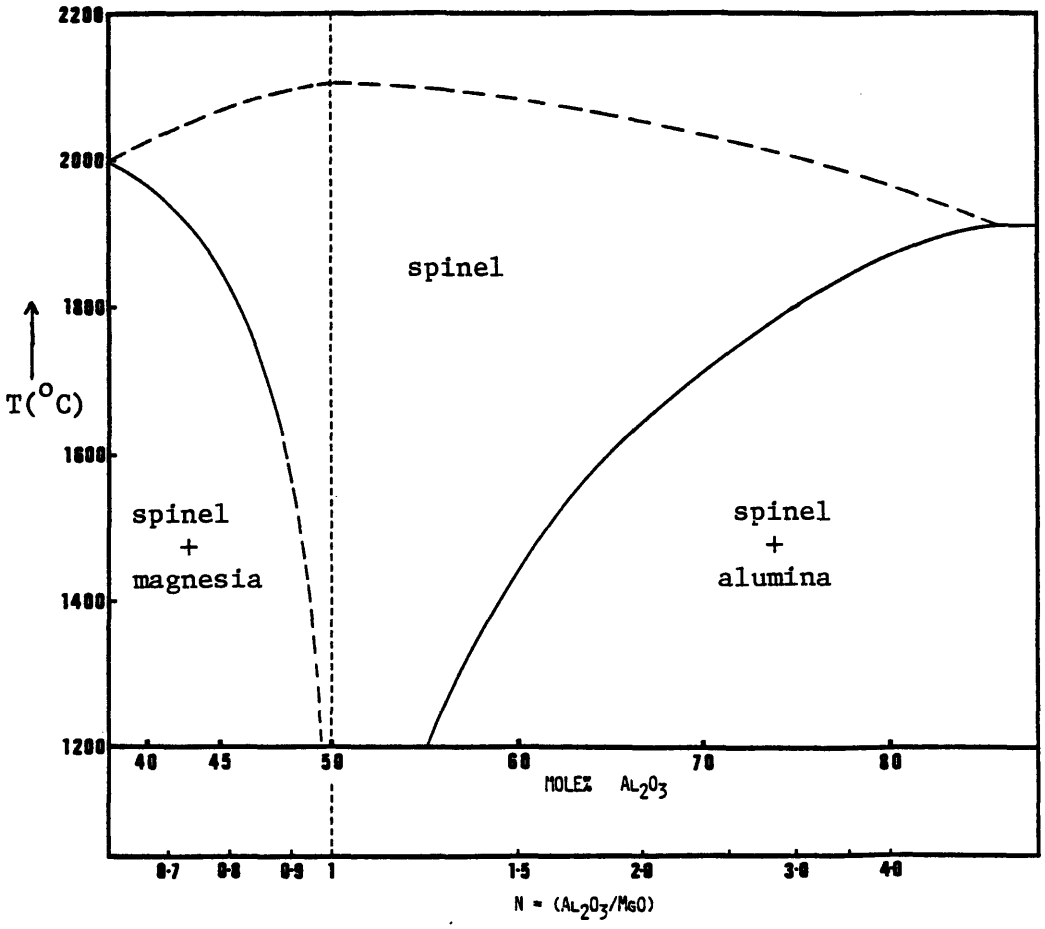

Figure 3.2 Phase diagram for magnesium aluminate spinel. (from ref. 51 and 52).

3.2 Phase Equilibria

The limits of solid solution in alumina rich compositions have been established by Roy et al. (51) and in magnesia rich compositions by Alper et al. (52). These results are compiled and illustrated in Figure 3.2. The solid solubility is extensive in alumina-rich compositions (up to $Al_2O_3/MgO \approx 6$) but very limited on the magnesia-rich side; because of the very few data points in the work by Alper et al. (52), the MgO-$MgAl_2O_4$ phase boundary must be regarded as somewhat schematic as drawn. Unpublished work by R.D. Bagley (Corning Glass Works, Corning, New York) indicates the magnesia solubility at high temperatures (1700-1900°C) may be quite a bit less than illustrated.

Because magnesium evaporates readily from spinel at high temperatures, it is difficult to prepare either single or polycrystals that are exactly stoichiometric. In much of the literature, what is reported as stoichiometric spinel is actually slightly alumina rich.

There have been a number of conventions used in the literature to denote spinel compositions, including the weight percent alumina, mole percent alumina, weight percent excess magnesia or alumina, and alumina-magnesia molar ratio. Throughout this work we will whenever possible refer to the composition in terms of the molar ratio, n, as in $MgO{:}nAl_2O_3$.

3.3 Electrical Conductivity

Sonder (53) determined that the ionic transference number in nearly-stoichiometric spinel is approximately unity over the temperature range 627°-1427°C and oxygen pressure range 1 to 10^{-16} atm. Iron impurity up to 0.1% had negligible influence on the results. Since the electronic mobility is orders of magnitude greater than the ionic mobility ($\approx 10^{8}$ greater in MgO, 54), for the ionic conductivity to dominate indicates that the electronic defect concentration is negligible.

Bates and Garnier (55) and Weeks and Sonder (56a) have measured the electrical conductivity of stoichiometric spinel; Sonder and Darken (56b) examined alumina-rich as well as stoichiometric spinel, and their results in Fig. 3.3 illustrate the main features of interest.

The alumina excess spinel conductivity is more easily interpreted; for compositions of n=1.9 and 2.0 a single activation energy of 2.5-2.7 eV was observed. Sonder and Darken (56b) interpreted this as a cation vacancy conduction mechanism, which is reasonable since alumina excess is accomodated by cation vacancies (40). However, the vacancy concentrations in n=2 spinel are very high (4.76% of the normally occupied lattice sites) and although there is little evidence for defect association or clustering effects (non-ideality seems unimportant even at such concentrations; see Section 4.5), the correlation factor may be strongly

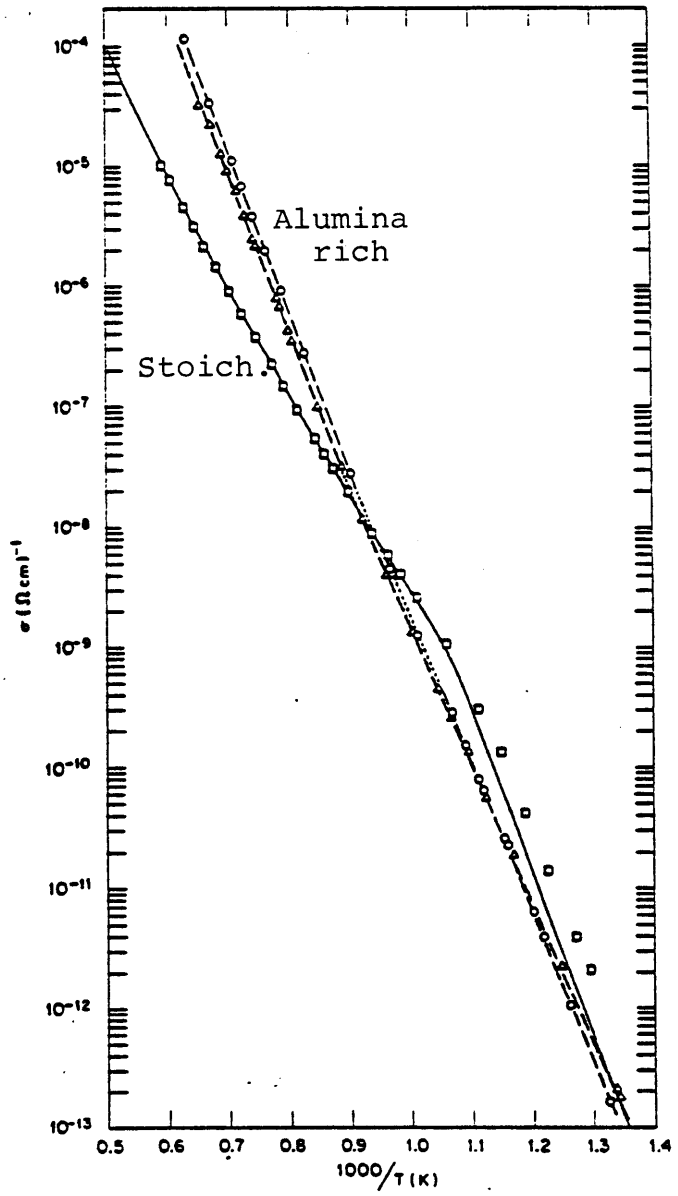

Figure 3.3 Electrical conductivity in stoichiometric and alumina rich spinel, from Sonder and Darken (ref. 57).

influenced. Nonetheless, it appears that a single conduction mechanism is dominant in spinel of this composition at these temperatures.

In stoichiometric spinel, all three authors observed a decrease in activation energy in stoichiometric spinel upon heating through ≈650°C, which may be related to the second order phase transformation that has been reported (49,50). Bates and Garnier (55) did not obtain data above 830°C, but from 650° to 850°C their activation energy (1.65 eV) agrees well with that measured by the others (1.5-1.6 eV, 56a,b). At higher temperatures (≈1050°C) a gradual upturn in slope to an activation energy of ≈2.2 eV is found. There is no discontinuous change in slope here, and there are several possible explanations for the behavior. There may be a dependence on cation inversion, which changes gradually in this temperature range, or two competing conduction mechanisms that are not very different in energy. It is not clear if cation diffusion in spinels proceeds by motion from lattice site to lattice site or if intermediate steps to interstitial sites are involved; the preferred path may depend on defect concentrations. The fact that the high temperature activation energy is less in stoichiometric spinel suggests that at low vacancy concentrations, a lower energy path involving interstitial motion may be preferred, while in the highly alumina-rich spinel, vacancy motion is dominant.

At low temperatures (<850°C) the conductivity of alumina rich spinel is lower despite its large defect concentrations. It has also been observed in other highly defective ionic systems, e.g. doped ZrO_2, that sometimes diffusion and conduction decrease with increasing defect concentrations (57). Although the details are not well understood, both defect association and correlated defect and ion motion are believed to be related to this effect.

It seems from these data that alternate conduction mechanisms may operate in stoichiometric spinel which are not present in alumina rich spinel where there are a high concentration of cation vacancies. A complete interpretation, which is beyond the scope of this work, must consider not only the multiple defect migration paths that are available, but also defect association behavior at low temperatures, and correlation factor effects.

3.4 Diffusion

3.4.1 Cation Diffusion

The magnesium tracer diffusivity in what was presumably nearly stoichiometric spinel was reported by Lindner and Akerstroem (58) as:

$$D_{Mg} = 200 \exp[-3.73 \text{ eV}/kT] \quad (\text{cm}^2/\text{sec}) \qquad (3.1)$$

There is some question about the reliability of this data as the samples used were porous and polycrystalline. Halbwachs et al. (59) have measured a similar 3.86 eV energy from

internal friction in highly alumina-rich spinel which they attribute to the magnesium-octahedral vacancy exchange. If this is true, the samples Lindner and Akerstroem (58) used must have been sufficiently alumina rich for the cation vacancy concentration to be pinned by nonstoichiometry as are Halbwachs et al.'s (59) samples, since for a truly stoichiometric sample the activation energy must include a vacancy formation energy term also, and therefore should be higher than the activation energy in nonstoichiometric spinel. This is possible if either the starting compositions were alumina rich or if magnesia loss from their samples occurred at high temperatures. Accepting the 3.73-3.86 eV energy to be that for magnesium-vacancy exchange, the 2.5-2.7 eV energy observed by Sonder and Darken (57) for ionic conduction in alumina-rich spinel is likely to be for the aluminum-octahedral vacancy exchange. We presume the vacancies are octahedral at the moderate temperatures of Sonder and Darken's measurements (750°-1450°C) as a result of Jagodzinski and Saalfeld's work (40) which showed that the cation vacancies in alumina rich spinel are located on octahedral sites.

There has been no measurement of the aluminum diffusivity in magnesium aluminate, but on the basis of a 2.5-2.7 eV energy for migration one can estimate the self-diffusion coefficient of aluminum vacancies at fixed dilute concentrations in alumina rich spinel:

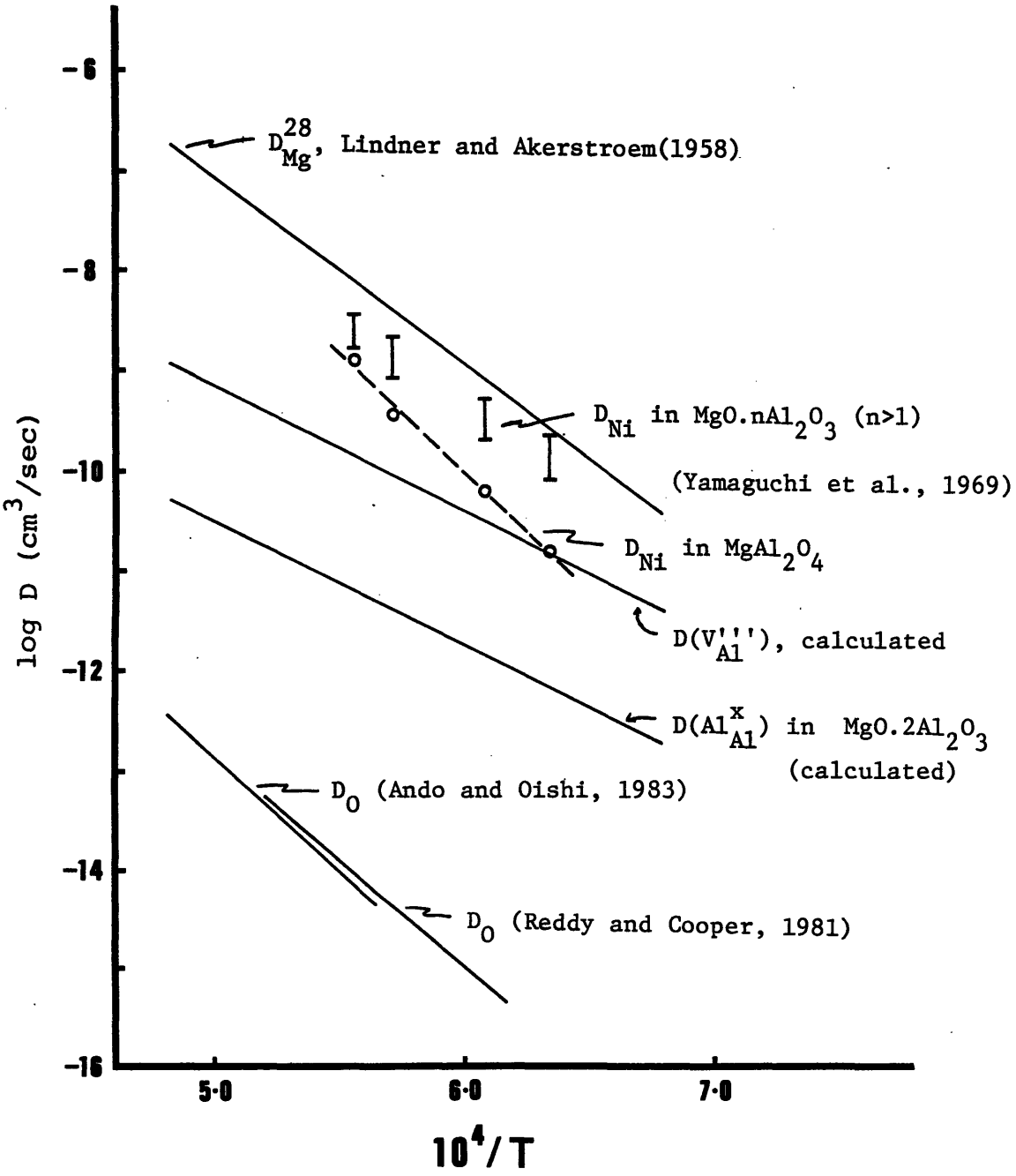

Figure 3.4 Diffusion coefficients in magnesium aluminate.

$$D(V_{Al}) \approx 1/6\ a^2\ \Gamma\ f\ \exp[-H_m/kT]$$

where a is the octahedral site jump distance, Γ the jump frequency ($\approx 10^{13}$ sec^{-1}) and f the correlation factor (≈ 1). The result is shown in Fig. 3.4. If we neglect association and correlation coefficient effects (thereby obtaining an upper limit to the diffusivity), the aluminum diffusivity is:

$$D(Al) = D(V_{Al})[V_{Al}]$$

and is shown in Fig. 3.4 for spinel of n=2 composition in which the vacancies are assumed to be on octahedral sites only. Both the calculated vacancy and aluminum diffusivities lie below the the magnesium diffusivity measured by Lindner and Akerstroem (58), but lack of confidence in their result makes any comparison difficult.

Yamaguchi et al. (60) have made measurements of Ni^{2+} diffusion in magnesium aluminate as a function of stoichiometry from stoichiometry to n=1.5. Interdiffusion couples were prepared in which both sides of the couple were of the same stoichiometry but one had one-tenth of its Mg^{2+} content replaced by Ni^{2+}. In the temperature range 1305°-1527°C, they found the nickel diffusivity to increase linearly with the cation vacancy concentration calculated from the amount of alumina excess, which supports a vacancy diffusion mechanism.

Yamaguchi et al. (60) further observed that the diffusion activation energy decreases from 4.6 eV for stoichiometric samples to a constant 3.0 eV for samples of

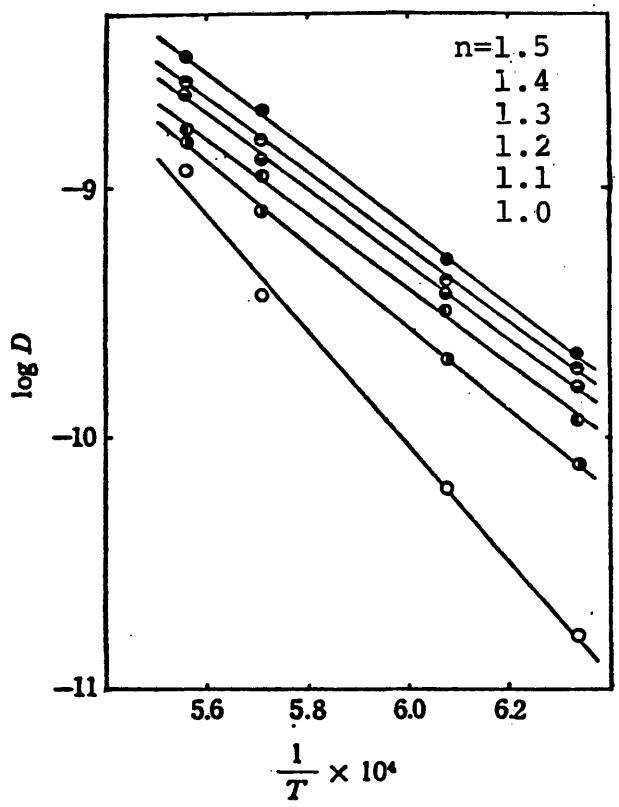

n	activation energy
1.0	4.6 eV
1.1	3.26
1.2	2.99
1.3	2.95
1.4	2.91
1.5	2.99

Figure 3.5 Nickel diffusion in stoichiometric and alumina rich magnesium aluminate spinel (from ref. 60).

composition n>=1.2, as shown in Fig. 3.5, suggesting a transition from intrinsic defects to extrinsic (stoichiometry-determined) vacancies. The intrinsic defect formation energy would then be 3.2 eV for a cation Frenkel or Schottky pair (the 1.6 eV difference represents one-half the pair formation energy).

In magnesium excess spinel there exists no experimental data, but in analogy with cation diffusion in magnetite (61) interstitials may become important, and they are likely to have a higher mobility than the lattice cations.

3.4.2 Oxygen Self-Diffusion

Oxygen self-diffusion in single crystals has been measured by Oishi and Ando (62) and Ando and Oishi (63) using ^{18}O gas exchange, and by Reddy and Cooper (64) using proton activation analysis. After correction of the gas exchange results for the particle surface area (65), there is good agreement between the two methods for stoichiometric spinel, with the diffusion coefficient given as (65)

$$D_{oxy} = 4.1 \times 10^{-2} \exp[-4.56 \text{ eV}/kT]. \qquad (3.2)$$

For alumina-rich spinel, while Ando and Oishi (63) find little difference in either the activation energy or pre-exponential for diffusion, Reddy and Cooper (64) find a nearly 10^2 greater diffusivity in an n=3.5 spinel. However, Reddy and Cooper's results are complicated by the

precipitation of alumina in these samples during the diffusion anneal, which may add a chemical driving force for oxygen in-diffusion. Ando and Oishi (63), on the other hand, conducted all of their anneals at temperatures within the spinel single phase field.

No clear interpretation of the oxygen diffusion mechanism has been made, but both of the above results are contrary to a simple vacancy diffusion mechanism, since the introduction of cation vacancies with excess alumina should suppress oxygen vacancies. As in other close-packed oxides, the oxygen diffusivity is orders of magnitude below that for the cations (Fig. 3.4).

3.5 Grain Growth in Spinel

Grain growth in magnesium aluminate has been measured by Bratton (66) and Uematsu et al. (6). Bratton (66) measured the grain growth in high density surface regions of sintered stoichiometric spinel and observed parabolic growth. Although other portions of the samples were more porous, apparently the dense surface regions were free of pore drag. If we assume 1000 ergs/cm^2 for the boundary energy, the mobility Bratton obtained is:

$$M_b = 8.55 \times 10^{-2} \exp[-4.77 eV/kT] \quad (cm^4/erg.sec) \qquad (3.3)$$

Uematsu et al. (6) reported that the grain boundary mobility at 1800°C as a function of composition followed the schematic form shown in Fig. 3.6. The most striking feature

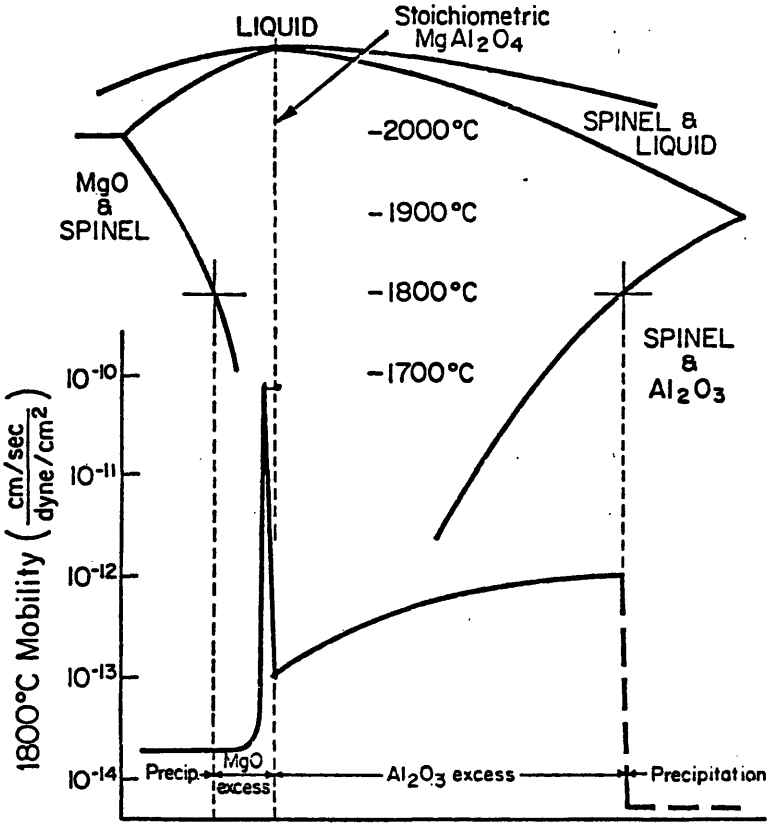

Figure 3.6 1800°C grain boundary mobility in magnesium aluminate as a function of composition, from Uematsu et al. (ref. 6).

is the 10^4 increase in mobility immediately to the magnesium excess side of stoichiometry. Because of the high vapor pressure of MgO above 1600°C, Uematsu et al. (6) suggested that the actual composition associated with the peak mobility may be stoichiometric rather than magnesia excess. With greater magnesia excess in solid solution, the mobility is shown as dropping below even that of the stoichiometric composition.

On the alumina excess side of stoichiometry, the mobility is shown increasing with alumina excess, and Uematsu et al. (6) suggested that this is due to kinetic factors. Once either boundary of the single phase field is surpassed, precipitates of MgO or Al_2O_3, depending on what is in excess, causes particle drag that further decreases the mobility.

In Figure 3.7 is shown the temperature dependence of grain boundary mobility in compositions Uematsu et al. (6) examined. The maximum mobility in Fig. 3.6 is plotted; this mobility was measured from a large, facetted, discontinuously growing grain (R.D. Bagley, private communication*). The mobilities of the alumina rich, stoichiometric and magnesia rich compositions are measured from uniform grain growth in polycrystalline samples. Although these samples are of

* The spinel mobility data in the reference by Uematsu et al. (6) were measured by R.D. Bagley (Corning Glass Works), who was kind enough to provide these experimental details.

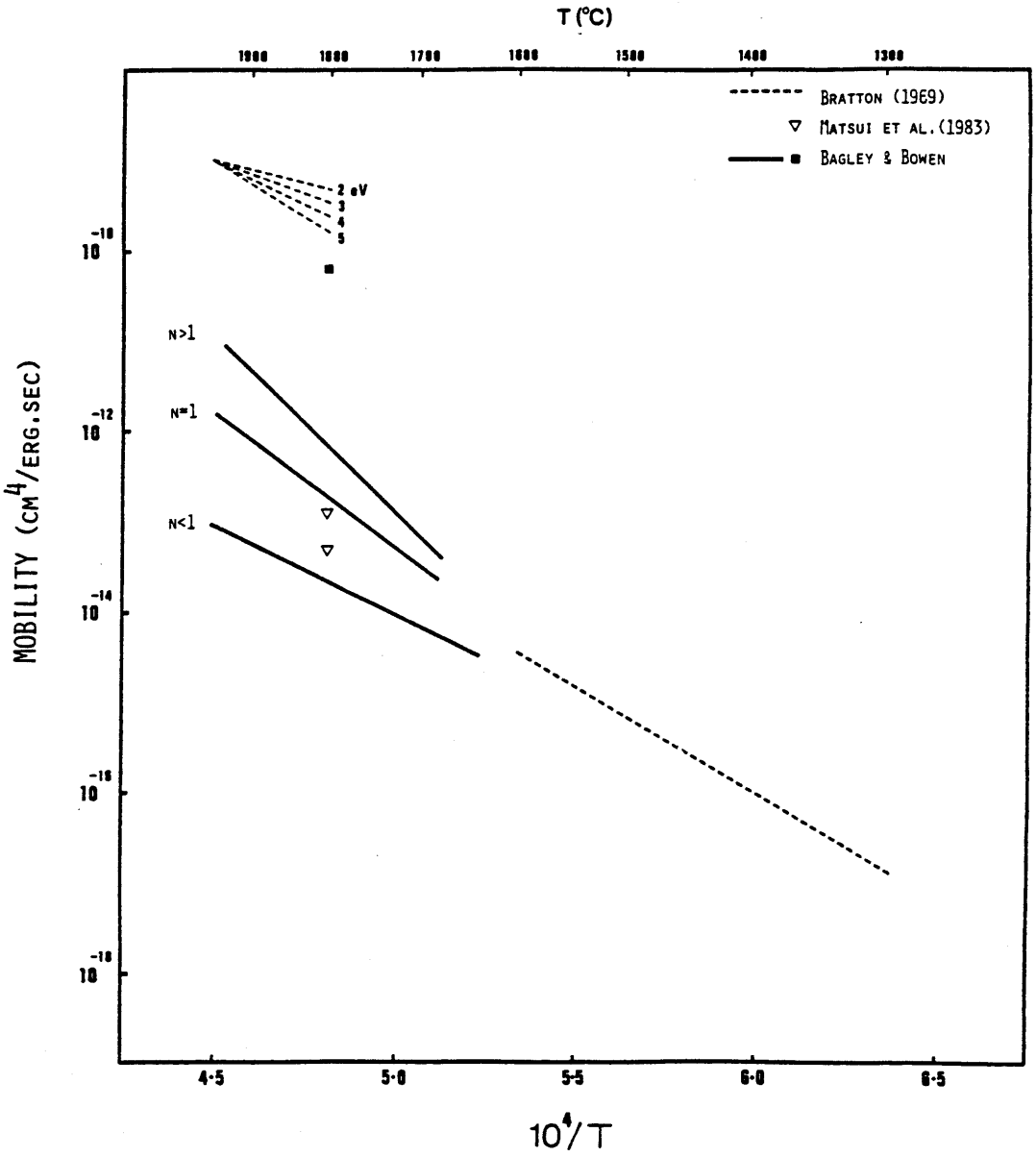

Figure 3.7 Boundary mobilities vs. temperature for spinel, from the literature.

compositions that should be single phase spinel at the temperatures in question it is not clear that these mobilities represent solid solution effects alone since the grain growth followed a 1/3 and sometimes 1/4 time dependence rather than the parabolic law associated with grain growth in the absence of interfering mechanisms. As discussed in section 2.3, time exponents of 1/n where n is not equal to 2 implies grain size dependent mobilities. A 1/3 dependence can result from strong impurity segregation (36), pore drag mechanisms, coalescence of a second phase, or grain growth in the presence of a liquid phase (37).

The apparent activation energies in the data of Uematsu et al. (6) for stoichiometric (6.08 eV) and alumina rich spinel (7.38 eV) also seem high. These are much higher than what Bratton (66) observed for stoichiometric spinel (4.77 eV), and are higher than any activation energies for diffusion in spinel. The magnesia rich samples show a 3.69 eV energy, which is close to the 3.73 eV found for Mg tracer diffusion (58), but the time exponent nonetheless makes a simple interpretation of the mechanism as Mg diffusion controlled tenuous.

Matsui et al. (67) have examined the effect of magnesia loss on pore removal rates in the final stage sintering of nearly stoichiometric spinel (n=1.07). Although it was not their purpose to measure grain growth, one can derive 1800°C mobilities from their published micrographs of the interiors

of as-sintered and annealed samples which did not experience magnesia loss. Data points derived assuming parabolic kinetics are included in Fig. 3.7; they are in good agreement with Uematsu et al.'s data for stoichiometric spinel at the same temperature, being slightly higher but within a factor of two.

IV. DEFECT STRUCTURE OF SPINEL

4.1 Introduction

A model for the defect structure of magnesium aluminate spinel can be developed from the literature in not only magnesium aluminate but also other spinels. The ferrite systems have been more thoroughly investigated since they are amenable to a wider variety of analytical techniques due to magnetic behavior and defect concentrations that vary widely with oxygen pressure. There has been more work on magnetite (Fe_3O_4) than any other system. One can generalize the results in many cases to include magnesium aluminate.

All findings to date indicate that ionic defects in spinels are restricted primarily to the cation sublattice. In this chapter we will first review the cation inversion phenomenon, followed by discussion of the native Frenkel defect mechanisms at stoichiometry and the solution mechanisms that accomodate nonstoichiometry. These results are then used to construct a Brouwer diagram which shows the principle defects and how their concentrations vary with alumina activity.

4.2 Cation Distributions in Spinel

Although natural magnesium aluminate cooled over geologic times is well ordered in the normal spinel distribution, upon heating to temperatures where atom

exchange is possible, some degree of randomization occurs. Direct evidence for this comes from infrared absorption experiments by Hafner and Laves (68), nuclear resonance by Brun and Hafner (69), a neutron diffraction study by Stoll et al. (70), and ESR measurements by Schmocker et al. (71) and Schmocker and Waldner (72) in which Cr^{3+} ions in solution, predominantly on octohedral sites, were used as a probe of the nearest neighbor cation environment.

While the existence of disorder can hardly be disputed, the actual amount of equilibrium disorder at any given temperature is unclear. The data of the Schmocker and Waldner (72) are plotted in Figure 4.1 as inversion parameter x, defined as the fraction of tetrahedral sites occupied by trivalent cations, against what the authors described as "peak temperature". The accuracy of the inversion parameter measured is given as +/-10%; however, the details of sample heating and cooling are not stated except to note that a few minutes at temperature is sufficient to cause disorder. Two natural spinels (of different impurity contents) were found to begin disordering at about 800-900°C.

It is found that when cooling at normal laboratory rates (i.e. without attention to rapid quenching) the thermal inversion in natural spinels does not completely reverse itself. This was observed by Schmocker et al. (71) and Schmocker and Waldner (72) in their ESR studies. Stoll et al. (70) earlier reported results in agreement with these,

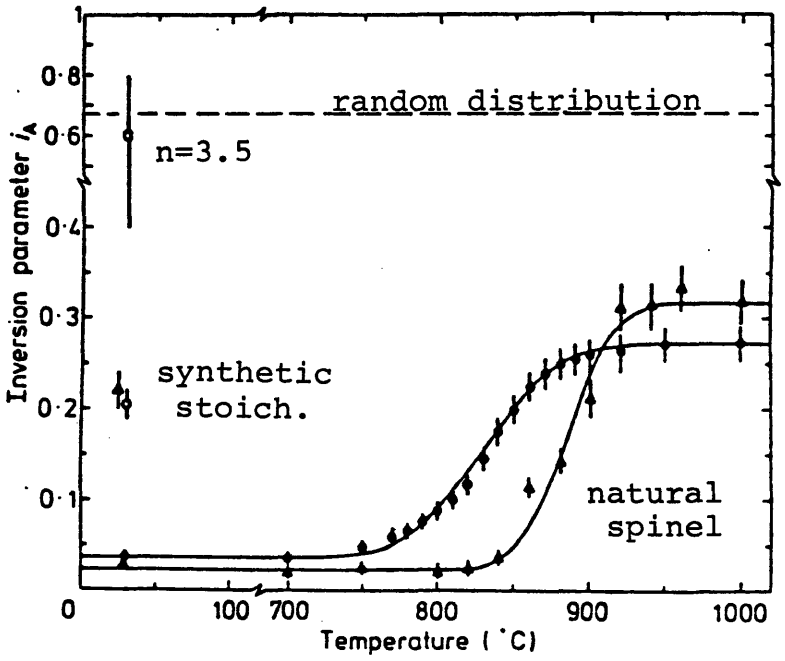

Figure 4.1 Cation inversion parameter, x, vs. temperature for magnesium aluminate (from ref. 72).

finding by neutron diffraction that x=0.10 to 0.15 in synthetic spinel, with the greater disorder found in more rapidly cooled samples. Schmocker and Waldner (72) show x≈0.2 for a synthetic sample in Fig. 4.1. (The high inversion parameter shown for an n=3.5 alumina rich synthetic spinel in Fig. 4.1 is misleading, however, as it indicates not so much inversion as the presence of excess aluminum ions in solution on magnesium sites.)

Therefore, all synthetic spinels, and also natural ones that have been heated above 800°-900°C, can be considered disordered. The approach to equilibrium disorder will be rapid at higher temperatures, but the ability to preserve it for observation upon cooling is in doubt. Figure 4.1 shows inversion reaching a plateau where x≈0.3 above 900°C, but given the unspecified heating and quenching procedures in the experiment one cannot take these curves to represent equilibrium conditions.

In order to address the issue of how much disorder is ultimately achieved, i.e. whether or not spinel reaches complete randomness (x=2/3) at higher temperatures, consider that cation inversion can be treated as a chemical equilibrium (73,74), which for $MgAl_2O_4$ is (in Kroeger-Vink notation):

$$Al_{Al}^{X} + Mg_{Mg}^{X} = Al_{Mg}^{\bullet} + Mg_{Al}'. \qquad (4.1)$$

Charge neutrality requires that

$$[Al_{Mg}^{\bullet}] = [Mg_{Al}'] \qquad (4.2)$$

if these are the predominant defects.

If concentrations of other defects such as vacancies and impurities on the two cation sublattices are small by comparison, one can write:

$$[Al_{Mg}^{\bullet}] + [Mg_{Mg}^{X}] = 1$$

$$[Mg_{Al}'] + [Al_{Al}^{X}] = 2. \qquad (4.3)$$

Assuming also that activities are equivalent to concentrations, the law of mass action gives the following equilibrium constant for inversion:

$$K_I = [Al_{Mg}^{\bullet}]^2/\{(1-[Al_{Mg}^{\bullet}])(2-[Al_{Mg}^{\bullet}])\}$$

$$= \exp[-G_o/RT] \qquad (4.4)$$

where G_o is the free energy change for inversion ($G_o=H_o-TS_o$). $[Al_{Mg}^{\bullet}]$ is just the degree of inversion, x. The non-configurational contribution to the entropy of inversion, S_o, is often assumed to be negligible since experimentally it is found that the defects behave as ideal solutions (75) so that we have:

$$\ln x^2/[(1-x)(2-x)] = -H_o/RT. \qquad (4.5)$$

For magnesium aluminate, Navrotsky and Kleppa (75) have measured the heat of solution of samples quenched from a range of temperatures using high temperature calorimetry, and derive a value for H_o of ≈10 kcal/mole. However, while the calorimetry is quite accurate, it is not clear that the high temperature distributions were quenched in, so this H_o value may be an overestimate. Another estimate is possible from the data of Schmocker and Waldner (72) in Fig. 4.1. If we

take the position of the knee in the curves of inversion vs. temperature as a point where atom motion is both fast enough to reach the equilibrium distribution in a reasonable laboratory time and slow enough that it can be quenched in, a value for H_o of ≈6.5 kcal/mole is derived.

These two values seem to be reasonable bounds on H_o compared to the disorder measured by X-ray diffraction in two other normal spinel aluminates, $CoAl_2O_4$ and $ZnAl_2O_4$. Schmalzreid (73) determined the inversion in water-quenched tablet samples of $CoAl_2O_4$ at 850° and 1400°C to be 0.055 and 0.15 respectively, yielding from Eq. 4.5 H_o=14+/_3 kcal/mole. In $ZnAl_2O_4$, Cooley and Reed (76) measured H_o values of 16 to 18 kcal/mole on powder samples withdrawn from the furnace at 905°-1200°C and quenched into water. The increase in H_o in the order of tetrahedral cations, Mg^{2+}, Co^{2+}, Zn^{2+}, is in agreement with the sequence of site preference energies determined from experimental data and from crystal field theoretical studies (75), in which Zn^{2+} is found to have a few kcal/mole more tetrahedral preference than Co^{2+}, which in turn is a few kcal/mole removed from Mg^{2+}.

More complex relations than Eq. 4.5 have been advanced to describe the disorder, including:

1) Taking H_o to vary linearly with the amount of disorder (77).
2) Taking H_o to vary quadratically with disorder (78).
3) Adding a non-configurational entropy term (S_o) (76,

79,80).

4) Considering non-ideal mixing on each sublattice (81).

In the literature, often the approach taken has applied to a specific system the particular workers were interested in, and no one improvement has been shown to apply generally, although O'Neill and Navrotsky (78) argue that a quadratic dependence of H_o on x is to be expected from theoretical considerations of the change in lattice energy upon disordering. There is in general an absence of data of sufficient accuracy to test the various models.

The most accurate data on cation distribution to date is probably that of Wu and Mason (80) on Fe_3O_4, in which thermopower measurements at temperature remove the uncertainty about redistibution on cooling that is always present in room temperature measurements on quenched samples. Mason and Bowen (82,83) had earlier determined that a nearly random iron distribution was reached at high temperatures. Wu and Mason (80) confirmed this in detail, finding that complete randomness is reached at ≈1450°C , and that a non-configurational entropy term is necessary to describe the data adequately.

However, magnetite may not be representative of other spinels since it is not clear to what degree Fe^{2+} and Fe^{3+} are distinguishable ions on the octahedral sublattice that show configurational entropy, as opposed to entropy associated with partially delocalized electrons (78).

Assuming the ions are distinguishable, the difference in site preference energies for Fe^{2+} and Fe^{3+} yields a smaller disorder enthalpy ($H_o \approx 4$ kcal/mole, 83) than the aluminates for which less disorder is reported. Without more accurate data over a greater temperature range, the use of more parameters than in Eq. 4.5 for the aluminates is unjustified, and for simplicity we will proceed accordingly.

The inversion parameter against temperature for magnesium aluminate calculated using Eq. 4.5 has been plotted in Fig. 4.2 using bounding H_o values of 6.5 and 10 kcal/mole. These curves illustrate that complete randomization is probably not reached below the melting point of magnesium aluminate (2105°C), and over the experimental temperature range relevant to this work (1200-1800°C) the inversion is in the range 0.2 to 0.4 depending on which estimate of the enthalpy is more accurate.

In order to maintain Kroeger-Vink notation for coherency with later considerations of space charge segregation in which it is necessary to define the relative charges of defects, one needs to choose a reference system.
From the above, in the temperature range of interest spinel is approximately one-half disordered, thus it would be appropriate to choose either the perfect, ordered spinel or the random spinel as the reference state. For a random cation distribution, an average charge for cation sites can be specified. However, it seems conceptually simpler to deal

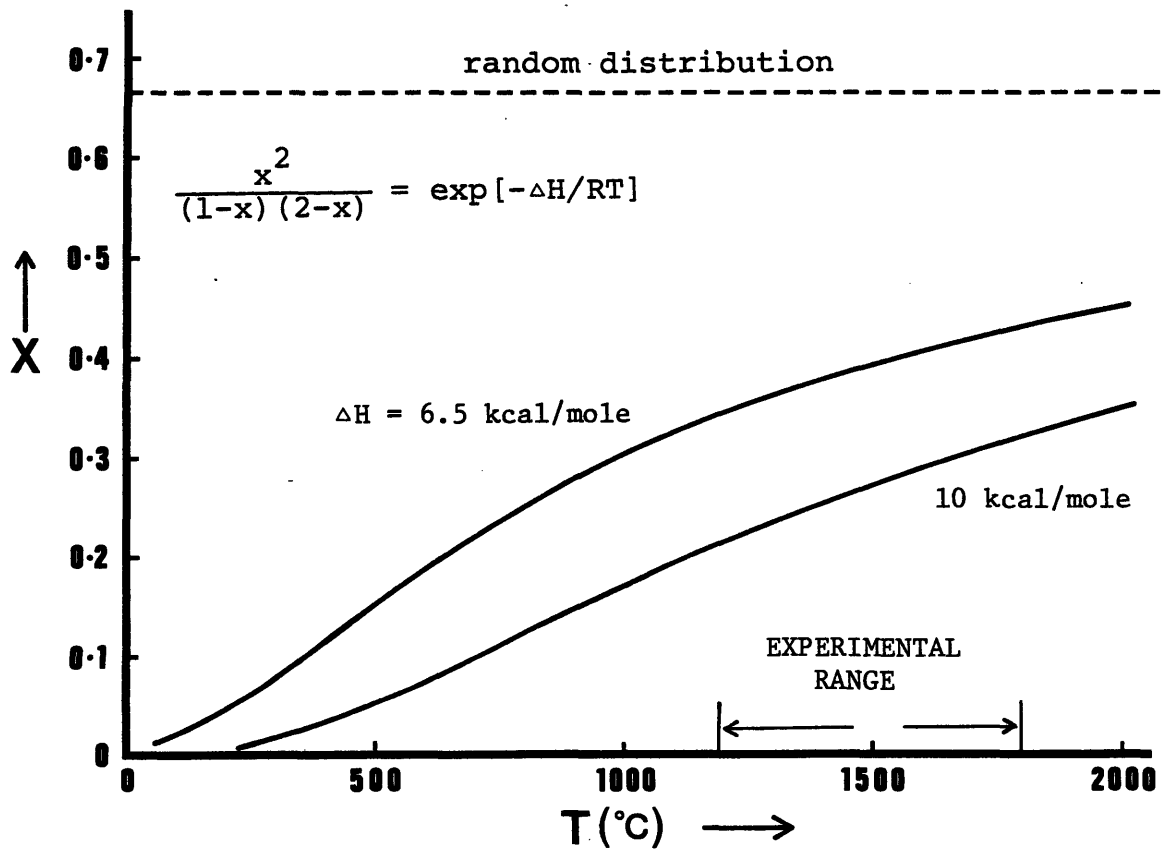

Figure 4.2 Calculated cation inversion in spinel.

with integral charges, so we will reference all defects to the perfect spinel.

4.3 Secondary Defects

4.3.1 Frenkel Pairs

Given the large numbers of vacant cation sites in spinels, it is often assumed that displacing a cation to one of those sites is not highly energetic and therefore cation Frenkel pairs will be easily formed. This has been shown to be true in Fe_3O_4 by Dieckmann and Schmalzreid (61,84) from the oxygen partial pressure dependence of iron tracer diffusivity. For an iron Frenkel defect mechanism, at high oxygen activity the iron vacancy concentration should be proportional to $p(O_2)^{2/3}$, whereas at low oxygen activity the interstitial concentration should be proportional to $p(O_2)^{-2/3}$. The iron tracer diffusivity follows exactly this form (61,84), with a minimum in diffusivity between the two regimes. Furthermore, Dieckmann et al. (85) have observed the same behavior for Co and Cr diffusing in Fe_3O_4, and Petuskey (86) finds the same is true for Al in Fe_3O_4 upon extrapolating interdiffusion coefficients in Fe_3O_4-$FeAl_2O_4$ to pure magnetite. Thus, both iron and these foreign cations form Frenkel pairs in stoichiometric magnetite, and migrate via cation vacancies at high oxygen pressure and interstitials (or possibly by an interstitialcy mechanism;

the experiments do not distinguish between the two) at low oxygen pressure. For iron, Dieckmann and Schmalzreid (88) have determined from the minimum in diffusivity relative to the minimum in defect concentrations that the iron interstitial is ≈15 times more mobile than the iron vacancy at 1200°C.

In magnetite the Frenkel reaction constant K_f has been estimated only for iron and only at 1200°C (to be $\approx 10^{-8}$, 87,88); therefore there is not a reliable value for the Frenkel formation energy. However, Dieckmann et al. (85) show that the temperature dependence of tracer diffusion at constant oxygen pressure in the interstitial(cy) regime includes the enthalpy for both motion and Frenkel defect formation, and this sum ($H_{m,i} + H_f$) increases for the cations examined from 3.43 to 5.14 eV in the order Fe, Co, Al and Cr. The enthalpy for diffusion of these same cations in the high oxygen pressure vacancy regime includes a motion and association term, and also increases, from 1.42 to 2.54 eV in the same order Fe, Co, Al, and Cr. If we take the interstitial and vacancy mechanism migration energies to be about the same, Frenkel formation energies in the range 2.0-2.7 eV are suggested by these data.

In magnesium aluminate, Yamaguchi et al. (60) have observed a 1.6 eV greater activation energy for Ni diffusion (by a vacancy mechanism) in stoichiometric ($n \approx 1$) versus alumina rich ($1.2 < n < 1.5$) samples (4.6 vs. 3.0 eV), which they

attribute to an intrinsic defect formation energy. For a Frenkel or Schottky defect pair this corresponds to a formation energy of 3.2 eV. While no theoretical estimates of the Frenkel or Schottky energy in spinel have been made, compared with calculated energies in other close-packed oxides of ≈7.5 eV for the Schottky pair in MgO (89), ≈5 eV for the Schottky triplet in TiO_2 (90), and ≈20 eV for the Schottky quintet in Al_2O_3 (90), this 3.2 eV energy seems unreasonably low for a Schottky energy and is more likely to be for a cation Frenkel reaction.

However, in detail there are a total of eight cation Frenkel reactions that one can write for a partially disordered spinel. Without specifying the interstitial site of interest, we have for magnesium aluminate spinel:

$$Al_{Al}^{x} \longrightarrow Al_i^{\cdot\cdot\cdot} + V_{Al}^{'''} \qquad (4.6)$$

$$Al_{Mg}^{\cdot} \longrightarrow Al_i^{\cdot\cdot\cdot} + V_{Mg}^{''} \qquad (4.7)$$

and:

$$Mg_{Mg}^{x} \longrightarrow Mg_i^{\cdot\cdot} + V_{Mg}^{''} \qquad (4.8)$$

$$Mg_{Al}^{'} \longrightarrow Mg_i^{\cdot\cdot} + V_{Al}^{'''} \qquad (4.9)$$

For each of these reactions 4.6 through 4.9 one can distinguish between octahedral and tetrahedral interstitial ions. For instance, in the case of aluminium on the ordered lattice sites we have:

$$Al_{Al}^{x} \longrightarrow Al_{i,tet}^{\cdot\cdot\cdot} + V_{Al}^{'''}$$

$$K_{f,Al'} = [Al_{i,tet}^{\cdot\cdot\cdot}][V_{Al}^{'''}]/[Al_{Al}^{x}]$$

$$Al_{Al}^{x} \rightarrow Al_{i,oct}^{\bullet\bullet\bullet} + V_{Al}'''$$

$$K_{f,Al}'' = [Al_{i,oct}^{\bullet\bullet\bullet}][V_{Al}'''] / [Al_{Al}^{x}] \qquad (4.10)$$

However, the ratio of concentrations of these interstitials on structurally nonequivalent sites is found to be a function of temperature only, not concentration, as long as the ideal solution approximation is valid (74):

$$[Al_{i,tet}^{\bullet\bullet\bullet}] / [Al_{i,oct}^{\bullet\bullet\bullet}] = K_{f,Al}' / K_{f,Al}'' \qquad (4.11)$$

This is naturally true also for magnesium interstitials.

It is not known which interstitial site is of lower energy for either magnesium or aluminum in magnesium aluminate spinel, nor is it known which of the reactions 4.6 through 4.9 are energetically favored when the spinel is substantially disordered at high temperatures. At lower temperatures where disorder is small, evidence discussed in the following sections suggests the aluminum Frenkel constant is greater than the magnesium Frenkel constant (i.e. reaction 4.6 is favored over 4.8).

4.3.2 Alumina Excess

The solution of Al_2O_3 in $MgAl_2O_4$ can be accomodated by placing aluminum ions on magnesium sites, $Al_{Mg}^{\bullet}$, with charge compensation accomplished by either aluminum or magnesium vacancies, V_{Al}''' or V_{Mg}''. This can also be viewed as the mixing of spinel with gamma-alumina, which is essentially a highly defective spinel in which 1/9 of the total cation

sites are empty. An alternative interstitial solution mechanism is in principle possible, but all of the available experimental evidence points towards the former.

Jagodzinski and Saalfeld (40) showed using the X-ray Fourier technique that in alumina excess spinel there were indeed cation vacancies, and that they were located predominantly at octahedral sites, i.e. V_{Al}'''. These were observations on samples cooled to room temperature, however, and at higher temperatures there may be both magnesium and aluminum vacancies. (In Fe_3O_4, octahedral vacancies are preferred at low temperatures (91) but in modeling the cation distribution Mason and Bowen (83) assumed a random distribution at high temperature, as have Dieckmann and Schmalzreid (88) in interpreting vacancy regime diffusion) The inversion parameter data of Schmocker and Waldner (72), obtained by electron spin resonance of Cr^{3+} ions in solution on octahedral sites, shows higher "inversion" for an n=3.5 alumina rich spinel than for stoichiometric spinels (Fig. 4.1), and can be interpreted as resulting largely from the presence of aluminium in solution on magnesium sites ($Al_{Mg}^{\bullet}$) rather than cation inversion per se. Other evidence such as the dependence of diffusion (60) and ionic conductivity (57) on alumina excess are also consistent with such a solution mechanism, which we can write as:

$$4Al_2O_3 \rightarrow 5Al_{Al}^{X} + 12O_O^{X} + 3Al_{Mg}^{\bullet} + V_{Al}''' \qquad (4.13)$$

or:

$$4Al_2O_3 \rightarrow 6Al_{Al}^{X} + 12O_O^{X} + 2Al_{Mg}^{\bullet} + V_{Mg}'' \quad (4.14)$$

in the extreme cases where vacancies are only present on octahedral or tetrahedral sites. If we assume a random cation vacancy distribution, the incorporation reaction can be expressed:

$$12Al_2O_3 \rightarrow 16Al_{Al}^{X} + 36O_O^{X} + 5Al_{Mg}^{\bullet} + 2V_{Al}''' + V_{Mg}'' \quad . \quad (4.15)$$

The cation vacancy fraction taken relative to the total number of cation sites is the same in all three cases and is:

$$x_V = (n-1)/(9n+3) \quad (4.16)$$

where n is the Al_2O_3/MgO molar ratio.

4.3.3 Magnesia Excess.

No independent evidence for the solution mechanism of excess magnesia exists, but from the results in magnetite at low oxygen pressures (61,84-86) an interstitial mechanism is to be expected. This can be either magnesium interstitials or aluminum interstitials:

$$4MgO \rightarrow Mg_{Mg}^{X} + 4O_O^{X} + 2Mg_{Al}' + Mg_i^{\bullet\bullet} \quad (4.17)$$

or:

$$4MgO + Al_{Al} \rightarrow Mg_{Mg}^{X} + 4O_O^{X} + 3Mg_{Al}' + Al_i^{\bullet\bullet\bullet} \quad (4.18)$$

for either of which the concentration of interstitials relative to the number of normally occupied cation sites is:

$$x_i = (1-n)/(3n+1). \quad (4.19)$$

Given sufficiently large magnesia excess in solid solution, magnesium interstitials (Eq. 4.17) are preferred. Closer to stoichiometry, aluminum interstitials are dominant if the

aluminum Frenkel constant is greater than the magnesium Frenkel, as shown in the following section. We presume that the alternative solution mechanism involving anion vacancies is too energetic, in comparison with cation interstitials, to be significant.

4.4 The Brouwer Diagram

Schmalzreid (74) has given a general treatment of point defects in ternary ionic compounds which can be applied in constructing the specific Brouwer diagram for magnesium aluminate spinel. Neglecting electronic disorder in accordance with the results of Sonder (53) that electrical conductivity is entirely ionic, and assuming anion defects to be negligible, there are six ionic defects with which we are concerned:

$Al_{Mg}^{\bullet}$, Mg_{Al}', V_{Al}''', V_{Mg}', $Al_i^{\bullet\bullet\bullet}$, $Mg_i^{\bullet\bullet}$

Since it is the variation of defect concentrations with stoichiometry that one is interested in, the Brouwer diagram of interest shows log (defect concentration) vs. log (activity of Al_2O_3), at constant temperature, pressure, and oxygen partial pressure (although for magnesium aluminate the redox equilibrium does not influence the major defect concentrations). Assuming that defect concentrations are equivalent to activities (ideal behavior), six independent defect equilibria are necessary to determine the concentrations.

Consider for the moment a well ordered spinel and thus two cation Frenkel reactions and their corresponding equilibrium constants:

$$Al_{Al}^{X} = Al_i^{\bullet\bullet\bullet} + V_{Al}''' \qquad K_{f,Al}=[Al_i^{\bullet\bullet\bullet}][V_{Al}''']/[Al_{Al}^{X}] \tag{4.20}$$

$$Mg_{Mg}^{X} = Mg_i^{\bullet\bullet} + V_{Mg}'' \qquad K_{f,Mg}=[Mg_i^{\bullet\bullet}][V_{Mg}'']/[Mg_{Mg}^{X}] \tag{4.21}$$

The cation inversion reaction (Eq. 4.1) can be written as the sum of two independent reactions (74):

$$Mg_{Al}' = Mg_i^{\bullet\bullet} + V_{Al}''' \qquad K_1=[Mg_i^{\bullet\bullet}][V_{Al}''']/[Mg_{Al}'] \tag{4.22}$$

$$Al_{Mg}^{\bullet} = Al_i^{\bullet\bullet\bullet} + V_{Mg}'' \qquad K_2=[Al_i^{\bullet\bullet\bullet}][V_{Mg}']/[Al_{Mg}^{\bullet}] \tag{4.23}$$

The following two reactions, combined, allow us to relate defect concentrations to the activity of alumina. The first is the formation of spinel from its component oxides:

$$MgO + Al_2O_3 \rightarrow MgAl_2O_4 \qquad K'=\exp(G^{o}/RT)=a_{MgO}\cdot a_{Al2O3} \tag{4.24}$$

where G_o is the standard free energy of formation. A second is :

$$MgO + 2/3Al_i^{\bullet\bullet\bullet} = 1/3Al_2O_3 + Mg_i^{\bullet\bullet} \tag{4.25}$$

from which we obtain:

$$K_3=a_{Al2O3}^{4/3}[Mg_i^{\bullet\bullet}][Al_i^{\bullet\bullet\bullet}]^{-2/3}\exp(-G^{o}/RT) \tag{4.26}$$

The last condition is that for charge neutrality:

$$3[Al_i^{\bullet\bullet\bullet}] + 2[Mg_i^{\bullet\bullet}] + [Al_{Mg}^{\bullet}] = 3[V_{Al}'''] + 2[V_{Mg}''] + [Mg_{Al}'] \tag{4.27}$$

Choosing two oppositely charged defects at a time in Eq. 4.27 to be the dominant charged species (Brouwer

approximation), two Brouwer or Kroeger-Vink diagrams are possible, depending on whether the aluminum or magnesium Frenkel constant is higher. If $K_{f,Al} > K_{f,Mg}$, the diagram in Figure 4.3 results, with five Brouwer regimes. If the converse is true, Figure 4.4 results, in which regions II and IV are bypassed. The defect concentrations in Figs. 4.3 and 4.4 follow the form:

$$[\text{defect concentration}] \propto [a_{Al_2O_3}]^n ;$$

the exponents for each defect species in Brouwer regimes I through V are tabulated in Table 4.1.

Near stoichiometry (Region III), cation inversion produces the greatest concentration of defects at any reasonable temperature so the charge balance is clearly $[Mg_{Al}'] = [Al_{Mg}^{\bullet}]$.

For alumina excess spinel, Jagodzinski and Saalfeld (40) find evidence for octahedral vacancies in as-cooled spinel. Since the kinetics of re-ordering seem to be relatively rapid above 800°C in natural (stoichiometric) spinels, and should be even more rapid in alumina rich spinel with a high concentration of cation vacancies, high temperature Frenkel defect distributions are presumably not easily frozen in. In that case, the results of Jagodzinski and Saalfeld (40) represent low temperature equilibrium better than high. The presence of octahedral vacancies, then, indicates that the aluminum Frenkel constant is higher than the magnesium, i.e. only Figure 4.3 is consistent with

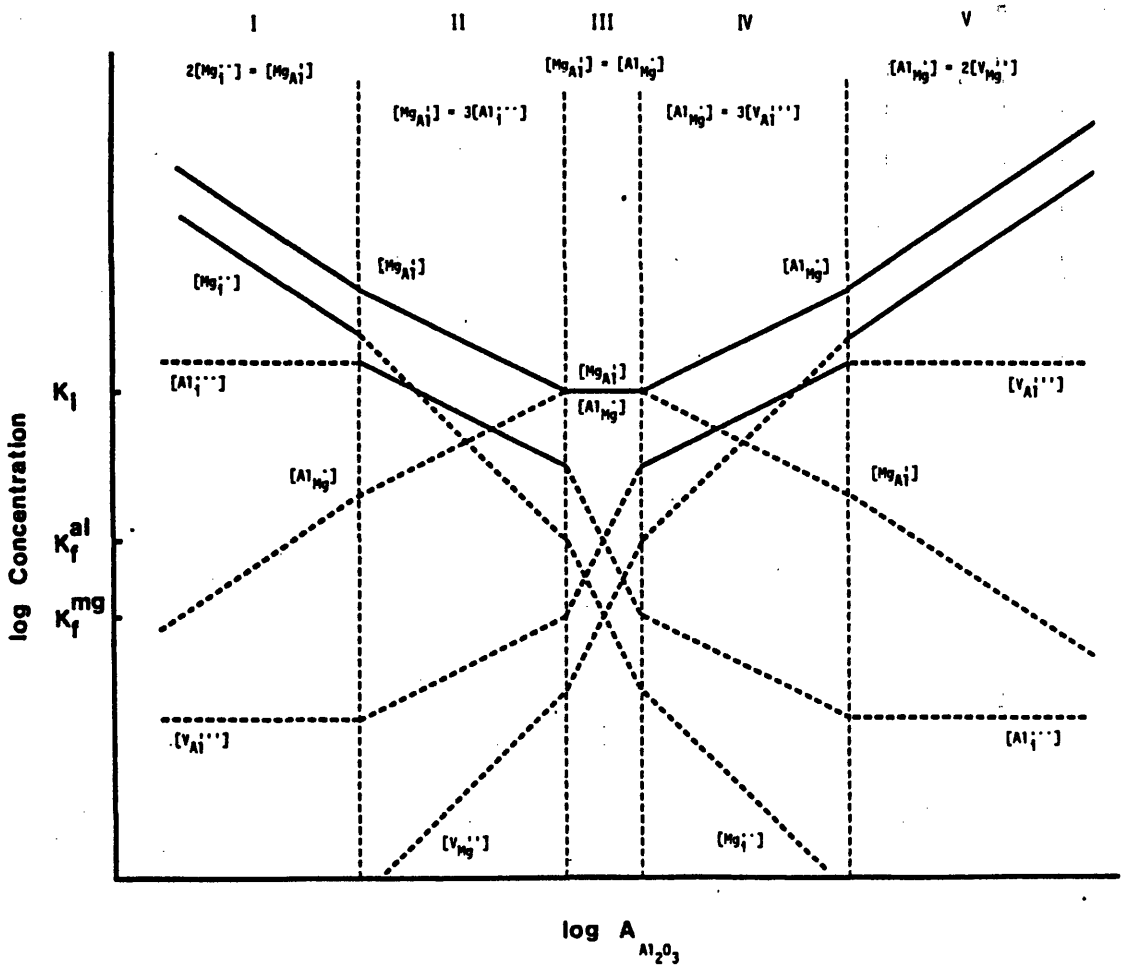

Figure 4.3 Brouwer diagram for magnesium aluminate, with $K_{f,Al} > K_{f,Mg}$.

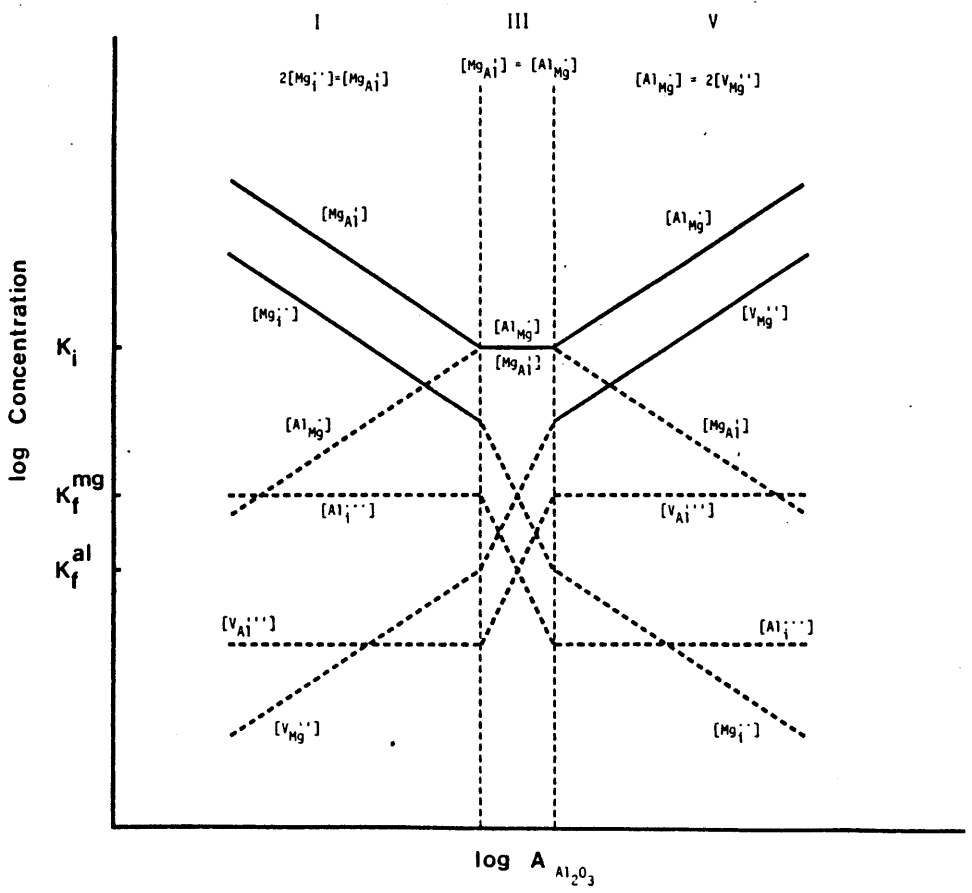

Figure 4.4 Brouwer diagram for magnesium aluminate, with $K_{f,Al} < K_{f,Mg}$.

TABLE 4.1 Dependence of Defect Concentrations on Alumina Activity in the Brouwer Diagram: $d(\ln [\ ])/d(\ln a_{Al2O3})$

	Brouwer Regime:				
Defect	I	II	III	IV	V
$Al_{Mg}^{\bullet}$	+4/3	+1	0	+1	+4/3
Mg_{Al}'	−4/3	−1	0	−1	−4/3
V_{Al}'''	0	+1	+4	+1	0
V_{Mg}''	+4/3	+2	+4	+2	+4/3
$Al_i^{\bullet\bullet\bullet}$	0	−1	−4	−1	0
$Mg_i^{\bullet\bullet}$	−4/3	−2	−4	−2	−4/3

their observations.

An important consequence of the ordering of Frenkel constants $K_{f,Al} > K_{f,Mg}$ is that on the magnesia rich side of stoichiometry, one then must have aluminum interstitials as the most abundant secondary defect. With increasing cation inversion, however, this conclusion is not necessarily valid since one must then include the Frenkel equilibria in Eqs. 4.7 and 4.9 which have not been considered in constructing the Brouwer diagram in Fig. 4.3. It is not possible, with the presently available data, to decide what the relative populations of aluminum and magnesium interstitials in magnesia rich spinel are at high temperature. This is an area where calculations of defect energetics such as have been done for alkali halides and other oxides would be useful; i.e. a comparison of the relative energies of aluminum and magnesium interstitials on octahedral and tetrahedral sites would allow one to decide what form of the Brouwer diagram is appropriate at high temperatures.

Notice that even for $K_{f,Al} > K_{f,Mg}$, with increasing $a_{Al_2O_3}$ eventually magnesium vacancies must overcome the aluminum vacancies (Region V), unless the phase boundary is first reached. Similarly, on the magnesia excess side, Region II, both aluminum and magnesium interstitials increase with magnesia excess although the latter does so more steeply, and eventually magnesium interstitials will dominate also (Region I) if the phase boundary is not crossed first.

Let us compare the actual defect concentrations introduced with deviation from stoichiometry to the phase boundary compositions to determine which of the Brouwer regimes are actually included in the single phase field of spinel at various temperatures. In Fig. 4.5 we have plotted defect concentrations resulting from nonstoichiometry (as fraction of the total number of cation lattice sites) against spinel composition, derived from the solution mechanisms for excess alumina and magnesia in Eqs. 4.13 and 4.18. Depicted also is the concentration corresponding to a random cation distribution, the degree of inversion observed by Schmocker et al. (71), and the phase boundaries at 1200° and 1800°C. On the magnesia rich side, if we take the total Mg_{Al}' concentration to be approximately the sum of that from inversion and magnesia excess, the charge neutrality condition of Brouwer regime II ($[Mg_{Al}'] = 3[Al_i''']$) is not attained even for the phase boundary composition at 1800°C. Similarly on the alumina rich side, if the total $Al_{Mg}^{\bullet}$ is approximated as the sum of that from inversion and alumina excess, Brouwer regime IV where $[Al_{Mg}^{\bullet}] = 3[V_{Al}''']$ is not yet reached at 1800°C. Assuming a random cation vacancy distribution (Eq. 4.15) does not change this conclusion. Thus, Brouwer regime III is in fact the only one encompassed by the single phase composition field except at temperatures exceeding 1800°C.

At higher temperatures the single phase field does widen

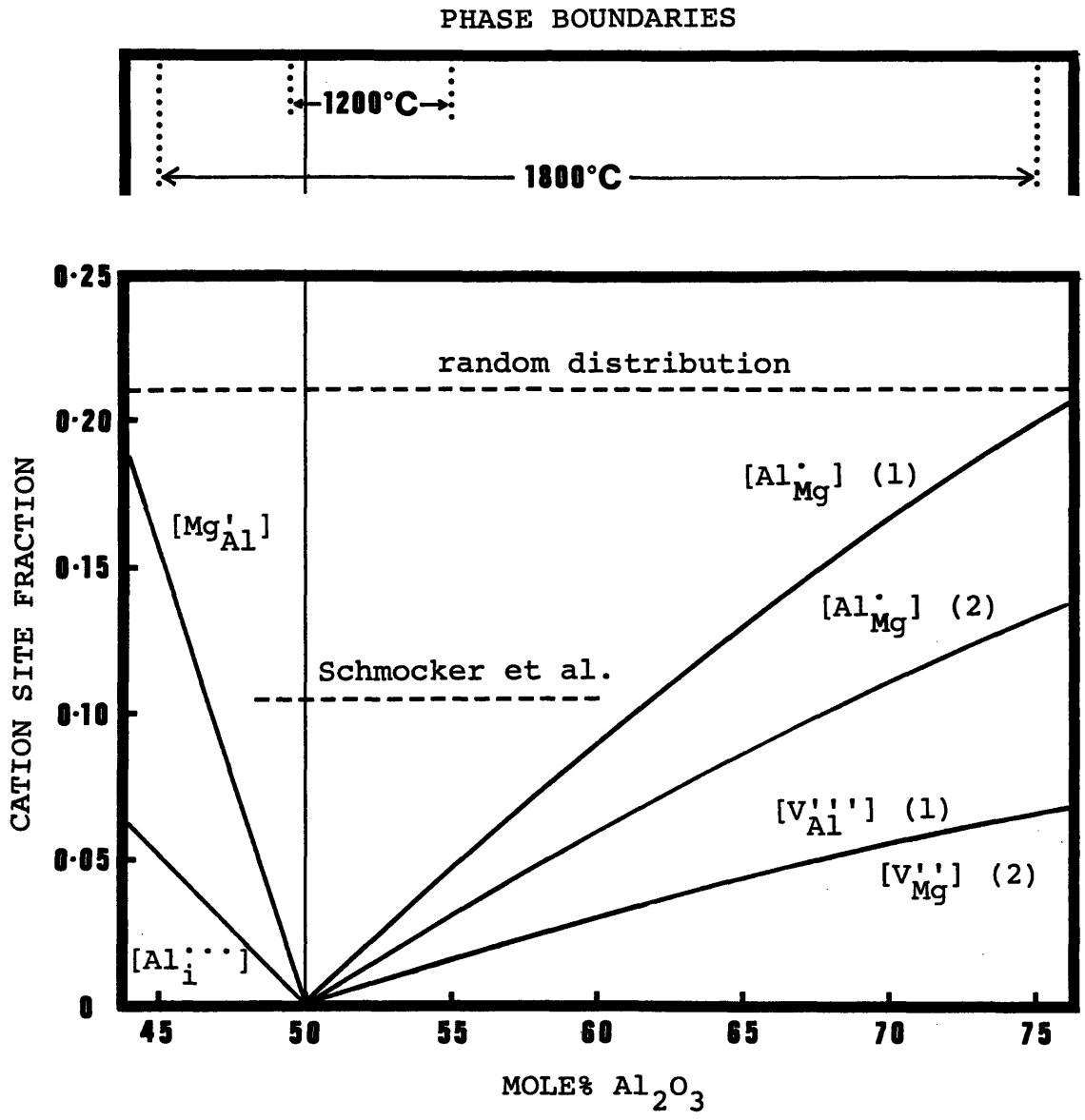

(1) In solution as $Al^{\bullet}_{Mg}$ and V'''_{Al}

(2) In solution as $Al^{\bullet}_{Mg}$ and V''_{Mg}

Figure 4.5 Defect concentrations introduced by deviation from stoichiometry in magnesium aluminate.

markedly (Fig. 3.2) and regions II and IV are possible. Within the experimental temperature range in this work of 1200°-1800°C, however, cation inversion does indeed dominate the defect concentrations in the single phase field.

It is interesting also that the calculated defect concentrations do not differ appreciably at the two phase boundaries; i.e. although magnesia is much less soluble in spinel than alumina on a molar basis, on a per defect basis this is not really true.

4.5. Defect Association

Thus far we have not included the possible effects of defect association. In magnetite, ideal solution behavior is observed up to vacancy concentrations at the phase boundary of ≈1 mole % between 1200° and 1400°C (61,85). In the present system the defect concentrations due to cation inversion and nonstoichiometry in spinels can reach such high levels (≈20%) that some fraction will be by definition associated simply because they cannot avoid one another, and the applicability of point defect theory should be questioned. Nonetheless, Schmalzreid (74) has shown that there is evidence that negligible interaction between defects occurs in certain systems, including magnesium aluminate, and for these the formalism of point defects is applicable.

The equilibrium constant for cation inversion:

$$K_I=[Al_{Mg}^{\bullet}][Mg_{Al}']/[Al_{Al}^{x}][Mg_{Mg}^{x}]$$

is not defect concentration independent if association between, for instance, $Al_{Mg}^{\bullet}$ and Mg_{Al}' or $Al_{Mg}^{\bullet}$ and V_{Al}'''species occurs. However, in $MgFe_2O_4$ and $CuFe_2O_4$, magnetic measurements show K_I to be concentration independent up to high degrees of disorder (74), indicating negligible defect interactions.

Analysis of the temperature dependence of the single phase field boundary provides another indication (74). The deviation from stoichiometry, $\delta=(n-1)$, is proportional to the concentration of the majority defects. Since these defect concentrations are given by equations of the form:

$$d \ln [i] = n_i \, d \ln a_{Al2O3} \qquad (4.28)$$

if ideal behavior holds, integration of Eq. 4.28 from stoichiometry to the phase boundary composition where $a_{Al2O3} = 1$ yields:

$$\ln \delta_{sat} \propto \ln [i_{sat}]/[i_o] \propto \ln a_{Al2O3,o} \propto 1/T \qquad (4.29)$$

where the subscript 'sat' refers to the saturated phase boundary composition and 'o' refers to stoichiometry. As a result the deviation from stoichiometry at the phase boundary is a function of temperature only and not defect concentration so long as defect interactions are negligible. Schmalzreid (74) has shown that a plot of $\ln \delta_{sat}$ vs. 1/T is indeed linear for magnesium aluminate in equilibrium with alumina from 1000°-1800°C, suggesting little defect interaction despite very large vacancy concentrations at the higher temperature phase boundary compositions as shown in

Fig. 4.5. For nickel aluminate in equilibrium with aluminate, the same linearity is found. Note that these observations show only that the relative concentration of defect associates compared to the total point defect concentration is low; the absolute concentrations may well be very high compared to, for instance, a highly stoichiometric binary oxide such as MgO. Although this analysis is rather indirect, it does show that in the composition range close to stoichiometry which we are more interested in, the likelihood of defect interactions affecting the defect equilibria as formulated above and as shown in Fig. 4.3 is small.

4.6. Summary

The dominant point defects in spinel are ionic and are confined to the cation sublattice. Substitutional defects resulting from cation inversion are the most abundant across the single phase field compositions; these are followed by Frenkel pairs at stoichiometry, cation vacancies in alumina excess spinel, and cation interstitials in magnesia excess spinel. At low temperatures the Frenkel constant for aluminum is higher than that for magnesium, and as a result aluminum vacancies and aluminum interstitials are respectively the dominant secondary defects introduced with excess alumina and magnesia. At high temperatures, randomization of cation vacancies in alumina rich spinel is likely, and cation inversion introduces additional Frenkel

equilibria about which there is presently insufficient data to allow positive conclusions regarding the relative populations of aluminum and magnesium interstitials.

V. EXPERIMENTAL PROCEDURE

5.1 Sample Preparation

5.1.1 Powder Synthesis

Samples were desired in which the composition is uniform throughout on a microscale and the microstructure dense and fine-grained. It was found that processing similar to that developed by Henriksen (92) for MgO, in which the metal hydroxide is precipitated from aqueous nitrate solutions, yielded spinel powders suitable for hot-pressing. Good spinel powders can also be prepared from sulfates (93); however early experiments on a Baikowski* alum-derived powder showed undesirable segregation of residual sulfur at grain boundaries after hot pressing.

Powders were prepared in acid-cleaned polyethylene or polypropylene vessels wherever possible; reagent grade solvents were used throughout. Magnesium nitrate ($Mg(NO_3)_2.6H_2O$) and aluminum nitrate ($Al(NO_3)_3.9H_2O$), in nominal proportions for a desired composition and yield of about 40 g. powder, were dissolved at room temperature in 400 ml distilled water + 120 ml acetone. The metal hydroxide was precipitated from this solution by adding slowly a mixture of 400 ml ammonium hydroxide, 120

* Baikowski International Corporation, Charlotte, North Carolina.

ml distilled water and 100 ml acetone, while stirring the solution rapidly with a Teflon coated magnetic stir-bar in a 1 gal. polypropylene jar. The hydroxide precipitated immediately, but the mixture was allowed to digest for another 5 min. while stirring before excess liquid was filtered off through a Pyrex fritted glass filter funnel lined with filter paper. The gel-like precipitate was removed before any dryness occurred and returned to the polypropylene jar.

A three step rinsing procedure commenced in which the hydroxide precipitate was: 1) dispersed by stirring in acetone, filtered to near-dryness; 2) redispersed in toluene and filtered; 3) redispersed in acetone again and filtered to dryness. This sequence of rinsing which does not allow the gel cake to dry is believed to remove interlamellar water from between the hydroxide platelets and to allow calcination to a less agglomerated powder (94).

The powder was then dried in polyethylene beakers covered with several layers of filter paper in a drying oven at 60°C, and calcined in high purity MgO crucibles* at 800°-1000°C for ≈2 h. in air. Yield was typically greater than 95% of the nominal batch size. The resulting loose, friable oxide powder cakes were lightly crushed in a high

* Honeywell Corporation, Golden Valley, Minnesota.

purity alumina mortar and pestle prior to hot pressing. Figure 5.1 shows SEM micrographs of a magnesia rich (a) and an alumina rich (b) calcined powder; despite the precautions both are highly agglomerated. It was found that the magnesia rich powders exhibited much larger particles than the alumina rich, as is evident in Figure 5.1, where the magnesia rich powder also appears to have sintered considerably at the calcining temperature. Bagley (95) has also observed this disparity in powder particle size as a function of stoichiometry in alum-derived spinel powders.

Certainly these powders are not morphologically ideal; the high degree of agglomeration would probably cause great difficulties were this a sintering experiment. However, they proved to be compositionally accurate as formulated, homogeneous on a microscale, and adequate for hot pressing to fully dense, fine grained samples. Therefore, pragmatism prevailed and no further attempts were made to characterize and refine the powder processing.

5.1.2 Characterizing Powder Stoichiometries

The compositions of the calcined powders were calibrated through Debye-Scherrer X-ray lattice parameter measurements. The details of the measurements are described in Appendix 1. Many workers have reported that the lattice parameter of magnesium aluminate spinel decreases with increasing alumina in solid solution; Wang (96) and Yamaguchi et al. (97) have

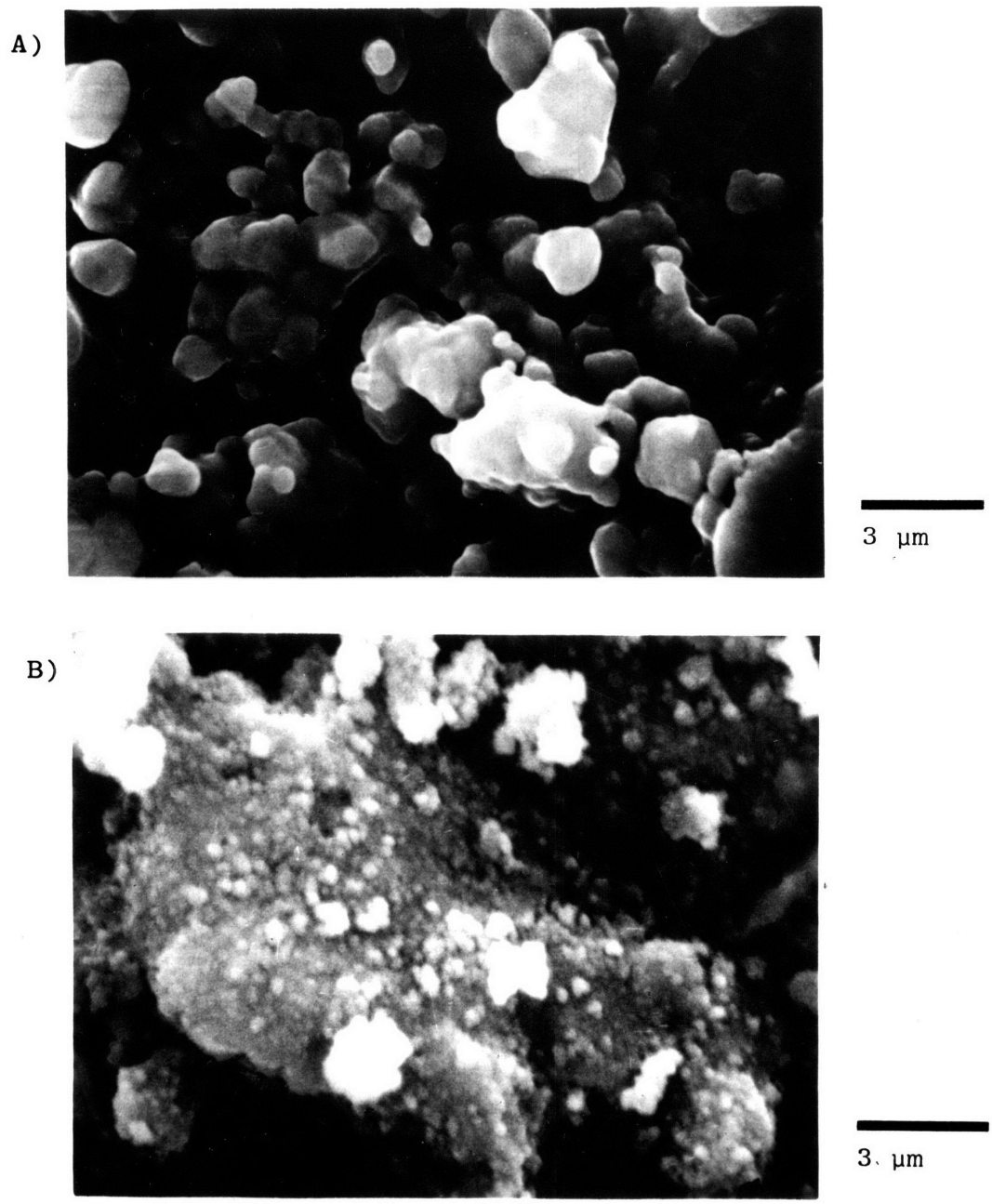

Figure 5.1 SEM micrographs of as-calcined, nitrate derived a) magnesia rich, and b) alumina rich spinel powders.

determined the variation to be very linear over a wide composition range and find Vegard's law constants that agree closely (-4.6×10^{-2} and -4.9×10^{-2} nm per mole% excess Al_2O_3, respectively). Their data and data from powders we have prepared are shown in Fig. 5.2 as lattice parameter vs. mole% Al_2O_3. Since it has also been reported (70) that the lattice parameter changes slightly with temperature due to cation disorder, for consistency in our measurements all powders were annealed at 1600°C for 1/2 hour in air and rapidly air-cooled, prior to X-ray analysis.

One sees in Fig. 5.2 that the absolute values of lattice parameters determined by Wang (96) and Yamaguchi et al. (97) do not agree very well; aside from the temperature variation, it is generally agreed that the relative precision of lattice parameter measurements is much better than the absolute accuracy (98). Thus, the Vegard's law constant is far more reliable than the actual lattice parameter value. For our powders, lattice parameters from alumina rich samples yielded a Vegard's law constant of 4.7×10^{-2} nm per mole% excess Al_2O_3 (least squares fit against nominal composition), in good agreement with the literature (96,97).

In magnesia excess spinel solid solutions, Alper et al. (52) have found that the lattice parameter is invariant with composition up to stoichiometry, and our findings confirm this (Fig. 5.2). The lattice parameter of stoichiometric spinel was determined to be as 8.0825 angstroms. Upon

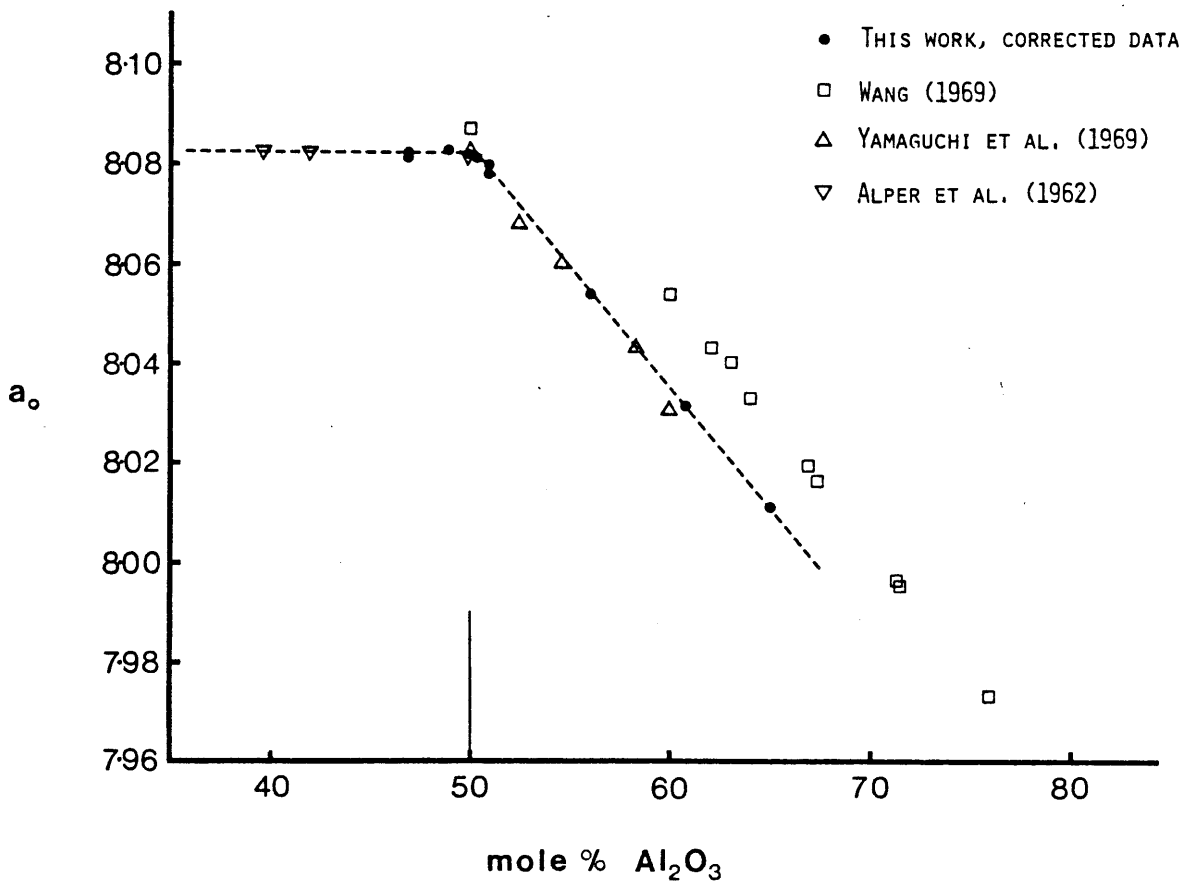

Figure 5.2 Lattice parameter vs. composition for spinel.

extrapolating from stoichiometry to alumina rich compositions using the experimental Vegard's law constant, all of the alumina rich powders were found to be approximately 1 mole% greater in alumina than the nominal compositions. We presume that this trend persists to stoichiometric and magnesia rich compositions, as they were processed in the same way. Thus, in this work the magnesia excess powders have been assigned compositions 1 mole% greater in alumina content than the nominal composition on the basis of this processing consistency. The accuracy of this determination is about +/_ 0.2 mole% alumina for samples not too far from stoichiometry. The compositions of alumina excess powders were determined solely from the Debye-Scherrer measurements.

Attempts to have the compositions confirmed by atomic absorption spectroscopy and inductively coupled plasma emission spectroscopy (ICP) were unsuccessful since these techniques proved far less accurate than the lattice parameter determinations. Wet chemical analysis was not attempted due to insufficient amounts of powder remaining after sample preparation and annealing. However, a final check on the relative compositions of powders is the Al/Mg ratios observed in the STEM measurements. They were consistent with the above results.

Trace elements were analyzed with ICP emission spectroscopy. Typical results for the elements in greatest concentration are shown in Table 5.1.

TABLE 5.1 Trace element analysis of nitrate-derived spinel powders.*

Sample Stoichiometry	wt ppm							
	Ca	Fe	Ga	Mn	Na	Si	Ti	Zn
Stoichiometric	119	151	50	3.4	99	75	17	<7
n=1.036	114	184	53	4.7	137	48	16	7.6
n=1.56	128	164	61	4.1	217	59	19	18

* Performed by Walter Zamechek, Union Carbide Corporation, Tarryton, New York.

5.2 Hot Pressing

In order to attain the smallest possible starting grain size commensurate with sufficiently high density to preclude pore drag as a mobility limiting mechanism, samples were hot pressed rather than sintered. However, two special procedures were undertaken to ensure high density and sample cleanliness: platinum encapsulation, and the use of spinel crystals imbedded in the powder to magnify the applied pressure.

Preliminary experiments indicated substantial carbon contamination would result from the graphite die upon hot pressing, which caused severe bloating when annealing samples afterwards. Equally seriously, it was felt that contamination of the samples by impurities carried in the graphite might occur. To avoid both of these problems without resorting to high purity graphite and/or other die materials, a means to encapsulate samples in platinum foil was developed.

Capsules were formed from 0.001" thickness platinum foil in cylindrical form (0.75" diameter by 0.5" height, see Figure 5.3). A flat lid of the same foil covered the capsule, and the rim was crimped tightly with sample inside, except for a small segment of the edge where the foil was loosely folded. This opening allowed the capsule to be evacuated and de-gassed before hot pressing, but could be easily sealed upon applying the load. The encapsulated sample was also prefired in air at 500°C in air prior to

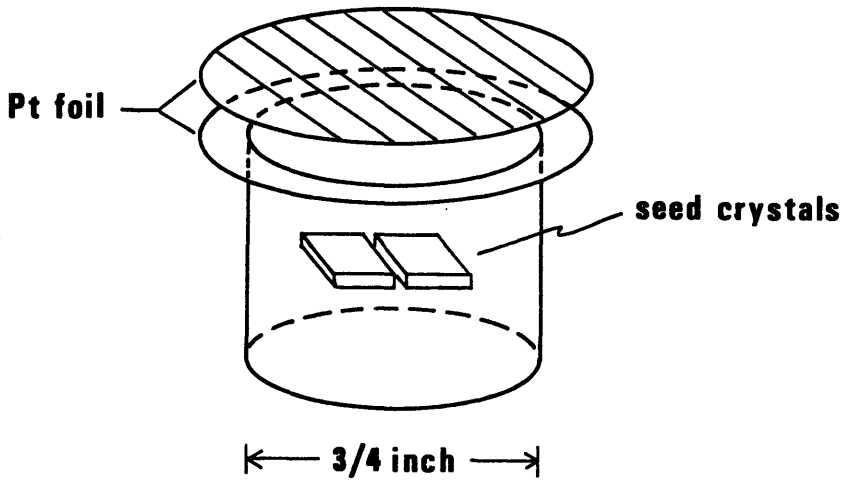

Figure 5.3 Schematic of platinum foil capsule and lid used for encapsulation during hot-pressing.

loading in the graphite die. In the die (of 1" diameter), the capsule was surrounded by commercial Baikowski Corp. stoichiometric spinel powder.

Two seed crystals cut in rectangular plate form (5mm x 10mm x 1mm) from a stoichiometric spinel single crystal boule* were embedded in each sample. This was initially done so that secondary recrystallization rates could be measured simultaneously with grain growth rates, and these seed crystals were wrapped with 0.004" platinum wire to serve as markers. However, this part of the experiment was unsuccessful for two reasons. First, in high mobility samples the matrix grain size increased very rapidly, and this lowered driving force combined with problems with attached pores at the recrystallizing interface did not allow migration of the interface further than a grain diameter or so. Secondly, in low mobility samples it was found that no pores were left to mark the original interface, and the migration distances were too small for the comparatively coarse platinum wire to serve accurately as markers. In neither case was reliable mobility data obtainable.

However, the seed crystals served the alternative useful function of magnifying the applied pressure by about a factor of five (based on the area reduction). Since the graphite dies used could not safely exceed about 5 ksi, this increase

* Union Carbide Corporation.

in pressure to ≈25 ksi turned out to be very useful in achieving fully dense (transparent) regions on the faces of the seed crystals, and so the practice of using seeds was continued.

Hot pressing was done at temperatures in the range 1250°-1450°C for times from 1 to 4 hours. In Figure 5.4 is shown the crossection of a sample after hot pressing, in which the outline of the capsule, the seeds, wire markers, and the dense regions on the seed faces can be seen.

5.3 Other Samples

In addition to the samples that were fabricated from nitrate-derived powders as above, a number of experiments were also conducted on a nearly stoichiometric sample hot pressed by W.H. Rhodes (GTE Laboratories) from a nitrate derived powder. This sample had been hot pressed at 1400°C and 15 ksi for 1 hour; the Al_2O_3/MgO molar ratio was determined via Debye-Scherrer analysis (on a sample annealed identically to our powders) to be 1.013. The starting powder for this sample is quite pure, with major impurity levels reported as:

Na	<148	wt. ppm
Si	42	"
Ti	18	"
Cr	< 7	"
Fe	42	"
Ni	<39	"

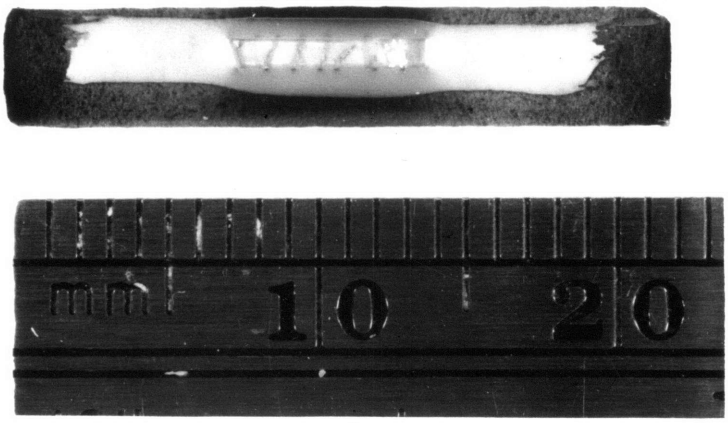

Figure 5.4 Cross section of as hot-pressed, seeded, spinel sample.

Calcium was not reported for this particular analysis, but other powders from the same source contained detectable amounts. The STEM analyses (to be presented later) indicated there was some impurity calcium. The as-hot pressed microstructure of this sample was dense (99.4% by immersion) and uniformly fine grained (0.64 μm linear intercept grain size). It was suitable in every way for our purposes.

Limited observations were also made on a magnesia-rich sample (n=0.909) prepared and annealed by R.D. Bagley (Corning Glass Works). This sample was prepared from alum-derived powders and fired at 1805°C in hydrogen for 20 min., following which it was polished and thermally etched at 1525°C for 7 min. in hydrogen.

5.4 Grain Growth Anneals

The hot pressed samples were sectioned into small specimens approximately 4mm x 3mm x 1.5mm for grain growth anneals. All specimens were cleaned prior to annealing by immersion in hot orthophosphoric acid at ≈180°C, followed by rinsing in: 1) distilled water + hydrochloric acid (4:1); 2) distilled water alone; 3) reagent grade methanol.

Despite the encapsulation procedure, bloating occurred occasionally in certain samples, indicating that we were not completely successful in excluding carbon. For consistency of heat treatment between samples, all anneals were therefore conducted in flowing hydrogen (pre-purified grade, 1-3 ppm

oxygen as received).

A molybdenum wound furnace with a verticle alumina tube* was used. Brass fittings with rubber gaskets sealed the top and bottom of the alumina tube, except for a gas inlet port at the top, gas outlet port at the bottom, and a small hole in the top fitting just sufficient to admit a sample lowering and raising wire. The top fitting had a quartz window for observation. Temperature was recorded with a Pt/Pt+10%Rh thermocouple that was protected by a close-ended alumina tube** which extended from the bottom fitting up into the hot zone. An electronic cold junction compensator *** was used with the thermocouple, power was controlled with a variac and temperature manually regulated to +/-5°C.

For each anneal, the sample was packed in powder of the same composition in a molybdenum foil envelope (15mm x 15mm x 5mm) and suspended on a molybdenum wire hanger inside the sealed furnace tube. The furnace was then purged with argon. Hydrogen was substituted for the argon, and after ≈1/2 h. the sample was lowered to the edge of the hot zone to outgas for 15 min.. It was then lowered into the hot zone, immediately adjacent to the thermocouple. A small positive hydrogen

* Morganite recrystallized alumina.

** McDanel 99.8% alumina, McDanel Refractory Porcelain Co., Beaver Falls, Pennsylvania.

*** Omega Engineering, Stamford, Connecticut.

pressure was maintained inside the furnace tube throughout the anneal, monitored by the flow rate of gas through a bubbler. At the end of the anneal, the sample was rapidly pulled to the top of the furnace tube where a high flow rate of argon was simultaneously introduced through the gas inlet port. Thus the samples can be considered to be rapidly gas-cooled, with an estimated quench rate of several hundred degrees per second.

A few samples were also annealed in air without encapsulation, then quenched from the hot zone directly into a water bath, for the purposes of examining if cooling rate effects were important. The mass of these samples is sufficient that little temperature drop occurrs during free fall. The quench rate once the sample strikes the water bath is $\approx 10^4$ °C/sec. (99), and was always sufficient to cause the samples to fracture into small pieces.

5.5 Microstructural Examination

To examine microstructure and measure grain sizes, the samples were polished to a 1/4 μm diamond finish, then ultrasonically cleaned in acetone and etched with fresh, hot orthophosphoric acid (H_3PO_4) at 180°C for time ranging from 2 to 10 minutes. Fine grained samples to be examined by scanning electron microscopy (SEM) were etched for shorter times than the coarser grained samples examined by light microscopy. Samples were rinsed in distilled water +

hydrochloric acid (4:1) after the hot acid etch, followed by rinsing in distilled water alone and then reagent grade methanol. A thin layer of gold (≈20 nm) was sputtered on all samples, to increase reflectivity for light microscopy or to prevent charging in the SEM.

The average grain size G_a was determined for each sample from the average intercept length, L_a, of at least 150 grains, using the conversion $G_a = 1.5L_a$ (100). The grain boundary mobility was determined according to Eq. 2.4, assuming 1000 ergs/cm^2 for the boundary energy in all cases.

5.6 STEM Sample Preparation and Analysis

5.6.1 Preparation of Samples

STEM specimens were prepared from sections cut from the center regions of annealed grain-growth samples with a wire saw or diamond coated disc saw. These sections were ground to 20-30 μm thickness with diamond paste (6 μm) on a glass plate, followed by ion thinning (Gatan model 600 ion mill) to perforation with 4-6 keV Ar^+ ions. All samples were mounted on copper grids for ion thinning and electron microscopy, and coated with a thin layer of evaporated carbon to prevent charging under the electron beam.

5.6.2 STEM Analysis

5.6.2.1 Instrumental

The scanning transmission electron microscope used is a Vacuum Generators* HB5 equipped with a Kevex Corp. (Foster City, CA) beryllium-window energy dispersive X-ray detector. The use of a virtual objective aperture and a beryllium specimen holder minimized spurious X-rays. As the specifications and capabilities of this instrument have been extensively reviewed elsewhere (101) we will only summarize the essential points.

A field-emission electron gun (operating at 100 kV) is utilized for maximum source brightness; i.e. a minimum probe size with sufficient beam current ($\approx 10^{-8}$ A). The electron probe is focused to ≈3 nm diameter and rastered across the sample for imaging, but can be fixed at any one point for microanalysis of a very small volume of material. The effective spatial resolution is discussed in more detail below (section 5.6.2.4), but it is about 5 nm in light metal oxides such as MgO and $MgAl_2O_4$. In determining the grain boundary segregation profile the probe is usually stepped normal to the boundary in spacings of 5 nm near the boundary and 10-20 nm further away, and an energy dispersive X-ray spectrum collected at each point. Quantification procedures are discussed in section 5.6.2.3.

* Vacuum Generators, East Grinstead, U.K.

The criteria by which one judges whether a given grain boundary is appropriate for analysis are many, and not often is the completely ideal boundary found. However, the following guidelines were followed for finding suitable boundaries:

1) The sample was tilted towards the X-ray detector to an angle of about 30° from the horizontal.

2) Boundaries in uniformly thin regions with a bright field projected image width of less than 30 angstroms were selected. Tilting allowed alignment of the boundary plane as nearly parallel as possible to the electron beam, within the bounds set in 1). Care was taken to avoid obstructions such as grid bars and thick sample regions in the path between the analyzed region and the detector.

3) Whenever possible, boundaries oriented to point towards the X-ray detector were chosen. This is usually done to avoid fluorescence effects between grain boundary and matrix elements, but for the compositions analyzed in this work this is not very important, and this guideline was often violated.

4) The orientation of each grain adjacent the boundary was examined with microdiffraction prior to grain boundary profiling to ensure that a strongly diffracting condition did not exist. This was done because recent experimental (102) and theoretical (103) work has shown that strongly excited beams lead to asymmetry in the total intensity profile as the

beam propagates through the solid, and can lead to anomalously skewed segregation profiles. The situation is worse for strongly excited beams in the direction of the boundary than for beams diffracted away from the boundary (102).

5.6.2.2 Electron Beam Damage

In thin foil sections, visible beam damage was sometimes observed when the probe was fixed in position for greater than ≈15 seconds. Along with the contrast change at the irradiated spot, there was sometimes an increase in the detected Al/Mg ratio.

This problem was circumvented by avoiding very thin foil regions, and by adopting the following probe placement procedure. Instead of fixing the probe at one point for the 30-60 seconds necessary to collect data, the probe was moved parallel to the boundary to an unirradiated spot every five seconds, maintaining the same distance from the boundary. As a further precaution, in between each spectrum the beam was either deflected or the scan area greatly enlarged to minimize beam time on the sample. Data collected in this manner was reproducible both at different points along the same boundary and between boundaries in the same sample, and seems to be representative of the true composition profile, whereas the usual probe placement procedure often yielded non-reproducible and scattered data.

It is not clear what the cause of beam damage was. Typically such effects are due either to irradiation induced atomic displacements, or to electron beam heating, or both. However, the literature suggests that neither of these is important under the present conditions, as discussed below.

Fast neutron and electron (1 MeV) irradiation damage in magnesium aluminate spinel has been recently studied by Parker (104). The primary atomic defect creation mechanism in electron irradiation was concluded to be isolated electron-atom collision displacements resulting in single Frenkel pairs. Radiolysis is thought to be unimportant in this oxide. Parker (104) estimated the displacement energies of oxygen, magnesium and aluminum atoms as 60, 60 and 20 eV respectively. Therefore, in order to create defects the electrons must transmit this threshold amount of energy or more to the atom.

An upper limit to the energy transferable by an electron of energy E and mass m to a target atom of mass M is (105)

$$F_{max} = 2E(E+2mc^2)/(Mc^2)$$

where c is the velocity of light. For the most easily displaced atom, Al, for 1 MeV electron irradiation F_{max} = 160 eV and considerable damage is likely, as Parker (104) observed. At 200 keV, F_{max} = 19.4 eV, and some defects may be created since the threshold is not sharp, atom displacement being a statistical process. However, Parker (104) used a 200 kV electron microscope (JEOL 200CX) to

observe extended defects created at the higher energy (1 MeV) and observed no further in-situ damage. At 100 kV as we have used in the STEM, F_{max} = 8.9 eV, and virtually no damage is to be expected.

The increase in sample temperature for a flat, uniformly thick film that is thermally well anchored at its edges has been obtained by solving the radial form of the differential equation for heat conduction to be (105)

$$T_{max} = b^2/2ke[j_p(dU_p/dz)/e](1/2 + \ln s/b)$$

where j_p is the beam current density ($\approx 3 \times 10^9$ A/m^2 for the STEM probe), k is the thermal conductivity (17 J/m.sec.K at 300K, E15), dU_p/dz is the energy loss rate with depth for 100 keV electrons (2×10^8 eV/m, E14), b the beam diameter ($\approx$2 nm) and s the distance from the irradiated spot to the heat sink ($<\approx$1mm). The T_{max} calculated thusly is a negligible 1K or so. If a segment of sample is not of the assumed geometry, for instance if it is on a peninsula of material attached via a narrow heat conducting path to the rest of the sample, the heating may be much more severe and in fact melting can occur. The areas of samples examined and profiled in the STEM were not of this configuration, and since good thermal contact to the folding copper grids can be assumed, it is difficult to attribute the cause of damage to beam heating.

One speculation regarding the source of damage is that atoms may be removed from the sample surface where atom

displacement energies are less, and in particular where electron-induced desorption can take place (106,107). Thus, the sample is in effect sputtered by the electron beam. This explanation is not inconsistent with our observations and is by default the most probable mechanism, but we cannot at present prove it to be the cause; here again the emphasis was on circumventing the irradiation problem and proceeding with the work at hand rather than studying the damage effects in detail.

5.6.2.3 Quantification of X-ray Data.

Quantitative interpretation of observed segregant profiles involves consideration of two issues; one must first determine how the X-ray intensities are related to composition, and then determine how the observed intensities are related to the actual segregant distribution given a finite instrument spatial resolution which samples both the grain boundary and the matrix simultaneously. We will discuss the first of these questions in this section, and the second in the following section.

The ratio of integrated X-ray intensities (after semi-empirical background subtraction) for two elements a and b are directly related to their concentration ratio by what is often referred to as the Cliff-Lorimer equation:

$$C_a/C_b = K_{ab} \ (I_a/I_b) \qquad (5.1)$$

where I_a and I_b are the X-ray intensities, C_a and C_b the

weight fractions of a and b, and K_{ab} is a constant at constant instrument voltage. K_{ab} can in principle be calculated if the detector absorption characteristics are known precisely (108), and also experimental values for particular instrument-detector combinations have been published (108), but these are not strictly applicable to other microscope environments and other energy dispersive detectors of different efficiencies. The most accurate means of calibrating K_{ab} values is with a standard of known composition under identical experimental conditions to the sample of interest.

In magnesium aluminate spinel the sample serves as its own standard for determining relative changes in Al/Mg at grain boundaries. Other elements we will be concerned with are Si and Ca, and for quantifying these, two standards have been used. For Si, a synthetic forsterite crystal (Mg_2SiO_4) was obtained*, and for Ca an calcium aluminate standard ($CaAl_2O_4$) was prepared. (This was done by wet-ball-milling the component oxides CaO and Al_2O_3 in isopropanol in a polypropylene jar with Teflon media, drying the mixture, isostatically pressing the powder at 40 ksi, and firing at 1625°C for 6 hr. in air.) The two standards were crushed and ground in an agate mortar, then deposited on carbon support films for microscopy. The K_{ab} values derived from these

* Grown by Dr. Takei at the Tohaku University, Japan.

TABLE 5.2. Cliff-Lorimer Constants Measured from $MgAl_2O_4$, Mg_2SiO_4 and $CaAl_2O_4$.*

Elemental Ratio (A/B)	K_{AB}
Si/Mg	0.843 +/- 0.049
Ca/Mg	0.698 +/- 0.075
Al/Mg	0.765 +/- 0.032

* The same X-ray energy windows are used here as for the analysis of spinel samples:

Mg	1.18-1.30 keV
Al	1.42-1.54 keV
Si	1.72-1.80 keV
Ca	3.60-3.76 keV

standards and from $MgAl_2O_4$ for the elements of interest are given in Table 5.2, where the limits of error for K_{ab} are calculated on the basis of X-ray counting statistics assuming no error in the specimen compositions.

Equation 5.1 for the ratio method holds only if absorption of x-rays in the sample is neglible. If this is not so, the observed X-ray intensities vary with sample thickness and an absorption correction to Eq. 5.1 is necessary (108,109):

$$C_a/C_b = K_{ab} \ (I_a/I_b) \ \exp[-(pt/2)(X_a-X_b)] \qquad (5.2)$$

where

$$X_i = \mu/p)^j_{spec}(\csc \alpha).$$

Here p is the density, t the foil thickness, $\mu/p)^i_{spec}$ is the mass absorption coefficient of the specimen for element i, and α is the detector take-off angle (33° for the HB5). The mass absorption coefficient is determined from:

$$\mu/p)^i_{spec} = \Sigma_j \ x_i \ \mu/p)^i_j \qquad (5.3)$$

where x_j is the weight fraction of element j in the specimen and $\mu/p^i)_j$ is the mass absorption coefficient of element j for the characteristic peak i of interest.

There is, however, a "thin-film limit" of the specimen thickness below which absorption is negligible, which for the ratio technique is given by (109):

$$(X_a-X_b)pt < 0.2 \qquad (5.4)$$

In Table 5.3 we have calculated the thin film limits for elemental ratios of interest in $MgAl_2O_4$, $CaAl_2O_4$, Mg_2SiO_4,

TABLE 5.2. Calculated Thin-Film Limits for Spinel Samples and X-ray Standards.

Composition	Elemental Ratio	Thin Film Limit (angstroms)
$MgAl_2O_4$	Al/Mg	54000
	Si/Mg	4000
	Ca/Mg	2280
$CaAl_2O_4$	Ca/Al	3300
Mg_2SiO_4	Si/Mg	75000
$CaSiMgAl_{2.67}O_4$	Ca/Mg	2317
	Si/Mg	26000
	Al/Mg	8526

and a hypothetical grain boundary composition of $Ca_{0.5}Si_{0.5}Mg_{0.5}Al_{1.33}O_4$. The mass absorption coefficients have been taken from Bracewell and Veigele (110). These results indicate first of all that the thin-film limits for the standards used are large enough that absorption can be neglected, as long as the X-ray data are taken from thin foil regions (such as the edges of particles, for the powder samples). It is also seen that for either $MgAl_2O_4$ or $CaSiMgAl_{2.67}O_4$, absorption is not a problem for thicknesses in our experimental range of 1500-3500 angstroms. Ca/Mg has thin film limits of about 2300 angstroms; for a 3500 angstrom foil Eq. 5.2 indicates a correction factor of ≈15%.

5.6.2.4 Spatial Resolution.

There are two related questions in spatial resolution; one is how narrow a spatial variation can be detected, and the other is how to deconvolute the magnitude (concentration) of a very narrow distribution from the total detected signal.

Numerous segregation studies in ceramics have shown that concentration changes at the grain boundary can be detected with an effective resolution of 50-100 angstroms. However, existing models predict a greater degree of beam broadening than this. Broadening has been modeled by a single scattering model (109), by Monte Carlo simulation techniques (See Goldstein, 108, and Kyser, 111 for reviews), and most recently by electron wavepacket diffraction theory (103).

The single scattering model, which is the most easily applied of the three, assumes a point source of electrons and that the electrons are elastically scattered at the center of the foil, as shown in Fig. 5.5. The exit diameter of a cone containing 90% of the scattered electrons is:

$$b(cm) = 625(z\ p^{1/2}\ t^{3/2})/(E_0 A) \qquad (5.5)$$

where z is the atomic number, A the atomic weight, E_0 the incident electron energy, p the specimen density and t the foil thickness. Figure 5.6 shows the broadening calculated from Eq. 5.5 for $MgAl_2O_4$.

Monte Carlo simulation techniques which calculate electron trajectories in a stepwise fashion are more precise since additional factors such as electron backscattering and multiple scattering are included; however, they are tedious to apply for routine microanalysis. Comparisons between the single scattering model and Monte Carlo simulations indicates that the former predicts less broadening in thin foils and greater broadening in thicker foils (108).

The electron wavepacket diffraction model of Marks (103) considers the probe spreading due to localized diffraction, and is promising in both its rigor and its ability to explain certain experimental results the others cannot. Results show that broadening has a lesser dependence on foil thickness than the $t^{3/2}$ relationship of the single scattering model, and is especially small close to a zone axis orientation. Near a strongly diffracting condition, on the other hand, the

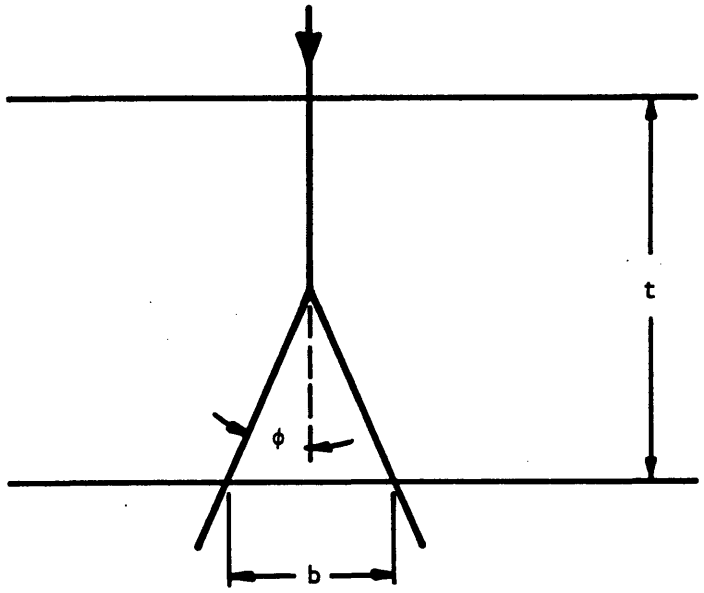

Figure 5.5 Single scattering model of beam broadening after Goldstein et al. (ref. 109).

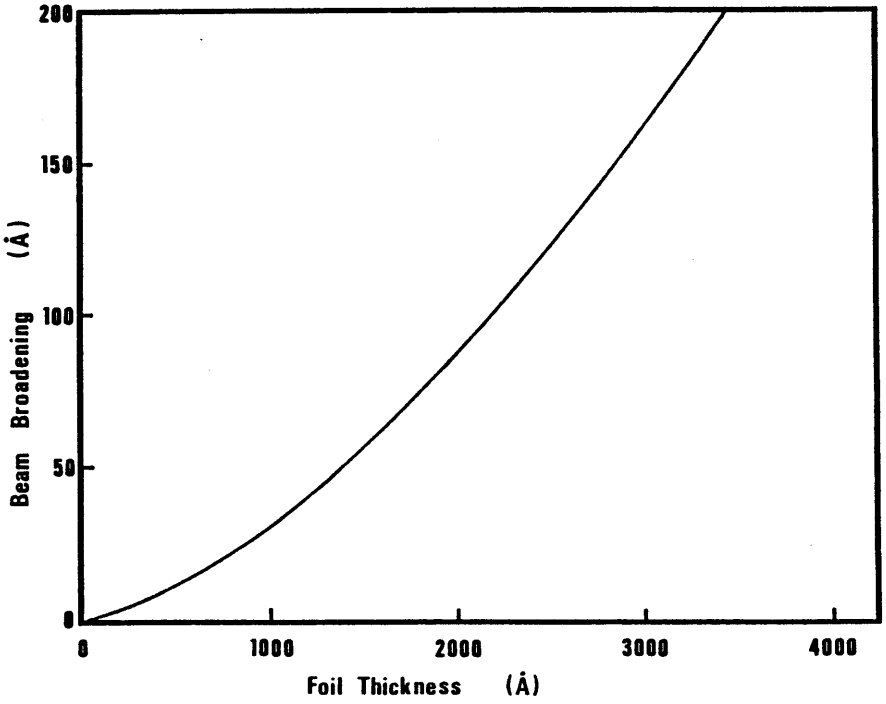

Figure 5.6 Beam broadening calculated from the single scattering model for $MgAl_2O_4$.

spreading is greater and is axially asymmetric, which can account for the experimental observation of anomalously skewed segregant distributions when the beam is strongly diffracted (102). Collision interactions with the boundary plane may also be important.

Bender et al. (112) have modeled the beam-analyzed volume as a column the diameter of the beam plus a truncated cone of width calculated from the single scattering model. From the relative volume of an enclosed grain boundary plane of width δ compared to the total volume, they calculate the grain boundary concentration from the observed signal. This model fails to account for the spatially non-uniform beam intensity (usually taken to be a Gaussian distribution across the beam diameter), and will underestimate the grain boundary concentration since, in fact, more X-rays are generated from from the center of the cone where the beam intensity is high than the edges. Hall et al. (113) have taken this intensity distribution into account in applying the single scattering model. For Fe segregation in MgO, they observe that for thin foils the peak signal at the grain boundary decreases with increasing foil thickness as expected, but that for thicknesses between 2000 and 4500 angstroms the peak signal at the boundary remains approximately constant. Comparison with calculated profiles indicates that the single scattering model fails; it overestimates the amount of beam broadening in this range of foil thicknesses, much as the work by Marks

(103) suggests.

In the present work the foil thicknesses we have used (1500-3500 angstroms) are in the same approximate range as in Hall's work (113). The thicknesses were estimated from the Al X-ray count rate relative to the electron beam current (measured at the objective aperture), using as a calibration standard convergent beam diffraction thickness measurements in a spinel sample which showed that the X-ray count per unit beam current increases linearly with sample thickness (Appendix 2).

Overall our observations were similar to those of Hall et al. (113) in that grain boundary X-ray intensity ratios in a single sample did not vary much with thickness, but if we applied Bender et al.'s model (112) and the beam broadening predicted by the single-scattering model, the calculated grain boundary concentrations are unrealistic. In order to interpret the results from a large number of boundaries for which individual calculation of beam broadening according to the more accurate models is unfeasible, we have resorted to a greatly simplified model after Doig and Hewitt (114) in which the analyzed volume is assumed to be a cylinder of diameter d centered on the boundary (Figure 5.7). For bulk solute concentrations that are small compared to the boundary concentrations, the grain boundary concentration is related

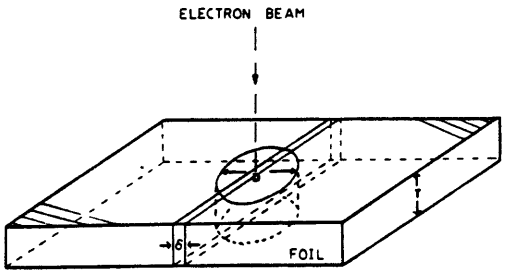

Figure 5.7 Beam-analyzed volume modeled as a cylindrical X-ray source containing the grain boundary (ref. 114).

to the observed peak concentration as:

$$C_{gb} = C_{observed} \cdot (V_{cyl}/V_{gb}) \qquad (5.6)$$

$$= C_{observed} \cdot (\pi d/4\delta)$$

Thus the enhancement factor $(\pi d/4\delta)$ is independent of thickness, which is an oversimplification, but is in better agreement with experimental results than the single scattering model. This enhancement factor is equal to 15.71 for the value of δ= 5 angstroms and d = 100 angstroms that we have used.

For segregation in a boundary plane of ≈5 angstroms width the STEM probe is clearly wide enough to enclose the entire distribution. Even in the case of a space charge distribution that extends perhaps ≈30 angstroms to either side of the boundary (18), this approximation seems to be adequate since the Fe segregation observed by Hall et al. (113) in MgO is of this character and does not show systematic variation of peak concentrations with thickness. However, in some of the present results in highly alumina rich spinel we found distributions that were even wider, for which Eq. 5.6 will underestimate the amount segregated.

VI. RESULTS

6.1. Grain Growth

6.1.1 Nearly Stoichiometric Spinel

The slightly alumina rich (n=1.013) sample hot-pressed by Rhodes showed uniform grain growth in the grain size range 0.6-7.5 μm and temperature range 1250°-1650°C. Representative micrographs are shown in Figure 6.1; no discontinuous grain growth was observed. The grain growth kinetics were approximately parabolic at two temperatures (1450° and 1600°C) where multiple anneal times were used. In Figure 6.2 is plotted 1450°C data as grain size squared against time and grain size cubed against time, illustrating a linear fit for parabolic grain growth kinetics. In Figure 6.3 are shown similar data for 1600°C. Anneal times ranged from 4 to 40 hours for samples of this composition. Grain boundary mobilities at other temperatures where only one anneal was conducted were thus derived assuming parabolic growth.

In Figure 6.4 we have plotted mobility versus reciprocal temperature for samples examined here along with data from the literature for nearly stoichiometric spinel. Besides data from the n=1.013 sample which spans the widest temperature range, a single data point obtained on a sample hot pressed from nitrate powder prepared to be as close to stoichiometry as possible (n=1.00) is shown, and also two data points measured from Baikowski stoichiometric powder

hot-pressed without encapsulation and therefor purity.

All of the data agrees closely; that from sample is very linear from 1250° to 1650°C and regresssion analysis yields a mobility (in uni $cm^4/erg.sec$):

ln M = -[6.05(+/- 0.67)] - [4.37(+/- 0.1eV

The activation energy is comparable to the 4.7 (66) measured over the same approximate temper Extrapolating to 1800°C, reasonable agreement factor of 5) is found with the stoichiometric Uematsu et al. (6) in Fig. 3.5 and that derive et al.'s published micrographs (67).

6.1.2 Magnesia Excess Spinel

Most of our data here are from a hot-pre encapsulated n=0.957 sample. The grain grow uniform with a narrow size distribution (Fig followed parabolic kinetics better than a t^1 (Fig. 6.6). However, the starting grain s larger (≈7μm) and grain growth was much mor the stoichiometric samples; final grain siz range 10-40 μm for anneal times of one hour corresponding mobilities are plotted again temperature in Figure 6.7. From 1450°-17C 10^3 greater than in the nearly-stoichiomet

linear regression yields:

$$\ln M = -[8.96(+/- 1.37)] - [3.02(+/- 0.78eV)]/kT \quad (6.2)$$

No second phase magnesia was observed in this n=0.957 composition except for occasional precipitates in the 1450°C anneal that were few enough not to cause significant particle pinning of grain boundaries. In contrast, an n=0.883 sample had substantial amounts of second phase magnesia in the as-hot pressed material that did not dissolve in the course of annealing, even at 1700°C, and precluded an accurate mobility determination. The spinel grains in this sample were large though, (>10 μm for short time ≈15 min. at 1700°C) and suggested boundary mobilities much higher than in the stoichiometric compositions. Since the spinel phase composition in this two phase sample is somewhere between that of the MgO-$MgAl_2O_4$ phase boundary at 1450°C (the hot pressing temperature) and 1700°C, it appears that the mobility does not drop off with increasing magnesia in solid solution as Uematsu et al. (6) suggested.

We examined also a sample of composition n=0.909 prepared and annealed by R.D. Bagley (Corning Glass Works) which supports this view. This sample had been annealed in H_2 at 1805°C for 20 min., then thermally etched at 1525°C for 7 min.. A fine dispersion of magnesia precipitates (Fig. 6.8a) throughout the sample hindered grain growth in the polycrystalline portion of grain size ≈8 μm (Fig. 6.8b), but in many places discontinuous grain growth had occurred,

leading to large grains of several hundred microns dimension. In Figure 6.9 are shown large grains of several hundred micron dimensions in the bulk and growning in from the sample edge, leaving behind the migrating boundary a dispersion of magnesia precipitates. Thus these are boundaries that have broken away from second phase particles; the composition of the magnesia saturated spinel phase is that at the phase boundary.

The mobility calculated for a driving force based on the 8 μm matrix grain size lies close to the extension of our data for the n=0.957 sample in Fig. 6.7. These results indicate that with even greater excess magnesia in solid solution, the boundary mobility remains 2-3 orders of magnitude higher than in stoichiometric spinel up to the phase boundary composition.

The very high mobility for slightly magnesia excess spinel reported by Uematsu et al. (6), Figure 2.5, is still an order of magnitude higher than what we have calculated. Nowhere in the course of this work did we measure a mobility quite this high; this may be an intrinsic grain boundary mobility if the recrystallizing grains have broken away from the solute cloud. It is possible that the fine magnesia precipitates in the Bagley recrystallized sample do cause some boundary pinning and lower the apparent mobility somewhat, and that in the absence of these precipitates the mobility would be higher still.

6.1.3 Alumina Excess Spinel

The grain sizes and growth rates of alumina-rich (n=1.56) samples were very similar in magnitude to that of the stoichiometric ones. However, no clear distinction between parabolic growth and $t^{1/3}$ kinetics was possible on the basis of the time dependent data at 1600°C, Figure 6.10. Nonetheless, because of the absence of mechanisms that could give rise to a $t^{1/3}$ dependence, such as pore drag or strong impurity segregation, mobilities were calculated on the basis of parabolic kinetics, and are plotted in Figure 6.11. The mobilities in the temperature range 1500°-1700°C are less than for stoichiometric samples, and linear regression yields a mobility:

$$\ln M = -[17.93(+/- 1.881)] - [2.57(+/- 0.30eV]/kT \quad (6.3)$$

A less alumina-rich sample (n=1.28) was also prepared and annealed, but did not show uniform grain growth. This was attributed to non-uniform composition on a microscale, readily identified from the broadened, diffuse Debye-Scherrer lines from this particular powder batch. However, from the non-uniform grain growth it was still possible to estimate a range of mobility, included in Figure 6.11, which is slightly higher than in either the stoichiometric or more alumina-rich samples.

6.1.4 Summary of Grain Growth Data

The present data are shown collectively in Figure 6.12, plotted as mobility against reciprocal temperature, along with the available literature data. In Figure 6.13 we have plotted the grain boundary mobility results as a function of sample composition. At fixed temperature, the mobility with increasing alumina content from stoichiometry to alumina-rich compositions appears to initially increase, then decrease. Unlike what Uematsu et al. (6) have indicated (Fig. 3.4), the mobility does not continue to increase up to the $MgAl_2O_4$ phase boundary. With increasing magnesia excess from stoichiometry, however, the mobility quickly rises by 10^2 to 10^3 and appears to remain approximately at this level up until the phase boundary.

6.2 Segregation Results

6.2.1 Impurity Segregation

The principle impurities found segregated at grain boundaries in nitrate derived samples were Si and Ca, whereas alum-derived samples also showed some S segregation. Figure 6.14 compares segregation found in a Baikowski alum-derived spinel powder hot-pressed at 1800°C without encapsulation, with that observed in an encapsulated nitrate-derived sample annealed at 1600°C. This illustrates the improvement in sample purity gained by the encapsulation procedure. The Baikowski powder is probably not as impure as this data

suggests; some of the impurities may well be from the graphite die material. The magnesia rich sample prepared by Bagley also from sulfates did not have segregation in such high quantities as the Baikowski sample shown in Fig. 6.14a; there was only a slight S segregation along with Si and Ca segregation in levels comparable to that found in the nitrate-derived samples.

Figure 6.15 shows the Si and Ca segregation that has been observed in these grain growth samples, plotted against sample stoichiometry and quantified using the forsterite and calcium aluminate standards with the model described in section 5.6.2.4. The data are plotted as fractional monolayers of impurity, where a monolayer refers to the surface cation site density in spinel. Error bars have not been included for the sake of clarity. There are, however, three sources of error in these data. These are: the error in counting statistics, which is lower the higher the impurity signal (greater number of X-ray counts), the error in K_{ab} values used to quantify the data (Table 5.2), and an error introduced by the beam broadening model which does not account for small (+/-10%) changes in peak concentration with specimen thickess. The cumulative error in on the order of +/-30% for the higher concentrations.

Data from all temperatures are included in Figure 6.15 since there was no correlation found between the amount of impurity segregation and the annealing temperature. In

particular, we found that each composition contained certain boundaries for which virtually no segregation was found. Even the maximum amounts of segregation observed are quite dilute, never exceeding 15% of a monolayer for Si and 20% for Ca. The larger amount of segregant shown in Fig. 6.14a corresponds to 67% and 56% of a monolayer for Si and Ca respectively.

6.2.2 Aluminum/Magnesium Segregation

In all of the grain boundaries examined, the Al/Mg ratio increased relative to the bulk. This was true regardless of sample stoichiometry. Figure 6.16 shows Al/Mg profiles across grain boundaries in magnesia rich, nearly stoichiometric, and alumina rich samples. The background Al/Mg ratio indicates the stoichiometry of the sample; the sample of n=0.88 is magnesia-saturated at the anneal temperature (1600°C) yet shows substantial increase in Al/Mg ratio across the boundary. The nearly stoichiometric sample shows approximately the same amount of segregation, while the alumina rich sample (n=1.28) shows substantially more segregation.

Often the Al/Mg profiles exhibited what seem to be slight depletion regions immediately adjacent to the increase at the boundary. An especially marked version of this is shown in Fig. 6.17 for an n=3 Baikowski powder sample annealed at 1800°C and cooled slowly at a rate of <100°/sec.

(Note the high bulk Al/Mg ratio and the 10X change in scale for this sample.) We attribute the depleted zones to segregation upon cooling; the width represents approximately the diffusion length for the segregating species. The segregation profile from an n=0.957 sample that was quenched into water ($\approx 10^4$ °C/sec) from 1600°C is shown in Figure 6.18 Within statistical scatter, the results are the same as for samples that were gas-quenched, indicating that the rate of cooling was adequate within the resolution of this analysis.

The amount of Al segregation varied with sample stoichiometry as shown in Figure 6.19. Data from the n=0.88 sample at 1600° C is plotted at the estimated phase boundary composition since this sample was two-phase. There is clearly less Al segregation at boundaries in magnesia rich spinel compared to alumina rich samples as a whole, and in the alumina rich samples the excess increases with nonstoichiometry. Here the concentration of excess Al (which includes depletion of Mg) was calculated using the grain interiors as a standard and with the same cylindrical volume model of beam broadening (Eq. 5.6) as used for Si and Ca segregation. For most of the samples we examined, the observed segregation profile of Al is narrow enough (decreasing to background levels within 100 angstroms of the boundary) that this model is applicable. Examples of narrow profiles are the n=0.883 and 1.013 profiles in Fig. 6.16, and others for the n=0.957 sample are

illustrated in Fig. 6.20. However, for highly alumina rich samples (n=1.28 and 1.56) slightly wider distributions were observed (Fig.6.16, n=1.28, and Fig.6.21, n=1.56) for which Eq. 5.6 underestimates the amount segregated, by perhaps a factor of 1.5 or 2. Thus the increase in excess Al with stoichiometry on the alumina excess side is in reality even greater than shown in Fig. 6.19.

There is considerable scatter evident in these data, which upon considering the sources of error appears to be real boundary to boundary variations. The X-ray counting statistics error is small for Al/Mg because of the large numbers of counts generated (typically 6000 to 20000); there is ≈5% relative error in the K_{AlMg} calibration, and foil thickness variations will vary the peak concentrations by +/- several percent in the experimental thickness range of 1500-3500 angstroms (113). The cumulative error is at most ≈25%, which compared with the spread of data in Fig. 6.19 indicates that there are real variations in concentration between boundaries in the same sample.

Only for the two compositions nearest to stoichiometry does the single phase field cover a wide enough temperature range for us to examine the temperature dependence of segregation. For the n=0.957 and n=1.013 samples, examining a very few boundaries in the temperature range 1250°-1600°C revealed no systematic variations in Al excess within the compositional resolution of the STEM analysis.

A)

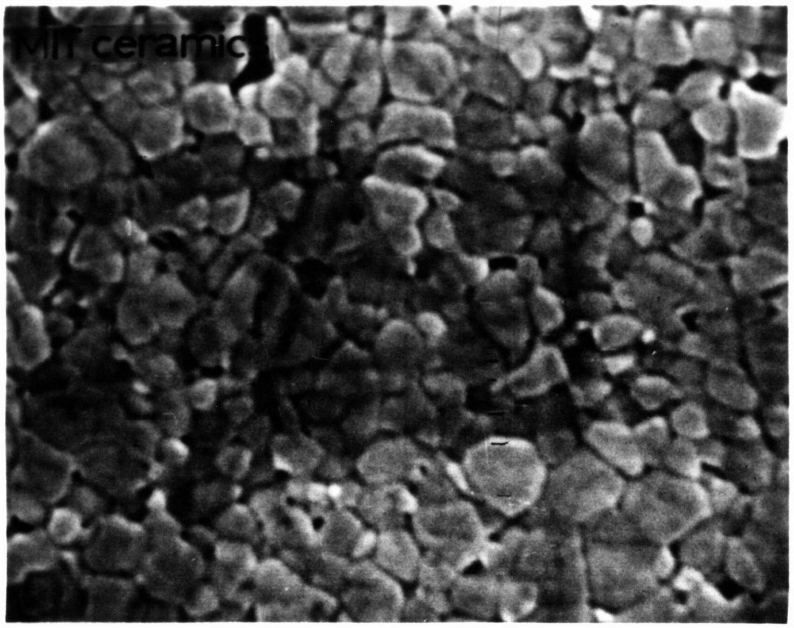

1 μm

B)

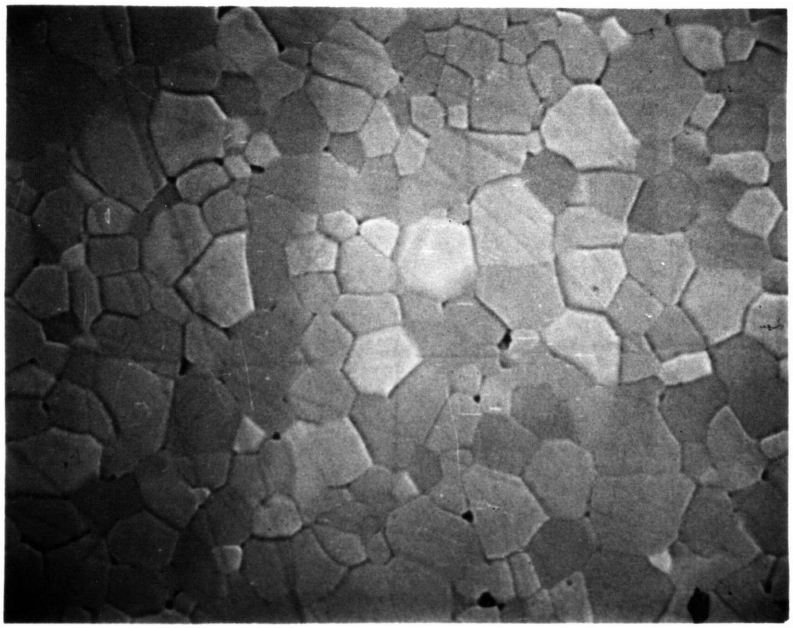

3 μm

Figure 6.1 SEM micrographs of n=1.013 spinel; a) as hot-pressed, and b) after annealing at 1600°C.

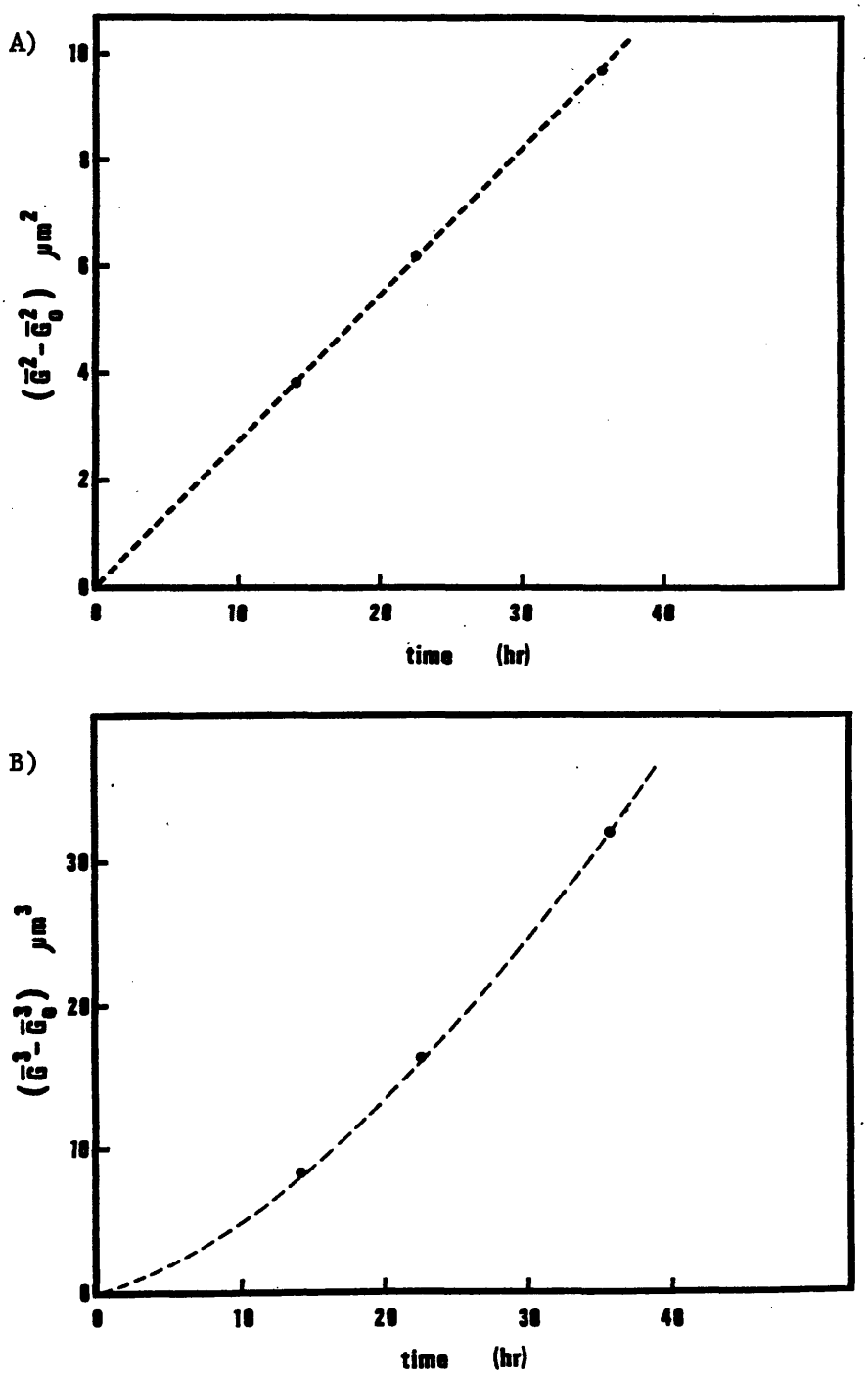

Figure 6.2 Grain growth kinetics for n=1.013 spinel at 1450°C; a) grain size squared vs. time, and b) grain size cubed vs. time.

N=1.013 SPINEL, 1600°C

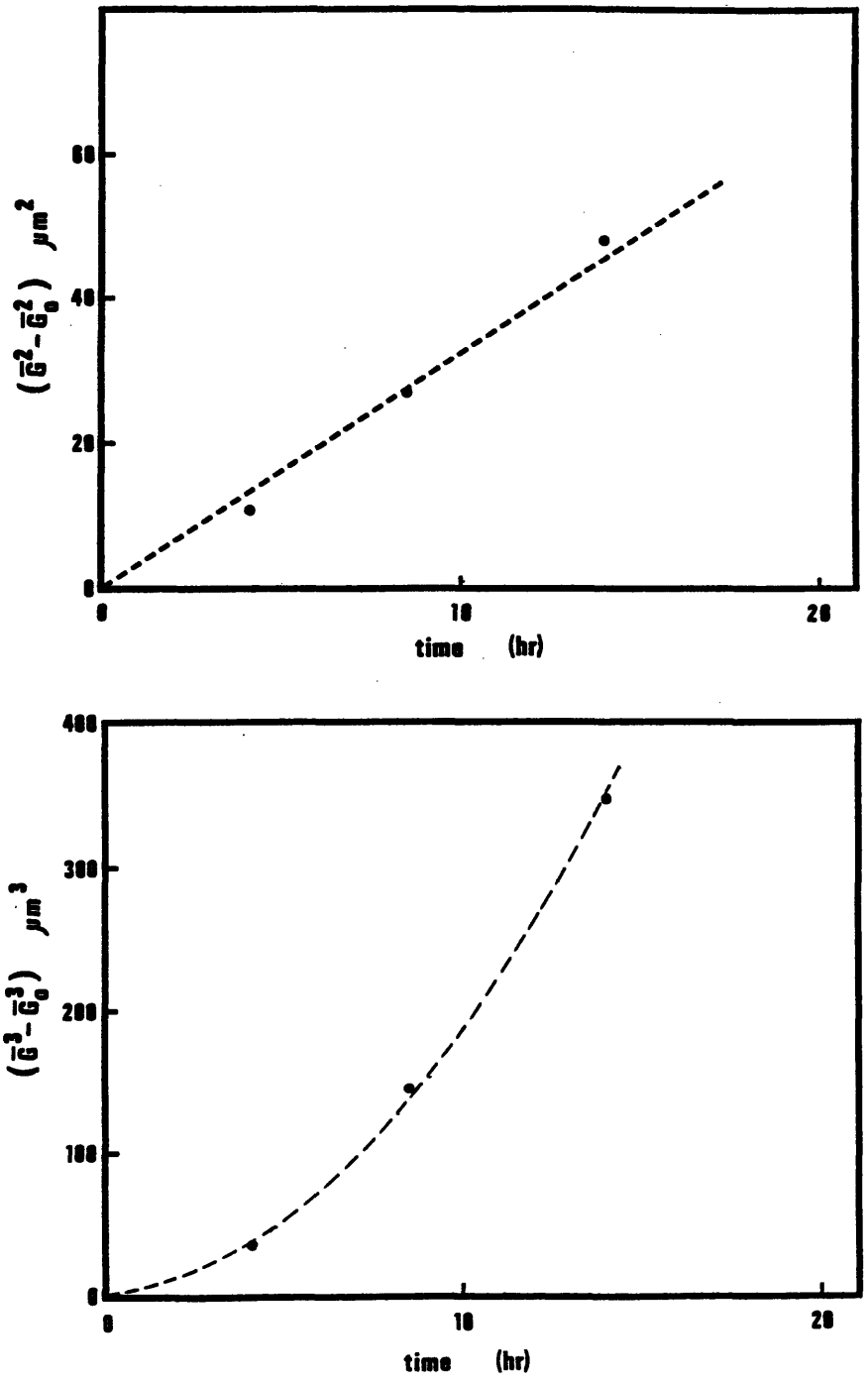

Figure 6.3 Grain growth kinetics for n=1.013 spinel at 1600°C.

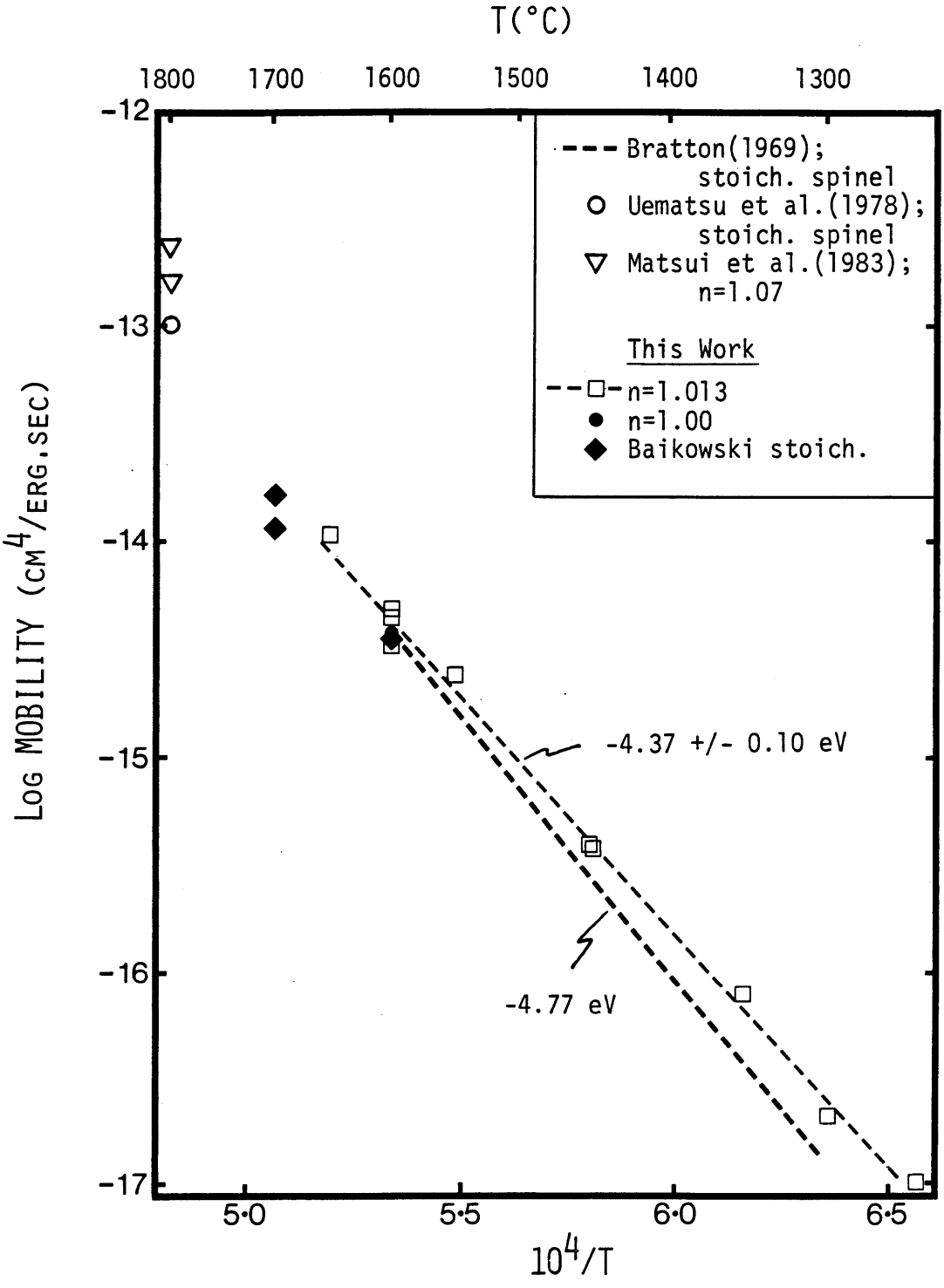

Figure 6.4 Grain boundary mobility vs. reciprocal temperature for nearly stoichiometric spinel compositions.

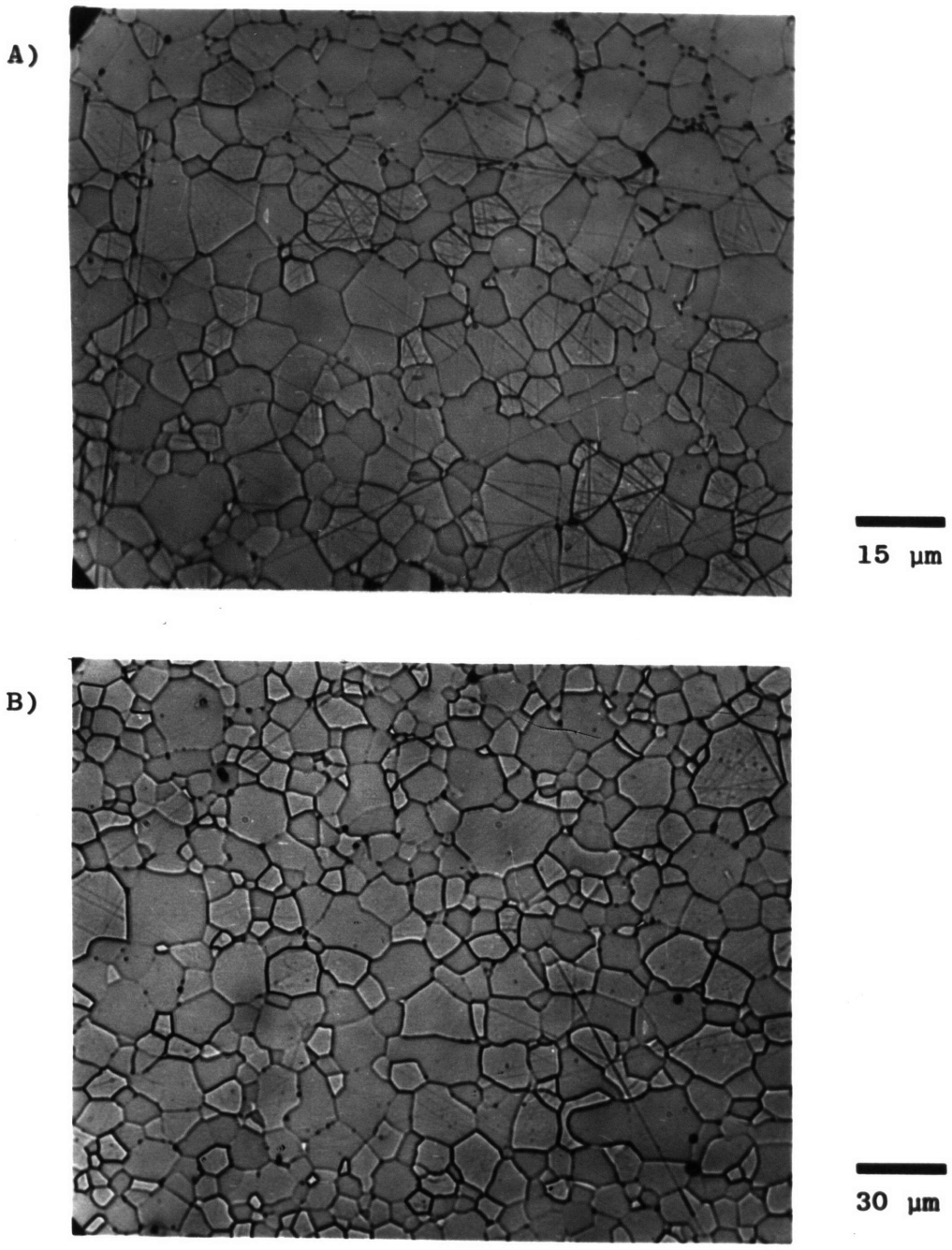

Figure 6.5 Grain microstructure in n=0.957 spinel; a) as hot-pressed, and b) annealed at 1500°C.

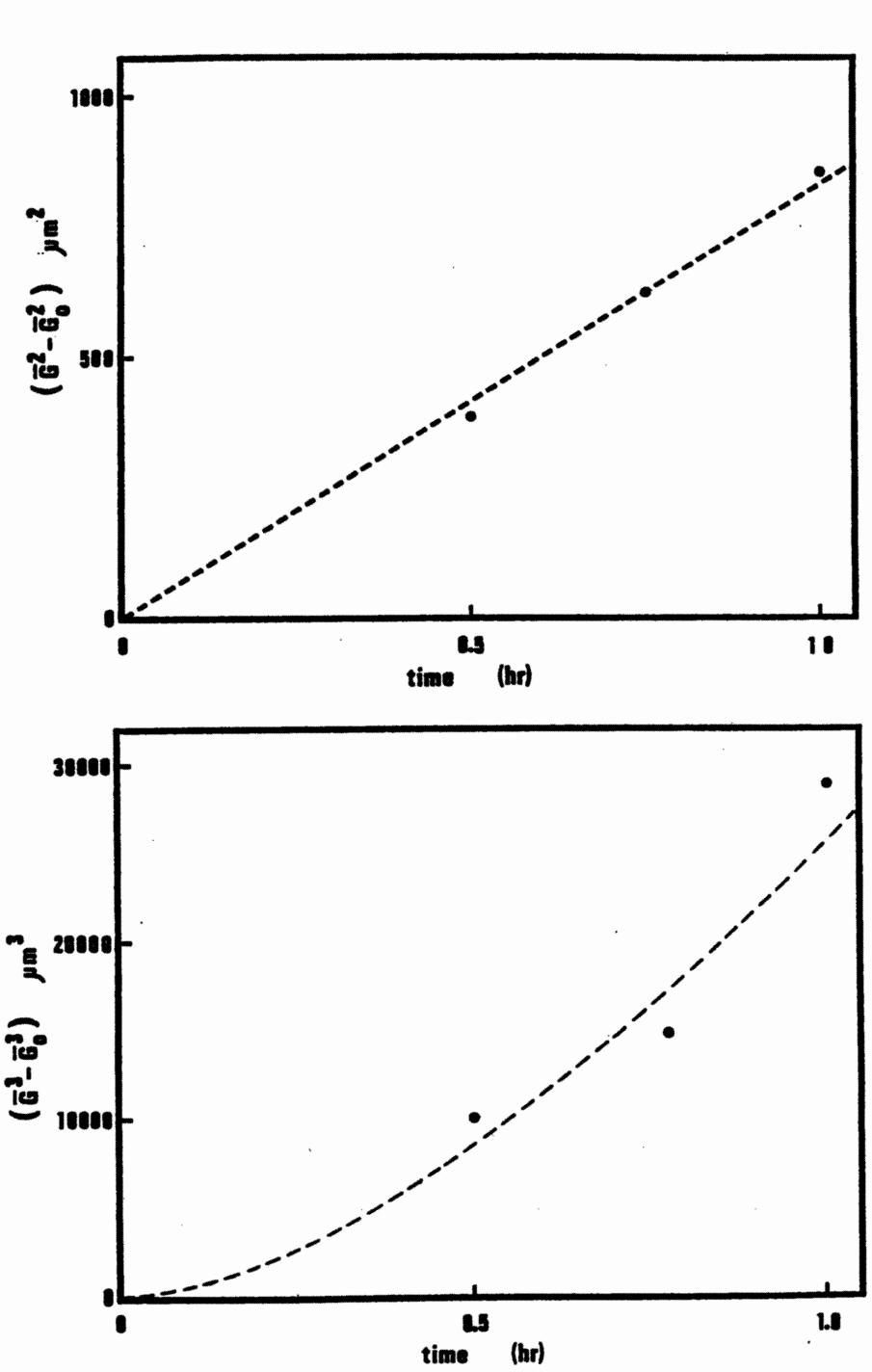

Figure 6.6 Grain growth kinetics for n=0.957 spinel at 1600°C.

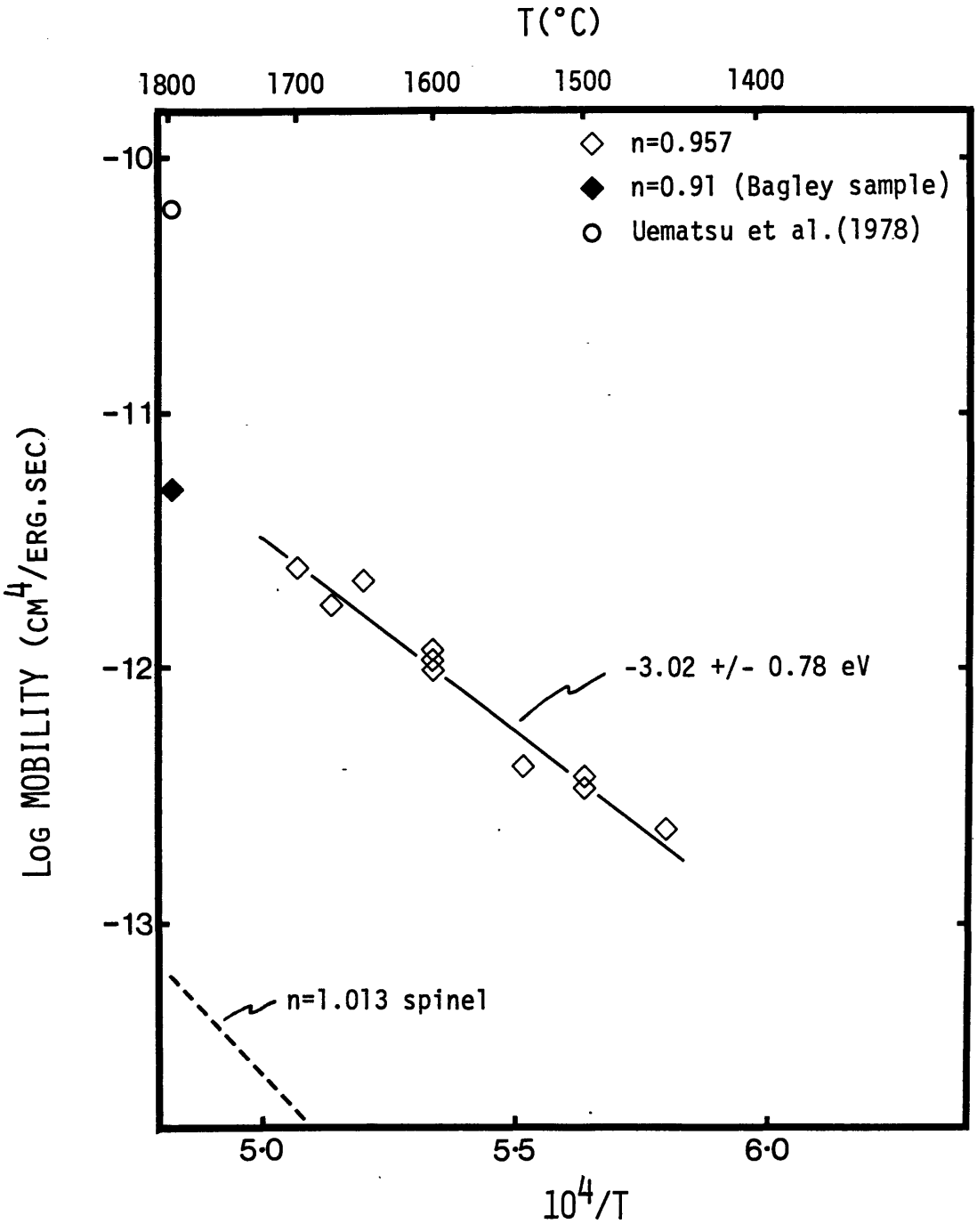

Figure 6.7 Boundary mobility vs. reciprocal temperature for n=0.957 spinel samples.

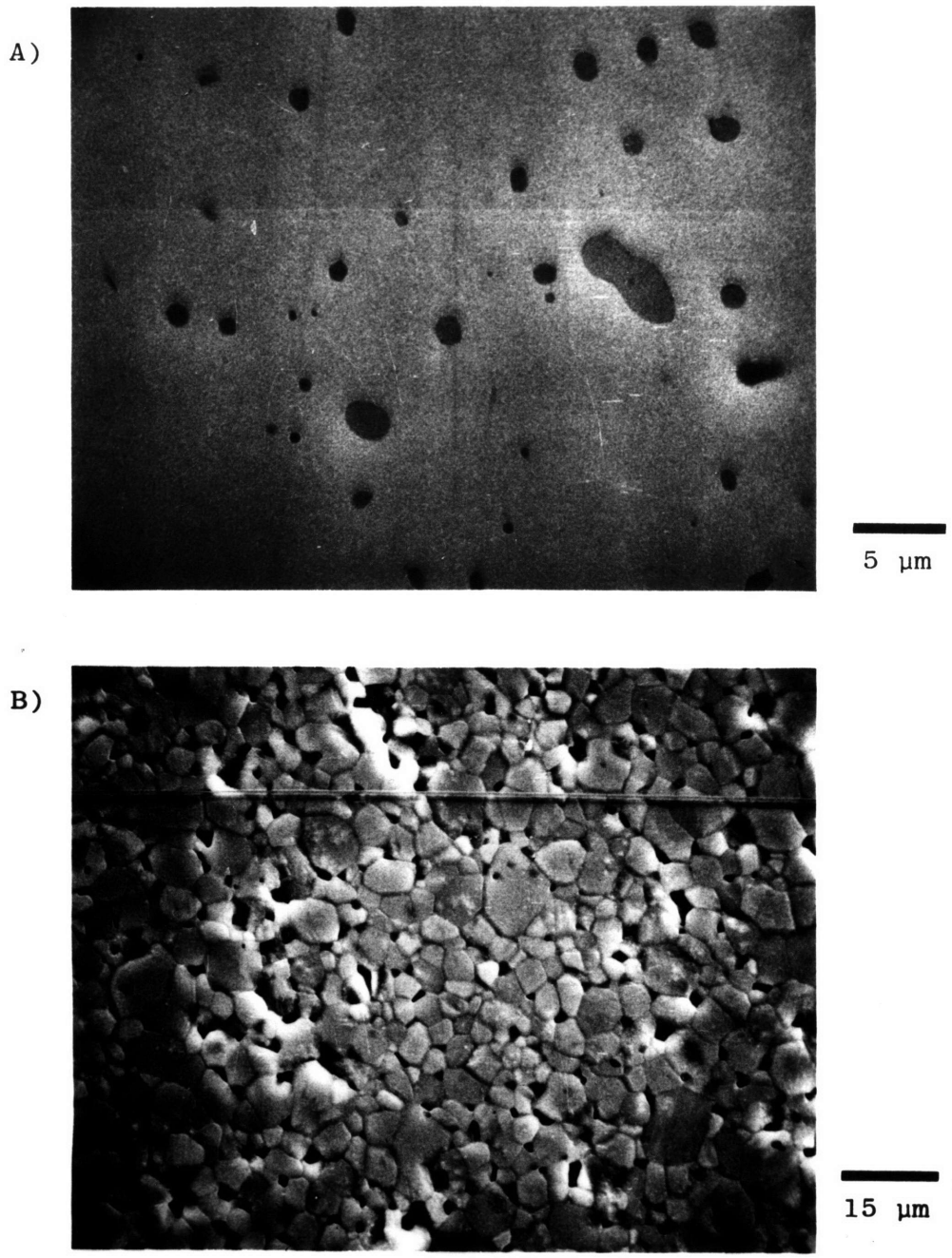

Figure 6.8 n=0.909 spinel sample prepared by R.D. Bagley; a) magnesia precipitates in as-polished section, and b) polycrystalline matrix grain structure.

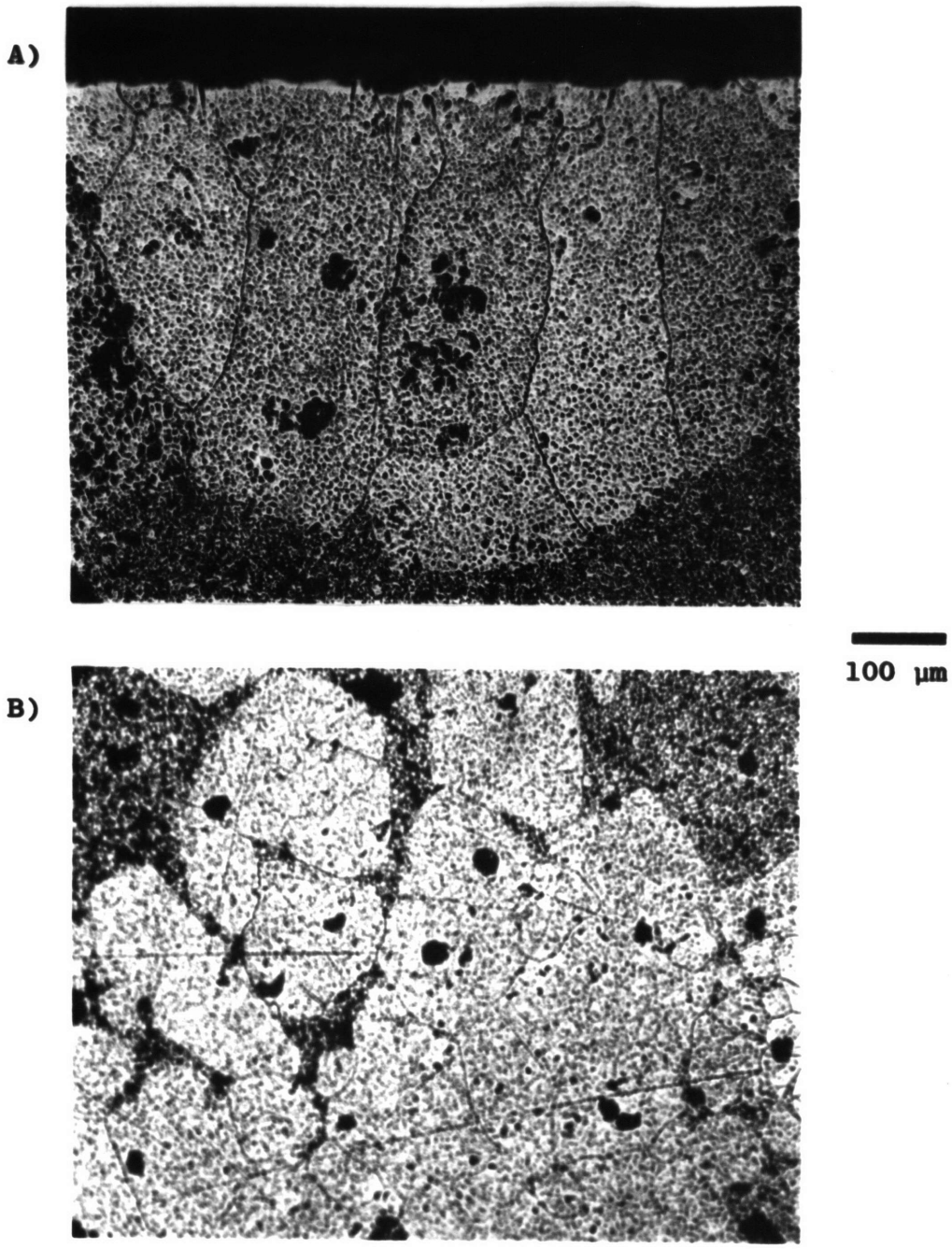

Figure 6.9 Discontinuously growing grains in n=0.909 Bagley sample; a) growing in from sample edge, b) in bulk of sample.

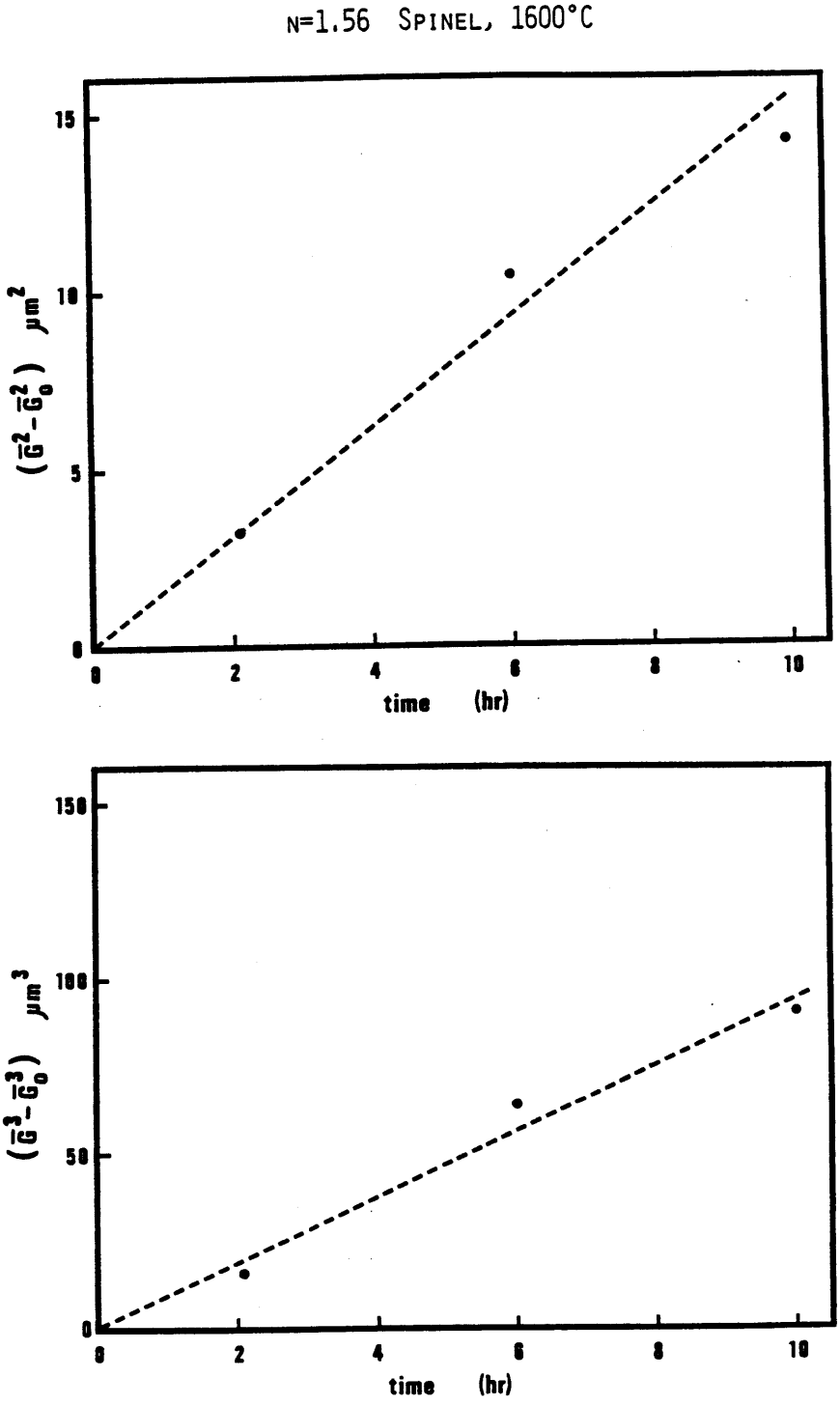

Figure 6.10 Grain growth kinetics in n=1.56 spinel at 1600°C.

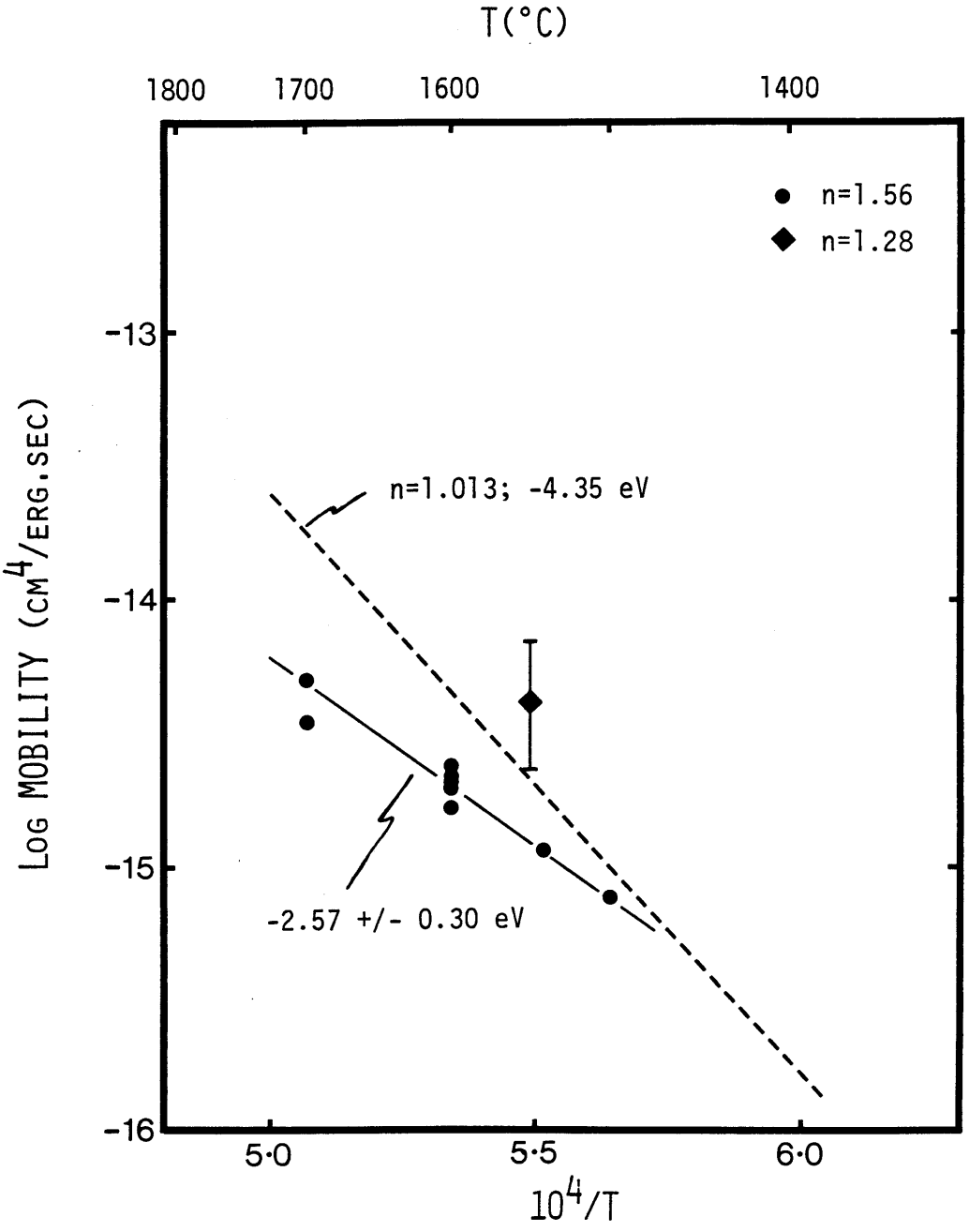

Figure 6.11 Boundary mobility vs. reciprocal temperature for n=1.56 spinel samples.

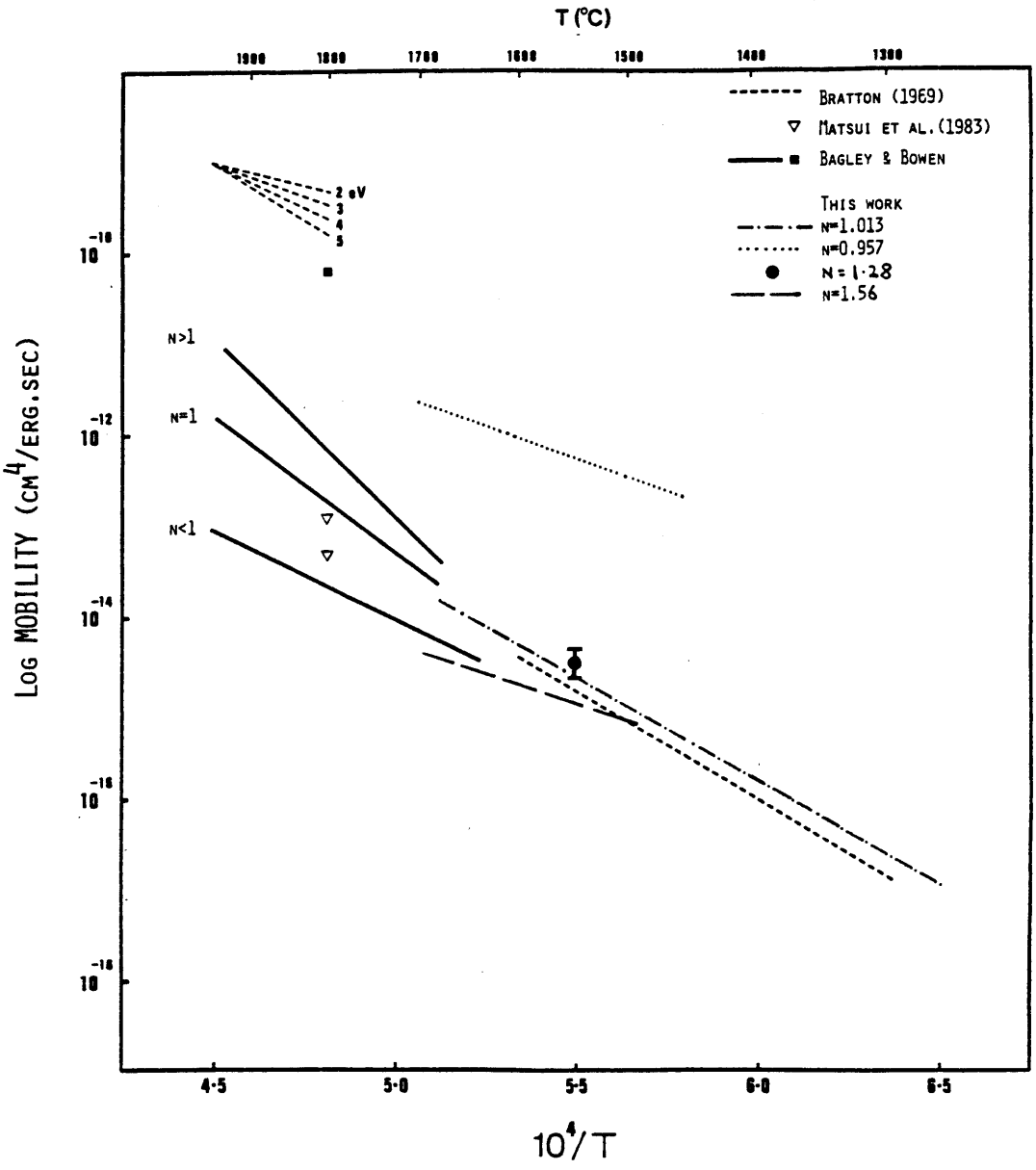

Figure 6.12 Grain boundary mobilities vs. reciprocal temperature from this work and the literature.

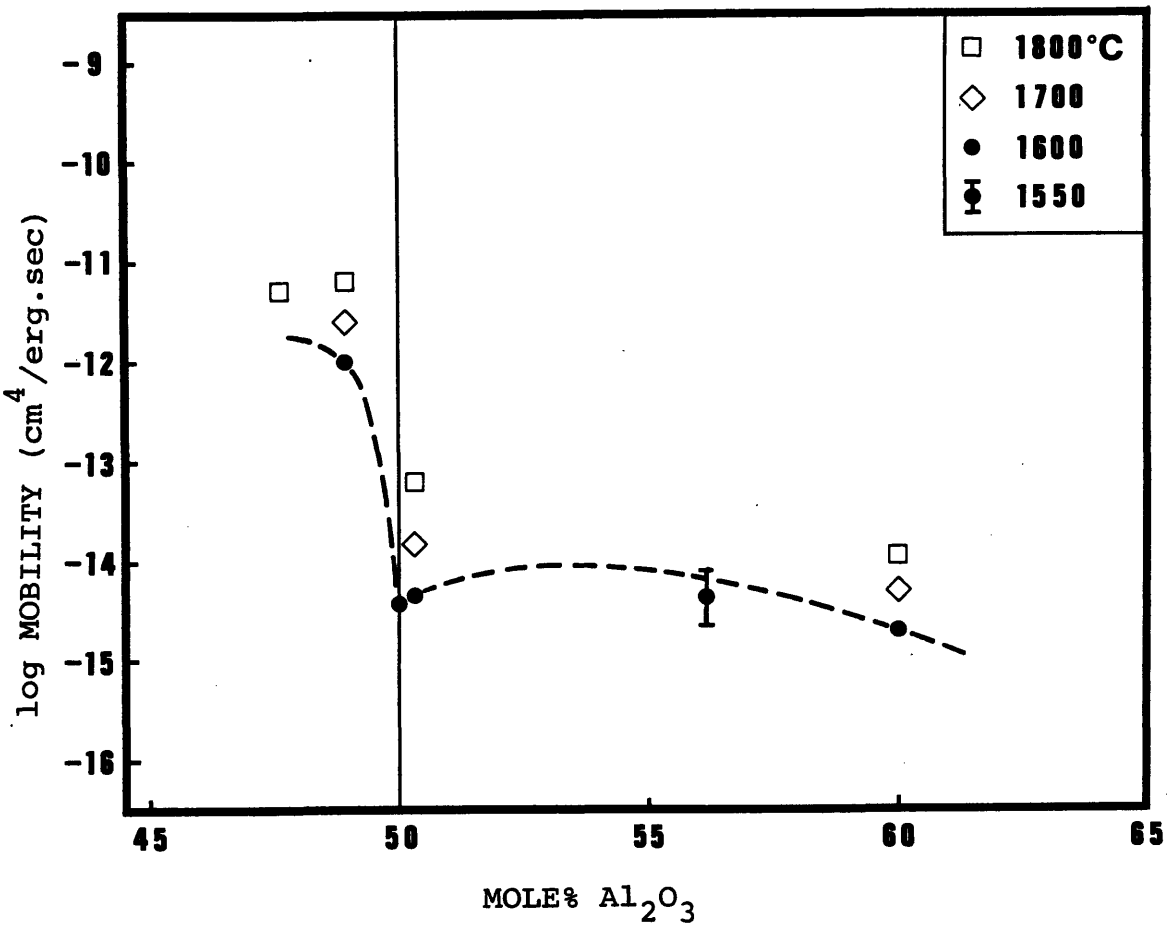

Figure 6.13 Boundary mobility vs. composition, from this work.

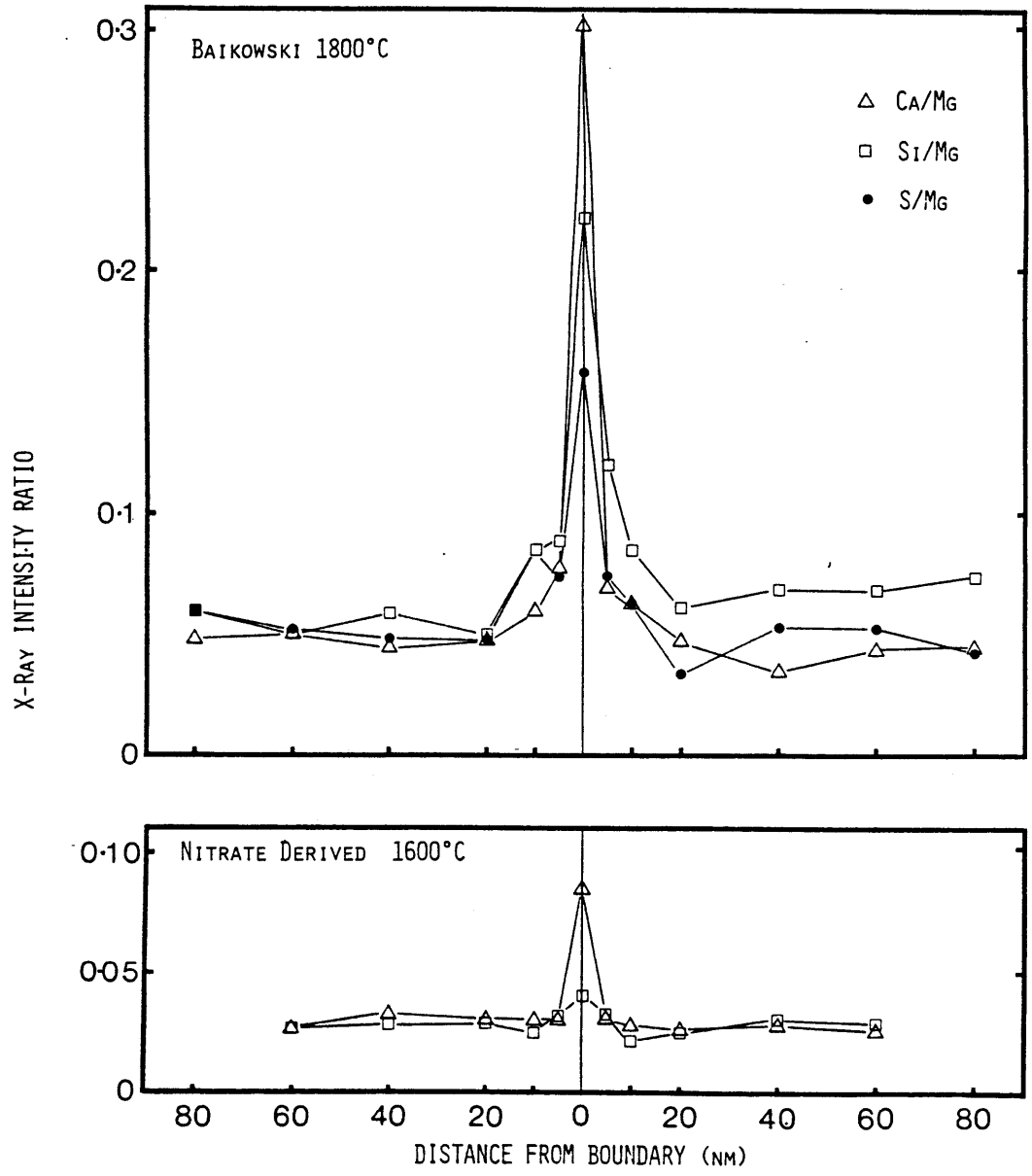

Figure 6.14 Impurity segregation in: a) Baikowski spinel hot-pressed without encapsulation, and b) nitrate derived, encapsulated hot-pressed spinel.

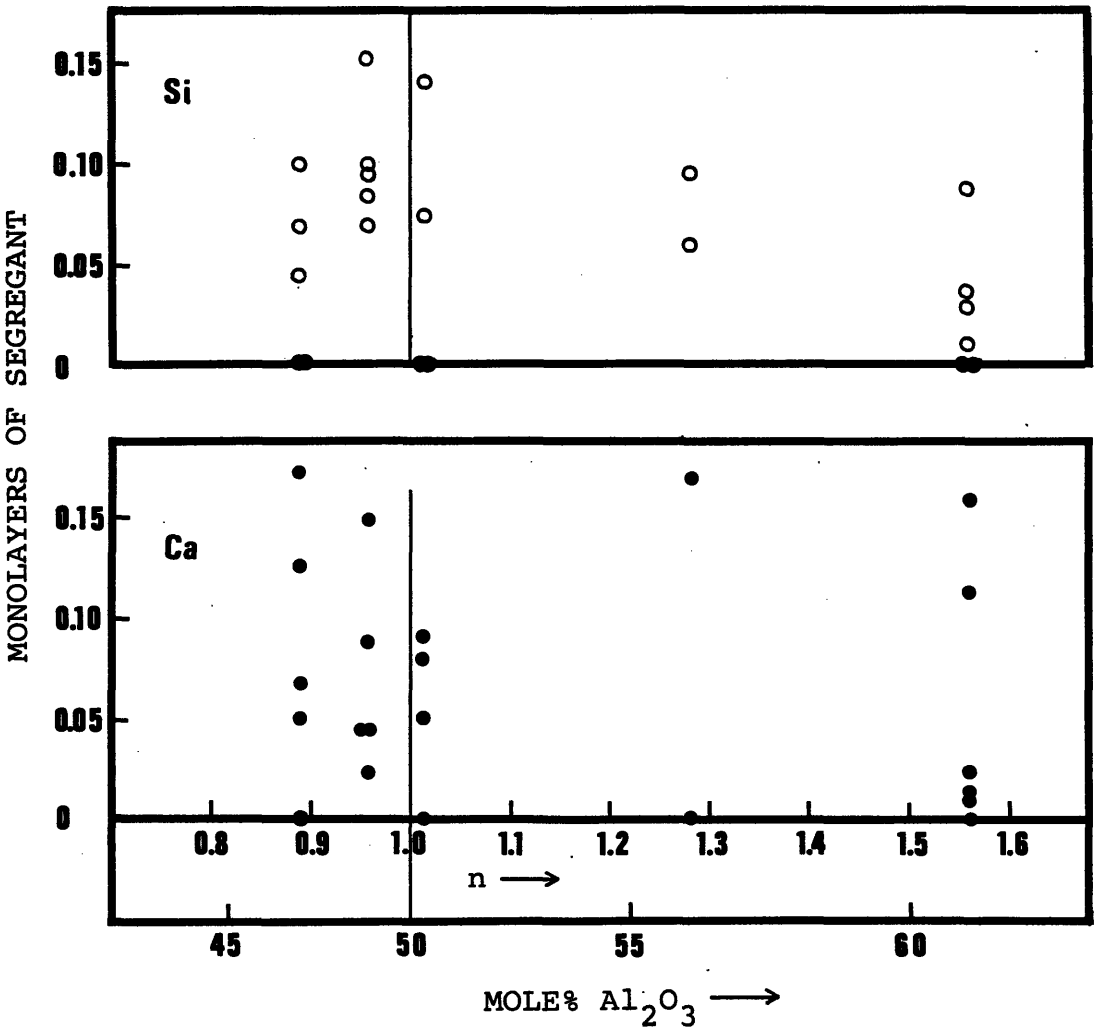

Figure 6.15 Quantified Si and Ca segregation in spinel vs. sample stoichiometry.

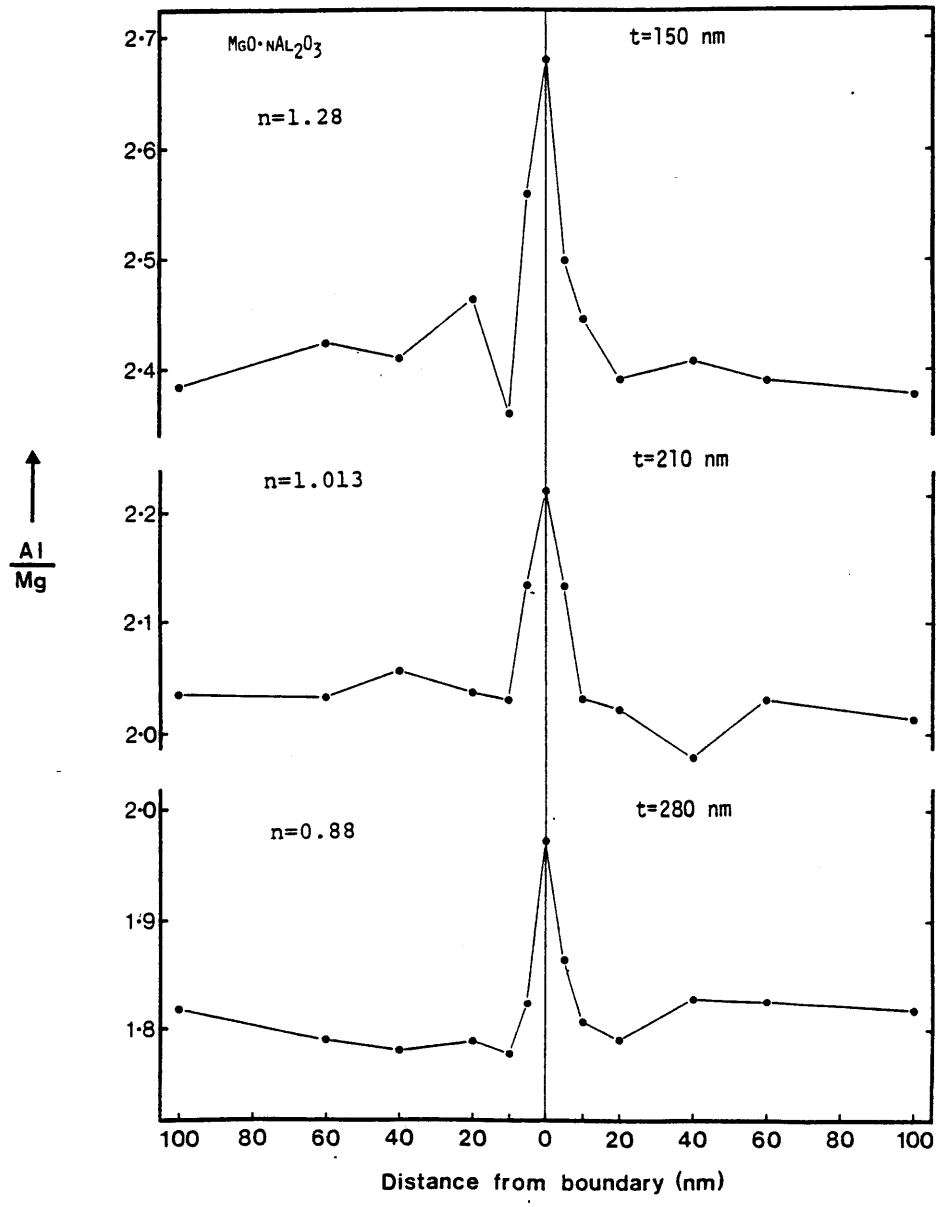

Figure 6.16 Al/Mg profiles across boundaries in magnesia rich, nearly stoichiometric and alumina rich spinel.

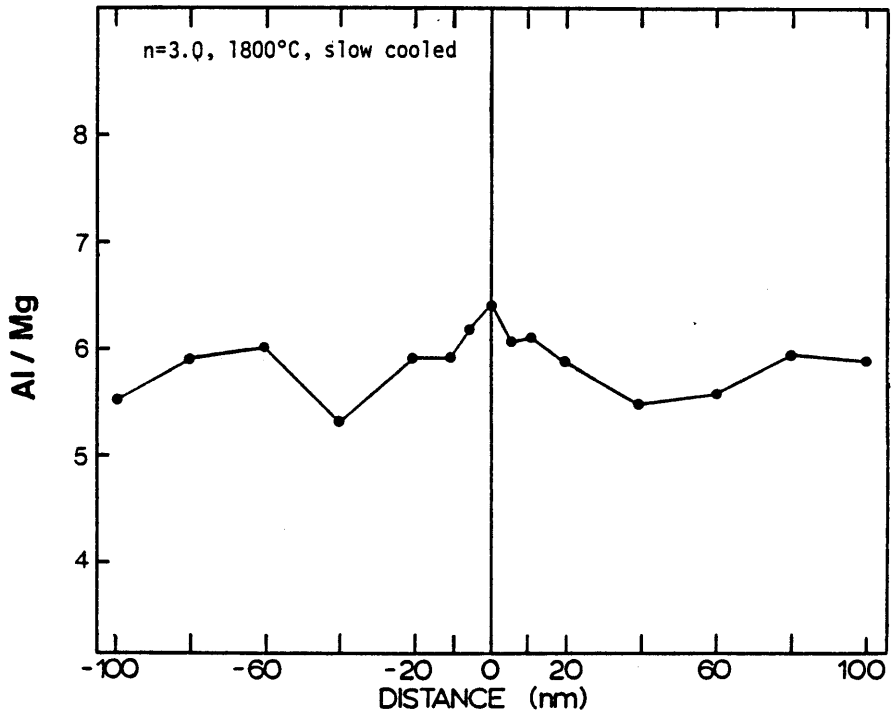

Figure 6.17 Al/Mg boundary profile in n=3 spinel slowly cooled from 1800°C.

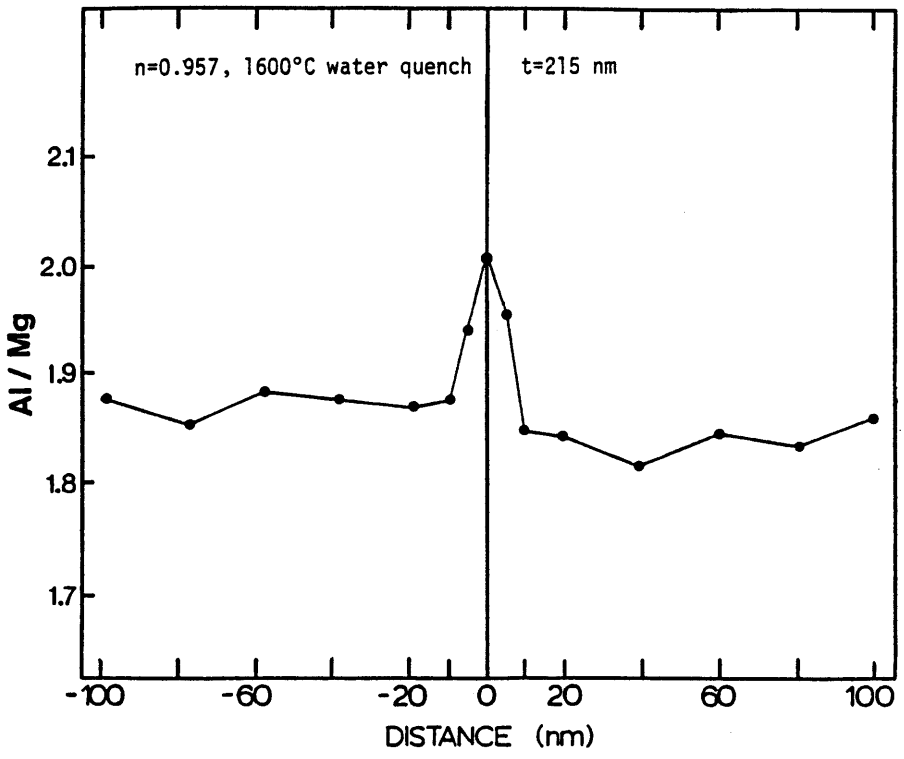

Figure 6.18 Al/Mg boundary profile in n=0.957 spinel, water quenched from 1600°C.

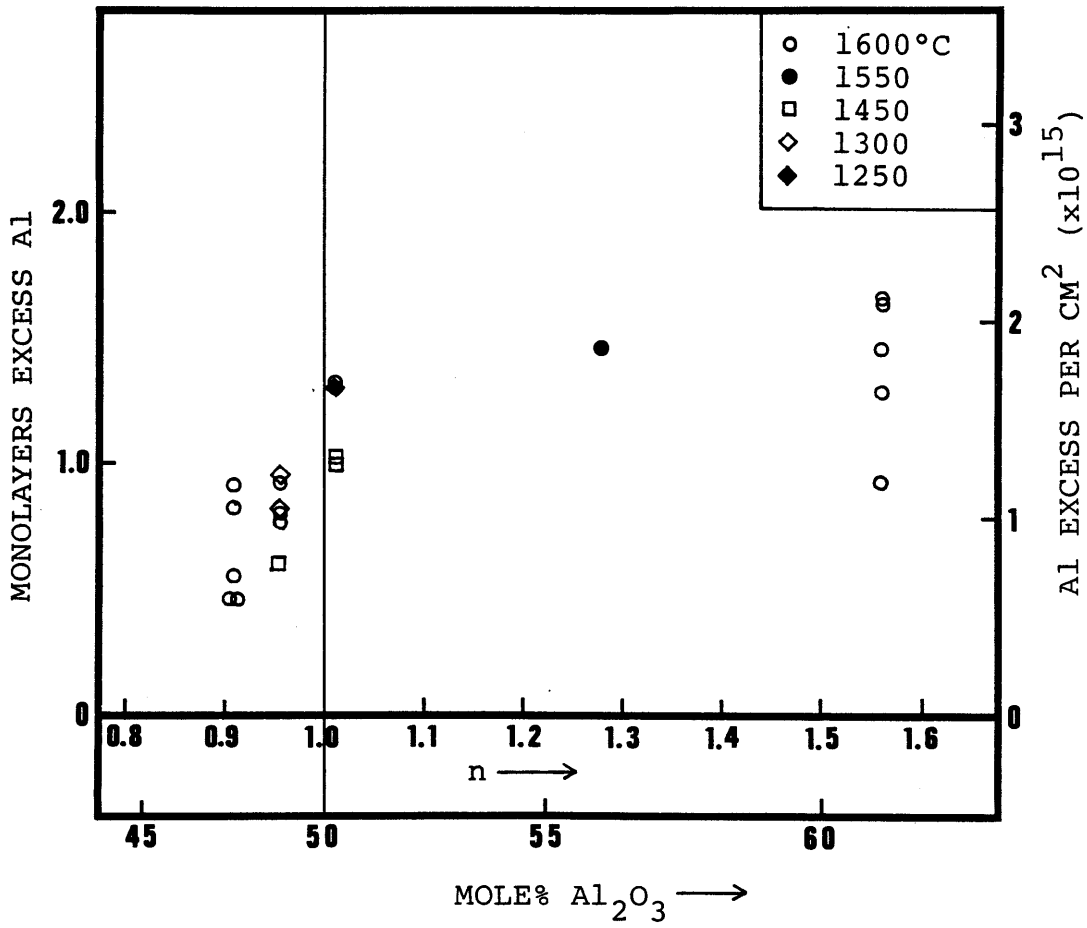

Figure 6.19 Al excess at grain boundary vs. sample stoichiometry.

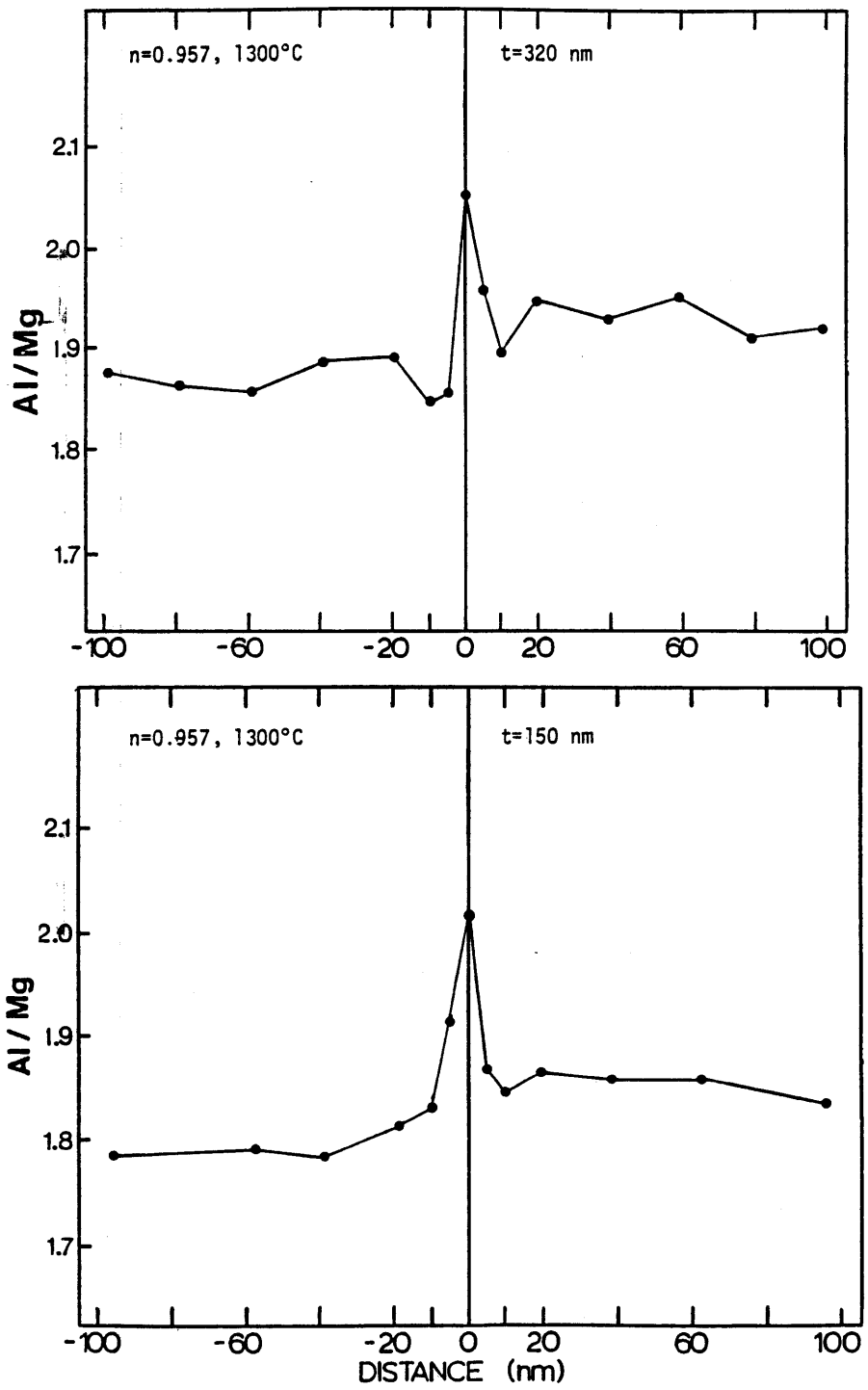

Figure 6.20 Al/Mg boundary profiles in n=0.957 spinel, 1300°C.

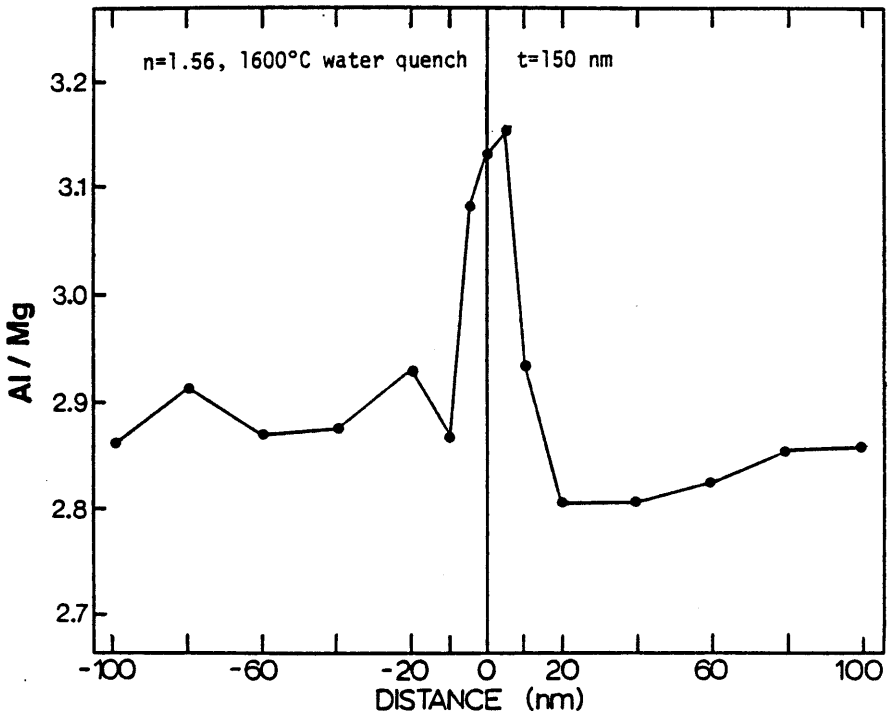

Figure 6.21 Al/Mg boundary profile in n=1.56 spinel.

VII. DISCUSSION

7.1 Impurity Tolerance of Spinel

A remarkable feature of the mobility data is the very good agreement found for nearly stoichiometric samples ($1<n<1.1$) from a variety of sources over a wide temperature range. Of the five sources of data represented in the mobilities shown in Fig. 6.4, each certainly has different background impurities and in levels of several hundred parts per million (Table 5.1) that would dominate the lattice defect chemistry of a highly stoichiometric oxide such as MgO and Al_2O_3. Yet at any given temperature we find mobilities that agree within a factor of five. Such agreement has not been found for data in either alkali halide or other oxide systems (115,116)

In all of the spinel compositions examined, Si and Ca segregation is observed. The amount of impurity varies from boundary to boundary, but in all cases it amounts to a small fraction of a monolayer segregated at the boundary plane. The possibility of undetected liquid boundary films which has sometimes been questioned in segregation studies is therefore moot; there is not enough impurity in this case to form a liquid film. The impurity segregation does not correlate with the large variations in boundary mobility in any way. Our measurement of impurity segregation in a low purity Baikowski sample (Fig. 6.14) shows considerably higher amounts of Si and Ca than the other samples plus some S

segregation, yet the mobilities of Baikowski stoichiometric hot-pressed spinel (Fig. 6.4) do not differ appreciably from purer samples. Although we cannot predict how much impurity might be present in other samples in the literature data, some S segregation is to be expected in alum-derived samples and it would be very surprising if the segregation levels of other impurities did not vary between sample sources.

It is difficult to predict which sites Si and Ca will occupy in the boundary, even though in spinels which contain these elements Ca tends to occupy tetrahedral lattice sites and Si octahedral lattice sites. Recent calculations by Duffy and Tasker (117) for impurity segregation in [110] tilt boundaries in NiO indicate that for nearly any solute there will be sites where the Madelung potential is favorable for segregation. The relative proportion of favorable sites and the energies of those sites for any given solute can be expected to vary between boundary types, and structural differences may account for the virtual absence of impurity segregant in some of our data compared with up to 0.2 monolayers in others. The specific boundary misorientations and structure have not been examined in this work. However, the presence or absence of Ca and Si segregation bears no relation to the degree of Al segregation , and is in any case always a small fraction of the grain boundary Al increase observed in these samples.

That the mobility is seemingly independent of segregated

background impurities in this system whereas in others they have a profound influence is related to the nature of the impurity and where it segregates. Since these two impurities (Ca and Si) in all likelihood segregate to sites in the boundary core, as they do in MgO (18), they are expected to have a relatively high diffusivity and to cause little drag on the boundary compared to a space-charge segregant. This is expected theoretically, and experimental measurements by Kitazawa (118) on the influence of mono and divalent cation solutes on boundary mobilities in KCL bear this out (the divalent solutes cause greater drag).

There are other background impurities present in these powders, such as Fe, Ga and Na (Table 5.1), which do not segregate in detectable quantities despite concentrations comparable to those of Ca and Si. Na may evaporate readily from the samples at the high anneal temperatures. Fe and Ga, being spinel forming cations themselves can probably substitute for Mg or Al, depending on the particular valence state, to form an effectively neutral defect. There is also the possibility of association to form a neutral defect complex if these impurities substitute in positions where they bear an effective charge.

Thus, along with our earlier conclusions that the lattice defect structure is dominated by cation inversion plus either native cation interstitials or vacancies, rather than impurities, the grain boundary migration behavior in

magnesium aluminate spinel can be said to be highly tolerant of impurities both segregated and in solid solution.

7.2 Space Charge Segregation of Native Cationic Defects

The grain growth measurements show boundary mobilities which vary sharply with Al_2O_3/MgO content near stoichiometry, increasing by two to three orders of magnitude (depending on temperature) upon proceeding from slightly Al to slightly Mg rich compositions. Outside this transition region changes in mobility with composition are comparatively minor. This dramatic change parallels a transition in the secondary lattice defects from excess cation vacancies to excess aluminum interstitials, as shown in Fig. 4.5, yet in all samples the Al/Mg ratio is found to increase at the grain boundary. There can be little doubt that these near boundary composition changes are a space charge segregation phenomenon, since there is little strain energy for the native cation defects and the Al/Mg segregation data in alumina rich spinel show considerably wider distributions (Fig. 6.21) than are usually observed for boundary adsorption.

7.2.1 The Grain Boundary Potential.

The increase in Al/Mg is consistent with a negative boundary charge and positive space charge since aluminum defect species can only bear a positive relative charge.

Upon examining all possible combinations of defect segregation and depletion, it is concluded that a positive boundary charge cannot be reconciled with the observed increase in Al/Mg ratio at grain boundaries. For this to occur given the cation defect species present in the bulk of the material, one scenario requires that lattice concentrations of V_{Mg}'' must be enough greater than that of V_{Al}''' to segregate preferentially despite their lesser charge. The concentration of Mg ions is then diminished in the space charge, which has the effect of increasing the Al/Mg ratio. (This is necessary regardless of the sample stoichiometry.) Available literature data (Section 4.3.2) instead indicate that in the lattice $[V_{Al}''']>[V_{Mg}'']$; assuming a random cation vacancy distribution at high temperatures gives the same result. Other defect distributions satisfying a negative boundary charge and an increase in Al/Mg ratio are equally unlikely.

Thus, we conclude that the boundary charge in spinel is negative and the space charge is positive in compositions within the single phase field. A potential which is relatively invariant with composition is consistent with the majority (potential determining) defects in spinel being those resulting from cation inversion, the concentrations of which do not change rapidly with sample stoichiometry. A contrasting situation is if, for instance, cation Frenkel defects dominate as in the calculation of space charge

potential in Section 2.1.1., whereupon the potential is a strong function of sample stoichiometry and changes sign from alumina rich to magnesia rich compositions as shown in Fig. 2.1.

7.2.2 Competitive Segregation of Substitutional and Interstitial Cations

Although the magnitude and sign of the electrostatic potential are determined by the defects in greatest lattice concentration, these are not necessarily the defects which segregate in highest concentration. The defects which will accumulate in the positive space charge are $Al_i^{\bullet\bullet\bullet}$, $Mg_i^{\bullet\bullet}$ and $Al_{Mg}^{\bullet}$. Although $Al_{Mg}^{\bullet}$ is always present in greater lattice concentrations, for a large enough electrostatic potential and sufficient lattice concentrations $Al_i^{\bullet\bullet\bullet}$ and $Mg_i^{\bullet\bullet}$ can segregate preferentially to $Al_{Mg}^{\bullet}$ since these species have three and two times the electrostatic driving force respectively. $Al_i^{\bullet\bullet\bullet}$ may segregate preferentially relative to $Mg_i^{\bullet\bullet}$ for the same reason. For a given potential and grain boundary charge density, clearly fewer defects of a greater charge are necessary to form the compensating space charge.

Calculations by Yan, Cannon and Bowen (17) have shown that for the competitive segregation of two aliovalent solutes of like charge but very different lattice

concentrations, if the minor solute also has substantial strain energy and therefore a larger total driving force for segregation, it will segregate preferentially to and suppress segregation of the major solute. The total electrostatic potential difference between boundary and bulk is still determined by the major solute, but the detailed space charge potential distribution and even the sign and magnitude of the grain boundary charge (which are related to the space charge field through Gauss' law) can be significantly altered by segregation of the minor solute. In the present case an analogous effect may result; the potential difference is fixed by cation inversion, but if cation interstitials are present in high enough concentrations these may segregate preferentially to satisfy the space charge potential distribution, reducing the magnitude of $Al_{Mg}^{\bullet}$ segregation and Mg_{Al}' depletion which might occur otherwise.

We then have a qualitative basis for understanding the higher grain boundary mobility in magnesia rich spinel, in terms of the controlling, segregated defect species being cation interstitials, as opposed to the mobility controlling defects being $Al_{Mg}^{\bullet}$ and Mg_{Al}' in stoichiometric and alumina rich spinel. In magnetite the iron interstitial is found to be more mobile than the iron vacancy alone (88), and therefore much more mobile than lattice iron; from this it seems likely that in magnesium aluminate the cation interstitials are much more mobile than $Al_{Mg}^{\bullet}$ and Mg_{Al}' which

diffuse by vacancy mechanisms. Furthermore, in the space charge region, the cation vacancy concentration is reduced by electrostatic repulsion and therefore the diffusivity of lattice cations is even less than in the bulk, whereas the interstitial diffusivity is approximately unchanged.

7.2.3 Defect Segregation and Mobility Model.

The solute drag problem that magnesium aluminate spinel presents is, from the point of view of calculations, subject to many uncertainties given the present data base. Individual defect formation energies are not known with any degree of certainty. The experimentally observed segregation indicates grain boundary charge densities of monolayer proportions, suggesting that the assumption of ideal source/sink behavior may be invalid and that the potential may be influenced by grain boundary site saturation. The segregated concentrations are such that a continuum space charge model of the segregant distribution is almost certainly invalid; calculated space charge widths from continuum electrostatics are of subatomic dimensions. Due to these shortcomings, a calculation of the equilibrium space charge defect and potential distributions by solving Poisson's equation subject to certain boundary conditions, as has been done for example by Kliewer and Koehler (15) and Yan, Cannon and Bowen (17) for alkali halides, has not been attempted.

We can, however, estimate the lattice defect

concentrations from the defect model presented in Chapter 4, and with additional approximations regarding the spatially varying form of the potential and solute layers in the space charge, determine the boundary potential empirically from the experimental results. The grain boundary mobility corresponding to such a model of the space charge defect distributions can be carried out for limiting conditions in alumina and magnesia rich spinel, with results that support the qualitative explanation presented above.

The increases in Al/Mg ratio at grain boundaries in these samples reflect the net result of cation defect accumulations and depletions in the space charge region as well as changes in the boundary core. We have no information on the boundary core defect structure that accomodates a negative charge other than that there is a deficiency of cations or excess of anions (some speculations regarding the charged boundary structure are discussed in Section 7.4). However, assuming that it is composed of defects that cause no change in the Al/Mg concentration (e.g., a stoichiometric ratio of cation vacancies for a negative boundary) and therefore considering all Al/Mg concentration changes to take place in the space charge, we can model the segregation of defects as follows.

Charged defects which will segregate or deplete from the space-charge are those included in the Brouwer diagram (Fig. 4.3):

$Al_{Mg}^{\bullet}$, Mg_{Al}', $Al_i^{\bullet\bullet\bullet}$, $Mg_i^{\bullet\bullet}$, V_{Al}''', V_{Mg}''.

Anion defects are assumed to be energetically unfavorable and present in negligible concentrations. For simplicity no distinction is made between octahedral and tetrahedral interstitial sites; as described earlier the ratio of the two interstitial concentrations is a function of temperature but not concentration. The above defects are assumed to have negligible strain energy compared to the electrostatic potential energy near the boundary, which will certainly be true for an electrostatic potential of at least a few tenths of an electron volt. We will assume that the defects are fully ionized, and therefore the relative charges remain as assigned above.

7.2.3.1 Lattice Defect Concentrations

The defect concentrations far from the boundary are calculated as follows.

A random distribution of the total number of cation vacancies on octahedral and tetrahedral sites will be assumed, such that $[V_{Mg}'']=1/2[V_{Al}''']$.

In alumina rich spinel, the cation vacancy concentration is calculated from the alumina/magnesia molar ratio, n, as:

$$[V_{total}] = (n-1)/(9n+3) \qquad (7.3)$$

and the $Al_{Mg}^{\bullet}$ concentration resulting from the excess of alumina is 5/3 $[V_{total}]$ (c.f. the incorporation reaction for excess alumina with a random vacancy distribution, Eq. 4.15).

At high temperature there will be probably also be a distribution between aluminum and magnesium interstitials, as discussed in Chapter 4. The total interstitial concentration due to magnesia excess is given by:

$$[Al_i^{\bullet\bullet\bullet} + Mg_i^{\bullet\bullet}] = (1-n)/(3n+1) \qquad (7.4)$$

and we will arbitrarily assume the concentrations of the two are equal:

$$[Al_i^{\bullet\bullet\bullet}] = [Mg_i^{\bullet\bullet}]. \qquad (7.5)$$

The excess Mg_{Al}' is, from Eqs. 4.17 and 4.18, equal to 5/2 $[Al_i^{\bullet\bullet\bullet} + Mg_i^{\bullet\bullet}]$.

In stoichiometric spinel the cation vacancy and interstitial concentrations are determined by a Frenkel equilibrium for which we will assume a formation energy of 3.2 eV:

$$[Al_i^{\bullet\bullet\bullet} + Mg_i^{\bullet\bullet}][V_{Al}'''] = 100 \exp [-3.2 \text{ eV}/kT] \qquad (7.5)$$

The pre-exponential factor of 100 is chosen arbitrarily to correspond with the most commonly observed range of values for Frenkel disorder ($\exp(S_f/k) \approx 100-10000$, 119).

In stoichiometric spinel the inversion parameter (fraction of tetrahedral sites occupied by Al^{3+} ions) is taken to be 0.3, which from Fig. 4.2 is reasonable for the temperature range of interest (1300°-1600°C). In terms of the present concentration units (fraction of the total number of normal cation lattice sites) this is:

$$[Al_{Mg}^{\bullet}] = [Mg_{Al}'] = 0.1 \qquad (7.6)$$

And the cation inversion equilibrium then gives:

$$[Al_{Mg}^{\bullet}][Mg_{Al}'] = 0.01 \qquad (7.7)$$

In alumina rich spinel, the total $Al_{Mg}^{\bullet}$ concentration is approximated as the sum of the excess and that resulting from cation inversion:

$$[Al_{Mg}^{\bullet}] = 0.1 + 5/3\ (n-1)/(9n+3)\ ; \qquad (7.8)$$

and the corresponding Mg_{Al}' concentration is determined from Eq. 7.7. Similarly, in magnesia rich spinel the Mg_{Al}' concentration is approximated as:

$$[Mg_{Al}'] = 0.1 + 5/2\ (1/n)/(3n+1) \qquad (7.9)$$

and $[Al_{Mg}^{\bullet}]$ is determined from Eq. 7.7.

7.2.3.2 Space Charge Defect and Potential Distributions

Instead of using a Boltzmann distribution for the defect concentrations as a function of distance from the boundary, x, in the space-charge:

$$n_i(x) = n_{i,o} \exp[z_i\ e\ \underline{\phi}(x)/kT] \qquad (7.1)$$

where $n_{i,o}$ is the lattice defect concentration of species i, z_i is the defect effective charge, e the electronic charge, and $\underline{\phi}(x)$ the electrostatic potential (referenced to zero in the bulk of the material rather than at the boundary as is often used), we will use a Fermi-Dirac distribution, essentially the same as McLean's expression (19), which is applicable for high concentrations:

$$n_i(x)/(\beta_i - n_i(x)) = [n_{i,o}/(\beta_i - n_{i,o})] \exp[z_i\ e\ \underline{\phi}(x)/kT] \qquad (7.2)$$

where β_i is the fraction of lattice sites available to the defect n_i; i.e. the saturation value for segregation.

Concentrations will be taken relative to the total number of cation sites in the spinel structure. Thus, β_i for the defects $Al_i^{\cdot\cdot\cdot}$, $Mg_i^{\cdot\cdot}$, $Al_{Mg}^{\cdot}$, Mg_{Al}', V_{Al}''' and V_{Mg}' are 3, 3, 1/3, 2/3, 2/3 and 1/3 respectively. If the interstitial defects prefer one type of interstitial site to the other, then their β value will be reduced, to 7/3 for tetrahedral occupation only and 2/3 for octahedral occupation only. It is probable that $Al_i^{\cdot\cdot\cdot}$ or $Mg_i^{\cdot\cdot}$ cannot occupy all of the available intersitial sites in the space charge region since at such high concentrations interactions between defects would seem important; a value of 1 is perhaps reasonable and will be used in this calculation.

Taking the space charge to be composed of multiple layers of solute in accordance with observations of the aliovalent solute distribution in MgO (18), the space charge distribution is modeled as multiple layers with a Debye length Γ equivalent to five atomic layers (≈20 angstroms).

The potential is well approximated by an exponentially decaying function (15):

$$\bar{\varphi}(x) = \bar{\varphi}_o \exp[-x/\Gamma] \qquad (7.12)$$

where $\bar{\varphi}_o$ is the potential at the grain boundary, which we will determine empirically.

Let us start with a spinel of n=1.013 composition at 1600°C. Upon calculating lattice defect concentrations from Eqs. 7.3-7.9, and space charge distributions for each defect from Eq. 7.2, and then integrating the total change in Al/Mg

ratio across the two space charge regions at a grain boundary, it is found that a ϕ_o value of 0.25 V yields a calculated concentration change across the space charge regions of 1.3 equivalent monolayers, close to the experimental average for the nearly stoichiometric (n=1.013) sample of 1.2 equivalent monolayers (Fig. 6.19). The corresponding space charge distibutions of $Al_{Mg}^{\bullet}$, Mg_{Al}', $Al_i^{\bullet\bullet\bullet}$ and $Mg_i^{\bullet\bullet}$ are shown in Figure 7.1; the vacancies that are repelled from the space charge (V_{Al}''',V_{Mg}'') are not shown. Notice that the composition change arises almost entirely from segregation of $Al_{Mg}^{\bullet}$ and Mg_{Al}'; there is virtually no segregation of the interstitial species.

Since the total formation energy for the majority defects, i.e. the inversion energy, is only ≈0.4 eV (≈10 ~~kcal~~/mole), the calculated potential assuming ideal source/sink behavior is a function of the difference between the unknown individual defect formation energies, and will be smaller. A potential of 0.25 V seems higher than expected, but given uncertainties in the inversion enthalpy values and the high grain boundary charge density which suggests site saturation effects may be important, this empirical potential value of 0.25 V is within reason. Furthermore, since the lattice concentration of majority defects, $Al_{Mg}^{\bullet}$ and Mg_{Al}'do not change very rapidly with deviations from stoichiometry, it is safe to assume this value of the grain boundary potential will apply for compositions not too far from

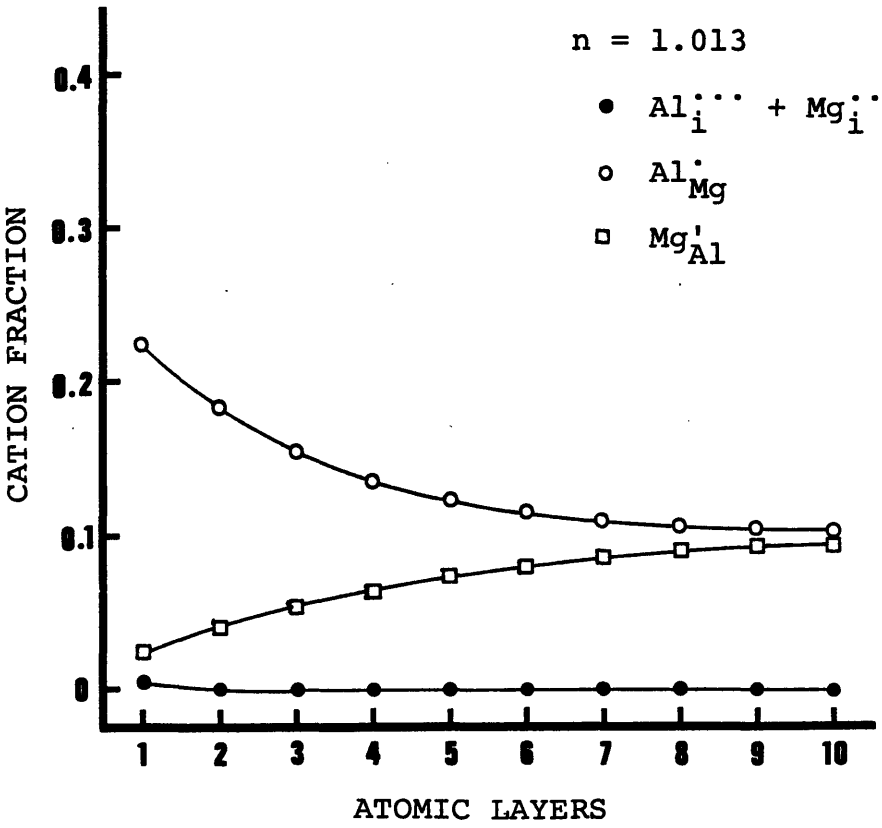

Figure 7.1 Defect segregation in n=1.013 spinel; multiple layer model of space charge.

stoichiometry.

Using a potential of $\mathfrak{F}_O$=0.5 V, it is found that cation interstitial segregation increases rapidly with magnesia excess such that near the boundary one has interstitial concentrations greater than the segregated $Al_{Mg}^{\bullet}$ concentrations in stoichiometric to alumina rich spinel. In Fig. 7.2 are shown the distributions of $Al_i^{\bullet\bullet\bullet}$ and $Mg_i^{\bullet\bullet}$ in n=0.957 spinel, and in Fig. 7.3 are shown the total charge density due to interstitial segregation in this composition compared with that corresponding to the defect distributions for n=1.013 spinel in Fig. 7.1. The positive charge density carried by interstitial segregation is clearly much greater than that which results from $Al_{Mg}^{\bullet}$ segregation and Mg_{Al}' repulsion in the absence of interstitials; however, it is not clear from the present calculations how much the segregation and repulsion of the latter species are suppressed by the large amount of interstitial segregation. Let us assume as a limiting condition that no segregation of $Al_{Mg}^{\bullet}$ or depletion of Mg_{Al}' occurs in the presence of high interstitial segregation, and calculate the drag and mobility corresponding to interstitial segregation alone in magnesia rich spinel (e.g. corresponding to Fig. 7.2), and compare these results to the defect drag and mobility in alumina rich spinel where interstitial segregation is negligible.

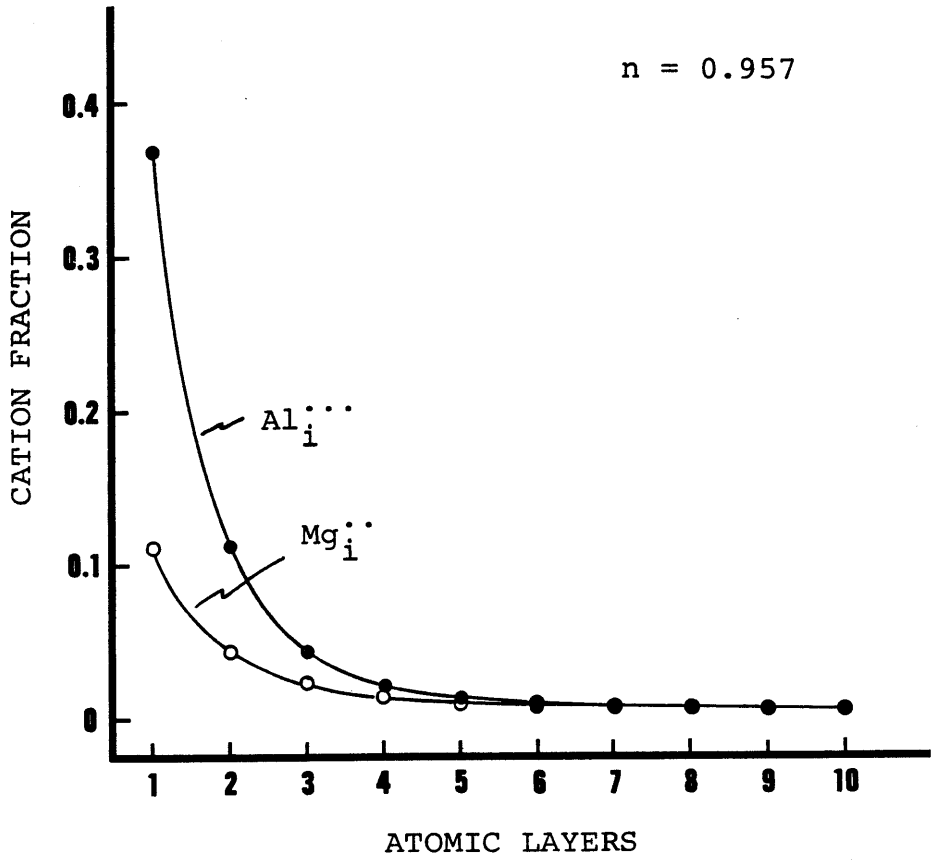

Figure 7.2 Interstitial segregation in n=0.957 spinel; multiple layer model.

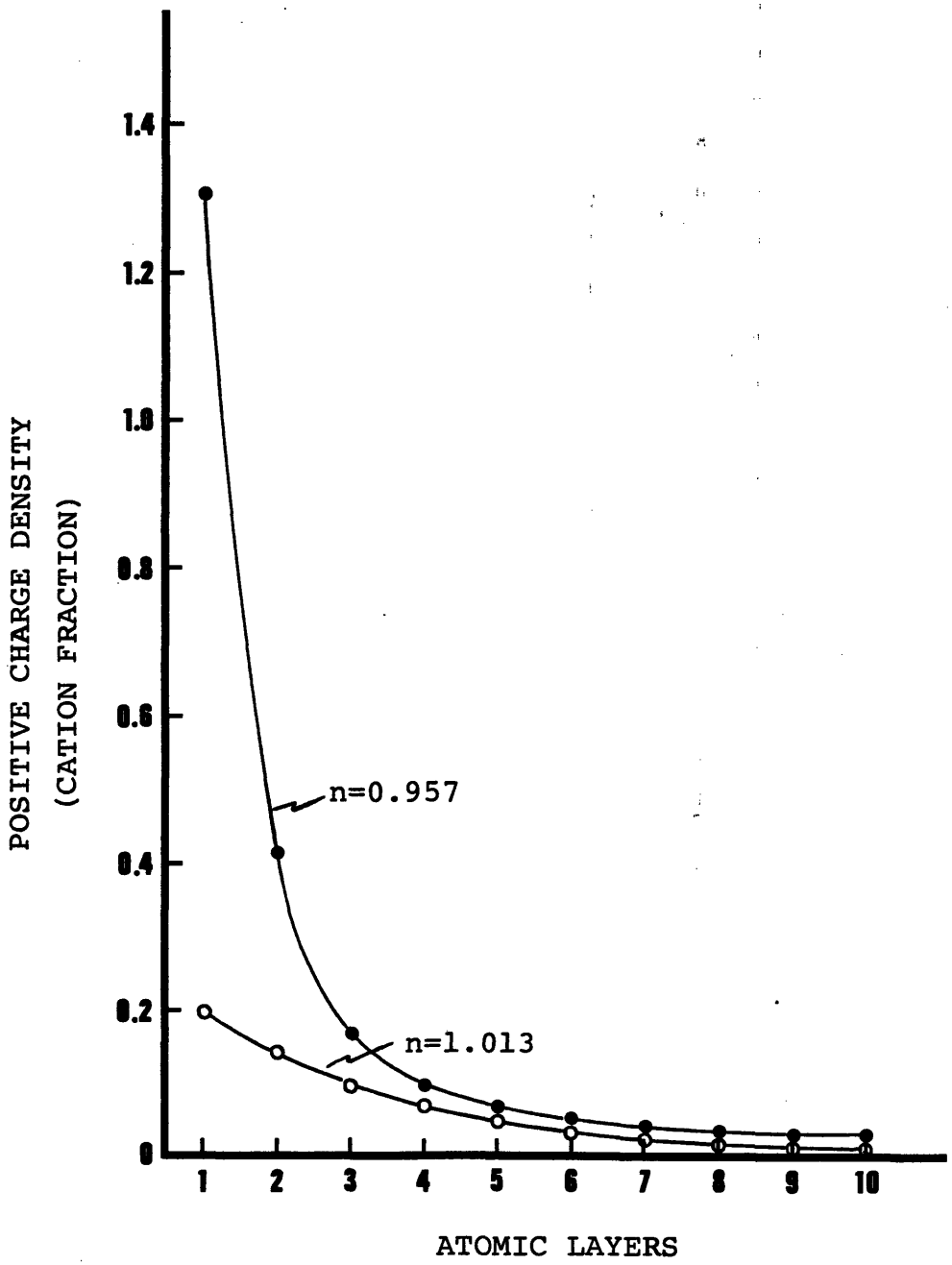

Figure 7.3 Space charge positive charge density corresponding to n=1.013 and 0.957 spinel defect distributions from Figs. 7.1 and 7.2 respectively.

7.2.3.3 The Mobility

From Cahn's theory (2), the grain boundary mobility in the low velocity solute-drag controlled regime is given by:

$$M_b = 1/(\alpha n_{i,o}) \qquad (7.13)$$

where α is the drag force per unit concentration per unit velocity, and $n_{i,o}$ is the lattice solute concentration. For a dilute solute segregated in a boundary layer of width δ, Eq. 7.13 has been approximated as (120):

$$M_b=(\Omega/2\delta RT)\{n_{i,o}\exp[z_i\ e\ \bar{\Phi}(\delta)/kT]/D(\delta)\}^{-1} \qquad (7.14)$$

where Ω is the molar volume, $D(\delta)$ the solute diffusivity in the segregated layer, $n_{i,o}$ the bulk concentration (thus the Boltzmann distribution is used) and $\bar{\Phi}(\delta)$ the potential at the layer δ. If the concentrations are not dilute, we can more generally write:

$$M_b=(\Omega/2\delta Rt)[|n_{i,\delta} - n_{i,o}|/D(\delta)]^{-1} \qquad (7.15)$$

where $n_{i,\delta}$ is calculated using Eq. 7.2. The absolute value of the concentration change in Eq. 7.15 corresponds to the fact that depleted defects (primarily Mg_{Al}' in this case) cause drag also.

For a defect segregating in multiple layers, we can modify Eq. 7.15 by summing over j layers:

$$M_b=(\Omega/2\delta RT)\ \Sigma_j\ [|(n_{i,j}-n_{i,o})|/D_{i,j}]^{-1} \qquad (7.16)$$

The diffusivities of $Al_{Mg}^{\bullet}$ and Mg_{Al}' will be assumed to be proportional to the local vacancy concentration:

$$D(Al_{Mg}^{\bullet},\delta) = [V_{Mg}'']\,(\delta)D_V \qquad (7.17)$$

$$D(Mg_{Al}',\delta) = [V_{Al}''']\,(\delta)D_V \qquad (7.18)$$

where D_V is the calculated vacancy diffusivity in Fig. 3.4. The interstitial diffusivities are unknown, and will simply be assumed equal to the vacancy diffusivity, D_V.

Calculated mobilities at 1600°C for alumina rich spinel (drag from all species) and for magnesia rich spinel (intersitial drag only) are shown in Fig. 7.4 as solid curves along with the experimental measurements. The integrated Al excess (from two space charge layers) corresponding to this calculation are shown in Fig. 7.5 along with the range of STEM measured values.

On the alumina rich side of stoichiometry, a continuously increasing mobility results due to $Al_{Mg}^{\bullet}$ and Mg_{Al}' diffusivities that increase with the cation vacancy concentration. This curve for constant boundary potential with stoichiometry is similar to the results shown by Uematsu et al. (6) for alumina rich spinel (Fig. 3.6). The present experimental results exhibit an increase nearer to stoichiometry followed by a decrease at higher alumina contents, which can be explained by an increasing boundary potential when the alumina excess is sufficient to alter the cation inversion equilibrium. A greater boundary potential causes increased segregation as well as greater vacancy depletion in the space charge, and thus more drag. As Fig. 7.5 shows, the measured segregation does increase with alumina excess whereas the calculated result does not.

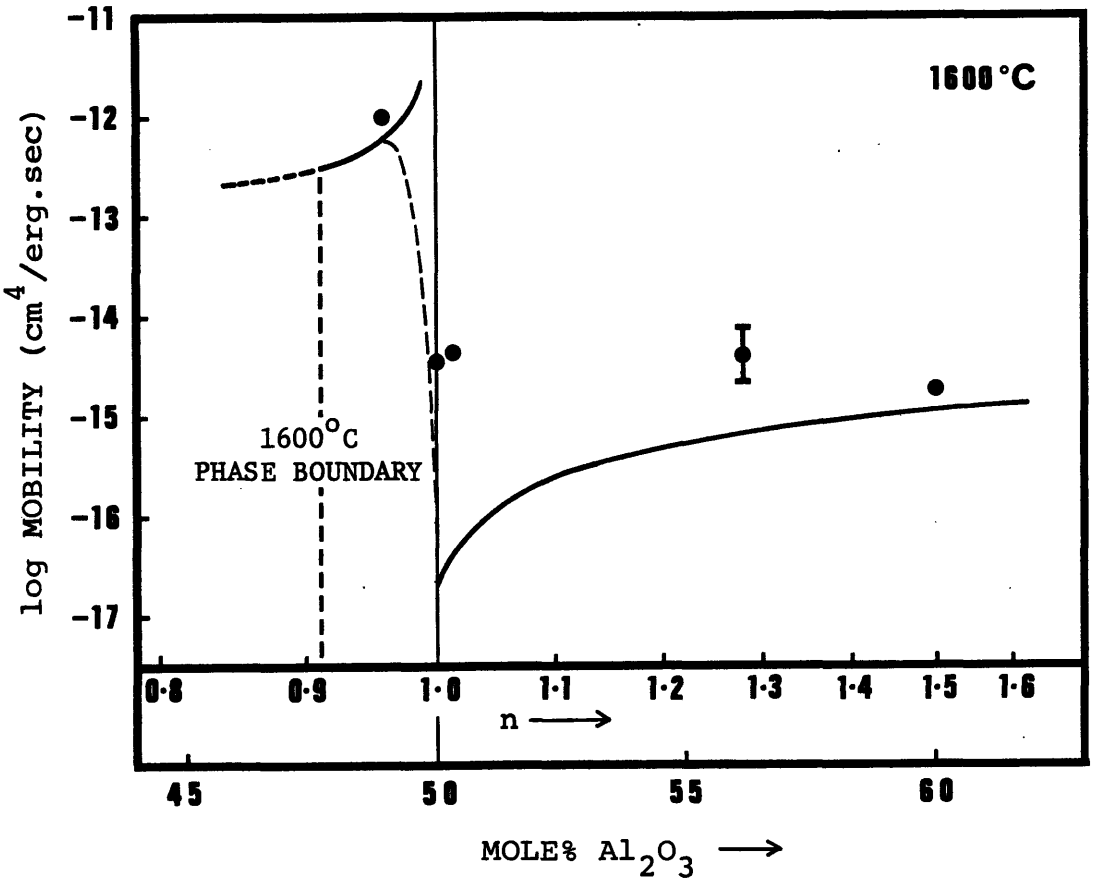

Figure 7.4 Calculated mobilities for alumina and magnesia rich spinel at 1600°C according to model in text, compared with experimental measurements.

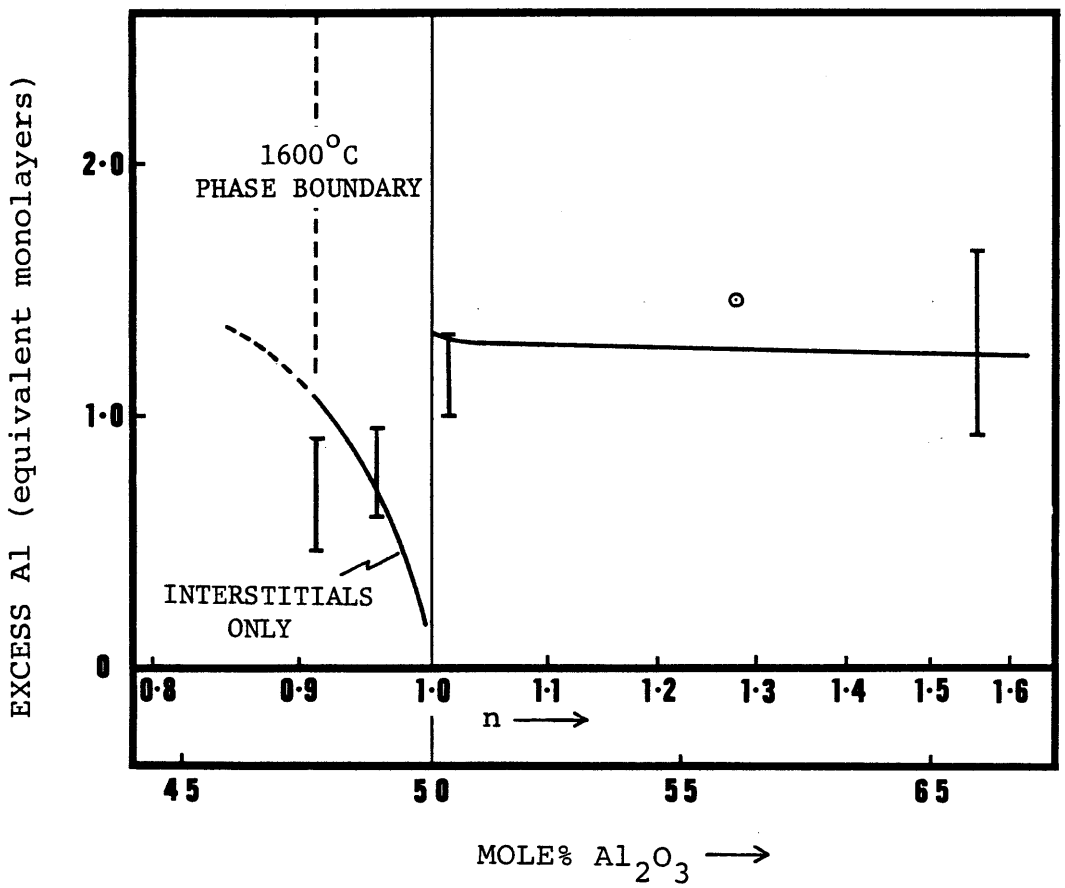

Figure 7.5 Integrated excess aluminum at grain boundaries corresponding to mobilities in Fig. 7.4, compared with range of experimentally observed values.

In magnesia rich spinel, the calculated total aluminum excess due to greater Al than Mg interstitial segregation is a rapidly changing function of composition (i.e. lattice intersitial concentrations) but is close to the measured range of values for n=0.957 and magnesia saturated compositions (Fig. 7.4). The mobility due to drag from interstitials alone, Fig. 7.3, is indeed orders of magnitude greater than calculated and measured mobilities in alumina excess spinel. Closer to stoichiometry on the magnesia excess side, however, one expects a rapid decrease in mobility as the interstitial segregation decreases and drag from substitutional defects once again become the controlling mechanism.

Clearly these calculated results are very approximate. Since many assumptions have been made for relevant parameters such as the defect diffusivities and their dependence on vacancy concentration, the relative concentrations of aluminum and magnesium interstitials, the space charge width and segregation saturation values, to attach much significance to the numerical results is unwarranted. The calculated mobility in nearly stoichiometric spinel is $\approx 10^2$ less than is measured, and the good agreement between calculation and experiment for the magnesia rich mobility is probably fortuitous. Much more information regarding actual defect spatial distributions and concentrations, and especially defect diffusivities, is necessary for a more

more exact comparison between the model and experimental results. The large difference in mobility between interstitial and substitutional cation controlled regimes is the most important feature illustrated by the present calculation, and this is consistent with our interpretation of the experimental results.

It is to be emphasized that there are two regimes of defect-segregation controlled migration behavior in alumina excess and in magnesia excess spinel respectively, and not a peak in mobility along an otherwise continuous background mobility as Uematsu et al.'s results (6) first suggested. These results illustrate the influence that changes in the lattice defect structure of magnesium aluminate, upon proceeding from alumina rich to magnesia rich compositions, have on the defect composition on the space charge regions and consequently on the boundary mobility.

7.3 The Temperature Dependence of Mobility

It is often said that the activation energy for grain boundary migration should be close to the diffusion activation energy of the controlling solute. For solutes that segregate to the grain boundary core region, this energy may be in between the values for grain boundary diffusion and lattice diffusion, whereas for space charge solutes, it is expected to be closer to the lattice diffusion activation energy. However, if we examine the expression for mobility

(Eq. 7.14 and 7.15), it is found that this will only be true if the concentration of segregated solute does not change with temperature. Otherwise the temperature dependence of mobility includes a concentration term which can be large ($\exp[-z_i e\phi/kT]$ for a charged species).

The few temperature dependent STEM results measured here indicate that the amount of aluminum segregation does not to first approximation change with temperature (Fig. 6.19). Since the amounts segregated correspond to a monolayer or more of grain boundary charge, it may be that the boundary is approximatedly saturated within the experimental temperature range.

The activation energies for boundary migration that are measured do correspond well with solute diffusion activation energies. In alumina rich spinel (n=1.56), the mobility activation energy (2.57 eV) is close to that for ionic conduction in alumina rich single crystals, which has been attributed to vacancy migration (56). The mobility in nearly stoichiometric spinel exhibits an energy 1.8 eV higher.

Taking the 1.8 eV difference to be one-half the Frenkel defect formation energy, the data are consistent with a vacancy diffusion mechanism for segregated $Al_{Mg}^{\bullet}$ in stoichiometric spinel, with a total activation energy containing both motion and concentration terms, $E_M + E_{Frenkel}/2$. The inferred Frenkel formation energy of $\approx$3.6 eV

is close to that from Yamaguchi et al.'s data (60) of 3.2 eV, is not unreasonable compared with that indicated for Fe_3O_4 of 2-2.7 eV (85) (see Section 4.3.1). For alumina rich spinel the lattice vacancy concentration is fixed by nonstoichiometry and so the activation energy is that for motion alone. In the magnesia rich samples, no comparisons with literature are possible, but the activation energy of ≈3.0 eV is not unreasonable for an interstitial mechanism.

7.4 Grain Boundary Core Charge and Defect Structure

In both this work and earlier Auger spectroscopy measurements of Sc segregation in MgO (18), segregation of charged solute species corresponding to at least a monolayer of grain boundary core charge has been measured. If the defects which give rise to the core charge are of valence +/-2, such as cation vacancies, oxygen interstitials, or some combination of the two, a half-monolayer or more of these species must be absent/segregated at the boundary core. Compared to what is necessary to accomodate the smaller potential and boundary charge density in alkali halides (17) which have lower defect formation energies and can be obtained in higher purities, charge densities of this magnitude initially seem improbably high.

Recent computer simulations by Duffy and Tasker (120) treat the formation of boundary and space charge at special tilt boundaries in NiO more exactly than in the continuum

formulations by determining lattice defect formation energies at specific sites in specific boundary structures. It is found that while there is a spectrum of defect formation energies, some of which may be greater than the corresponding bulk values, sites of lower formation energy do exist and, the energies being unequal for oppositely charged defects, lead to charged boundary cores and compensating space charges as expected. These are, however, calculations for ideally pure materials. What is more interesting with respect to doped ionics is that the relaxed boundary structures are quite open, e.g. a (310)/[001] tilt boundary contains a Schottky pair per unit of periodicity, which is a high concentration of vacancies, and these simple tilt boundaries also contain ample intersitial sites. It is then perhaps not so surprising that boundary charges of monolayer proportions are possible. For instance, an extra quarter-monolayer of oxygen interstitials and cation vacancies respectively in an MgO grain boundary would yield a monolayer of charge. Since it is not clear from available experimental data whether or not saturation of grain boundary sites is reached with aliovalent doping of the more refractory oxides, another possibility may be that the boundary structure changes as a function of the doping level in order to accomodate the boundary charge. There may also be a coupling between the available density of sites for charged defects and the concentration of boundary core segregants.

7.5 Extensions to Other Systems

The present results on magnesium aluminate are clearly extendable to other spinel systems with similar defect structures, although to our knowledge there has not been sufficient data gathered on any other system to illustrate that this is the case. It is interesting also to consider aspects of other ternary systems which may make their behavior different from magnesium aluminate.

In the absence of detailed information on the origin of the negative grain boundary charge and positive space charge in magnesium aluminate, it can not be predicted that the same respective charges will exist in other materials. If the sign of the boundary and space charge are reversed in spinel, for instance, the negatively charged species that will segregate are cation vacancies and the negatively charged substitutional cation. Grain boundary mobilities are likely to be very high indeed in this case as near boundary cation diffusivities will be enhanced. An excess of the cation of higher valence will always make the space charge more positive; thus in principle it is possible to have a system for which the potential goes through zero at some composition, at which point the mobility will reach the intrinsic value.

Compounds which are electronic conductors present an interesting case, for if electronic carriers compensate the

space charge they will cause virtually no drag. However, it is insufficient for the material to simply conduct electronically since at equilibrium it is the concentration of electronic carriers compared to ionic defects which determines the relative space charge distributions; because of the mobility ratio, an electronic conductor may still have a majority of ionic defects. This consideration may be important in ferrite and titanate systems, for example.

Segregated transition metal cations may also behave quite differently from those of fixed valence. For example, in Fe_3O_4 in the high oxygen pressure cation vacancy regime (analogous to alumina excess spinel), a positive space charge consisting of an excess of Fe^{3+} ions may be expected to cause little grain boundary drag since no cation motion is required to move the charge distribution; electron hopping accomplishes the same thing. In $FeAl_2O_4$ on the other hand, segregation of Al^{3+} defect species would result in quite a different situation. In Fe_3O_4 in the low oxygen pressure interstitial dominated regime, segregated cation interstitials would require cation diffusion to move the space charge distribution, and may result in more drag than on the high oxygen pressure side, in contrast to the analogous case for magnesium aluminate.

VIII. CONCLUSIONS

The grain boundary mobility in magnesia-rich, alumina-rich and nearly stoichiometric magnesium aluminate spinel has been measured from parabolic grain growth at temperatures within the single phase field. Magnesia-rich samples exhibit a 10^2 to 10^3 greater boundary mobility, depending on temperature, than either alumina-rich or nearly stoichiometric samples. This large increase occurs with relatively little excess magnesia (<5 mole %); with greater magnesia excess the mobility remains high and approximately unchanged up to the phase boundary. With excess alumina, the mobility appears to increase slightly and then decrease, but the total variation up to a composition of n=1.56 is less than a factor of 5 at temperatures up to 1700°C.

Analysis of grain boundary impurity segregation by scanning transmission electron microscopy shows Ca and Si segregated in minor amounts (<0.2 monolayers) that do not, within the resolution of the analysis, vary in any systematic way with stoichiometry. Enrichment of aluminum in much greater quantities is found at grain boundaries in all samples, regardless of bulk stoichiometry. Slightly magnesia rich compositions exhibit less aluminum enrichment than nearly stoichiometric or substantially alumina rich ones. With increasing aluminum excess in the lattice, the amount of segregated aluminum increases.

A review of the literature indicates the following as

the most probable model of the lattice defect structure. The predominant lattice defects in stoichiometric spinel are antisite defects created through cation inversion; $Al_{Mg}^{\bullet}$ and Mg_{Al}'. These are therefore the defects that determine the boundary potential. Secondary defects are cation interstitials and vacancies from a Frenkel mechanism. Excess alumina in solid solution is accomodated as $Al_{Mg}^{\bullet}$ and cation vacancies, whereas excess magnesia is accomodated as Mg_{Al}' and cation interstitials. At high temperatures the vacancies are probably randomly distributed on octahedral and tetrahedral sites, and the interstitials probably include both magnesium and aluminum species.

Since segregated aluminum at grain boundaries can only exist in the presence of a negative grain boundary charge and positive space charge, it is proposed that the segregation in magnesia rich spinel is predominantly in the form of cation intersitials, whereas that in stoichiometric and alumina-excess spinel is in the form of substitutional cations. The much higher mobility in magnesia-excess spinel results from the much higher diffusivity of cation interstitials in spinel as compared to lattice cations which diffuse by vacancy mechanisms. On the alumina rich side of stoichiometry, with increasing alumina content the segregation of $Al_{Mg}^{\bullet}$ is greater, but its influence on the boundary drag is counterbalanced by a simultaneously increasing aluminum diffusivity.

The temperature dependence of mobility compares reasonably well with expected activation energies for cation diffusion in stoichiometric and alumina-rich compositions in that the vacancy concentration is not a function of temperature in alumina rich spinels, hence the activation energy is lower than that in stoichiometric spinels where the temperature dependence also includes a term equal to one-half the cation Frenkel formation energy.

In nearly stoichiometric spinel, grain boundary mobilities from several literature sources and those measured here agree closely in a way that is unprecedented for oxides. At any temperature in the experimentally observed range, the grain boundary mobilities agree within a factor of five despite what are certainly different impurity levels in each source of data. These are impurity levels (>200 ppm aliovalent impurities) that would dominate the defect structure of a highly stoichiometric oxide such as MgO or Al_2O_3. However, the impurity tolerance of grain boundary mobility in spinel is reasonable given a lattice defect structure and grain boundary segregation that is determined by the host cation that is in excess, together with native cation defects of low formation energies. One may expect other spinel and ternary systems to be similarly impurity tolerant, and to exhibit grain boundary mobilities which vary with stoichiometry in a way that can be understood in terms of the detailed lattice defect structure for each system.

APPENDIX 1. Debye-Scherrer X-ray Measurement of Lattice Parameters

A 114.59 mm diameter camera was used with Ni-filtered Cu radiation. Only clearly resolved doublets or single lines in the high angle ($\theta>45°$) zone were used; 17 such line pairs were measured from each film as listed in Table A-1. Correction for film shrinkage was done by determining the beam entrance coordinate, X_{180}, and exit coordinate, X_0, as the average of the midpoints for the line pairs measured. The true angle of each line was determined relative to the corrected camera diameter (after film shrinkage) as:

$$\theta_{hkl} = 90[1 - (X_{hkl}-X_{180})/(X_{180}-X_0] \quad \text{(degrees)}$$

The Nelson-Riley function, $\cos^2\theta/\sin\theta + \cos^2\theta/\theta$, was used to extrapolate to $\theta=90°$ for the absorption-corrected lattice parameter (98). The precision of this measurement is on the order of 0.0005 angstroms.

Small samples of each powder composition and also the nearly stoichiometric sample hot-pressed by Rhodes were annealed at 1600°C for 1/2 h. in air and rapidly air cooled before Debye-Scherrer measurement. The most magnesia rich sample (n=0.88) was annealed at 1700°C for 15 min. instead, to ensure solid solution. The results showed that as with the literature data described in Section 5.2, there is no change in lattice parameter between stoichiometry and single phase magnesia excess compositions, but there is a linear decrease with alumina excess (Figure 5.2).

Table A-1. Debye-Scherrer X-ray Lines Used for Lattice Parameter Measurements in Magnesium Aluminate

hkl	Cu-wavelength
800	K-alpha 1
800	K-alpha 2
822	K-alpha 1
751	K-alpha 1
751	k-alpha 2
840	K-alpha 1
840	K-alpha 2
911	K-alpha 1
931	K-alpha 1
931	K-alpha 2
844	K-alpha 1
844	K-alpha 2
933	K-alpha 1
10 20	K-alpha 1
10 20	K-alpha 2
951	K-alpha 1
951	K-alpha 2

APPENDIX 2. Convergent Beam Electron Diffraction Measurements as a Standard for Foil Thickness

A means of estimating the foil thickness for each grain boundary segregation analysis without the tedium of individual convergent beam diffraction measurements was desired. The X-ray count rate from a foil region, normalized to the electron beam current, measured at the STEM objective aperture, should increase linearly with foil thickness. If so, a standard can be used to determine the thickness of the analyzed region as a function of normalized X-ray count rate.

For this purpose convergent beam diffraction measurements of foil thickness (122,123) were made on a stoichiometric spinel foil along a gradient in thickness, using the g_{400} reflection, and the X-ray count rate and beam current measured at each point. The resulting plot of normalized Al Kα count rate vs. foil thickness was indeed linear (Figure A-1), from 800-1500 angstroms. This plot was then used as a standard to estimate the thickness of each analyzed grain boundary region, although the range of foil thicknesses for segregation results is greater (1500-3500 angstroms).

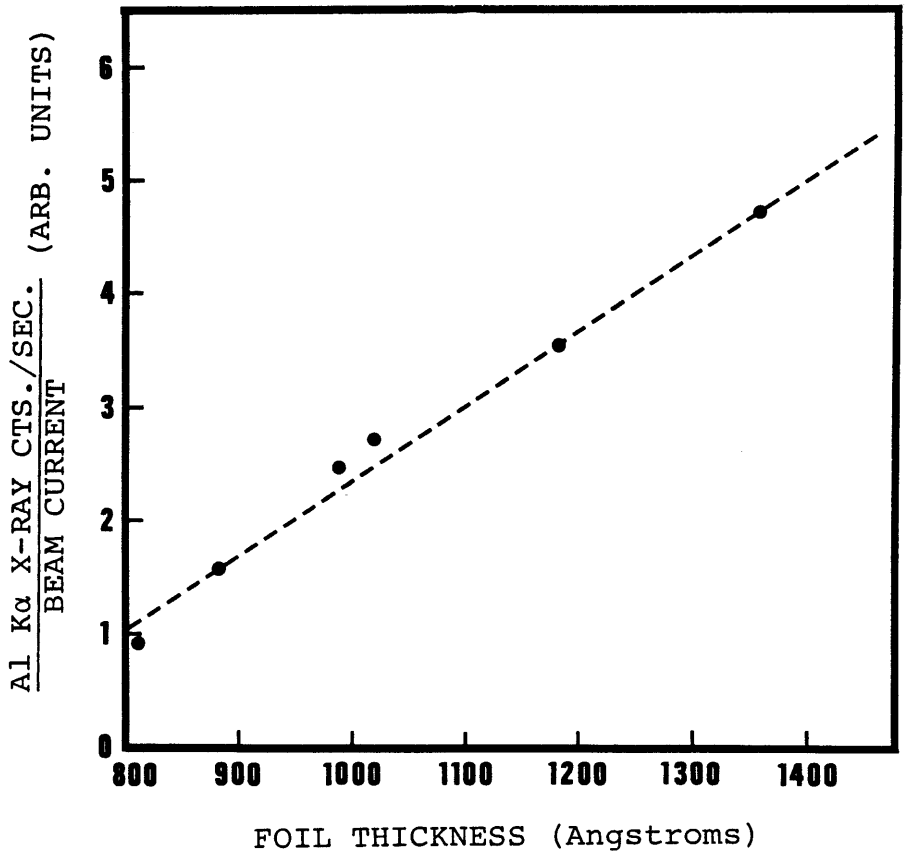

Figure A-1 Al Kα X-ray count rate normalized to electron beam current vs. foil thickness from convergent beam diffraction measurements.

BIBLIOGRAPHY

1. W.D. Kingery, "Plausible Concepts Necessary and Sufficient for the Interpretation of Grain Boundary Phenomena", J. Am. Ceram. Soc. 57[2] 74-83 (1974).

2. J.W. Cahn, "The Impurity-Drag Effect in Grain Boundary Motion," Acta Met. 2[9] 789-798 (1962).

3. K. Luecke and H.P. Stuewe, "On the Theory of Grain Boundary Motion," pp.171-210 in Recovery and Recrystallization of Metals, L. Himmel, Ed., Gordon and Breach, New York, 1962.

4. E. Sonder, "Ionic Transference Numbers and Electrical Conduction in $MgAl_2O_4$ Spinel," J. Am. Ceram. Soc. 66[1] 50-53 (1983).

5. A.M. Glaeser, "Grain Boundary Mobility in LiF," Sc.D. Thesis, M.I.T., 1981.

6. K. Uematsu, R.M. Cannon, R.D. Bagley, M.F. Yan, U. Chowdry and H.K. Bowen, "Microstructure Evolution Controlled by Dopants and Pores at Grain Boundaries," pp.190-205 in Proc. Int. Symp. Factors in Densification and Sintering of Oxide and Non-Oxide Ceramics, 1978.

7. F.W. Clinard, Jr., "Ceramics for Application in Fusion Systems," J. Nucl. Mat. 85-86 393-404 (1979).

8. C.A. Parker, "Fast Neutron and Electron Irradiation Damage in Magnesium Aluminate and Aluminum Oxynitride Spinels," Ph.D. Thesis, M.I.T., 1984.

9. J. Frenkel, Kinetic Theory of Liquids, Oxford University Press, New York, 1946.

10. K. Lehovec, "Space-charge Layer and Distribution of Lattice Defects at the Surface of Ionic Crystals," J. Chem. Phys. 21[7] 1123-1128 (1953).

11. J.D. Eshelby, C.W.A. Newey, P.L. Pratt and A.B. Lidiard, "Charged Dislocations and Strength of Ionic Crystals," Phil. Mag. 8[3] 75-89 (1958).

12. K.L. Kliewer, "Space Charge in Ionic Crystals - III. Silver Halides Containing Divalent Cations," J. Phys. Chem. Solids 27 705-717 (1966).

13. S.M. Sze, Physics of Semiconductor Devices, J. Wiley and Sons, New York, 1981.

14. E.J.W. Verwey and J.Th.G. Overbeek, Theory of the Stability of Lyophobic Colloids, Elsevier, New York, 1948.

15. K.L. Kliewer and J.S. Koehler, "Space Charge in Ionic Crystals. I. General Approach with Application to NaCl," Phys. Rev. 140[4a] A1226-A1240 (1965).

16. J.M. Blakely and S. Danyluk, "Space Charge Regions at Silver Halide Surface: Effects of Divalent Impurities and Halogen Pressure," Surf. Sci. 40[1] 37-60 (1973).

17. M.F. Yan, R.M. Cannon and H.K. Bowen, "Space Charge, Elastic Field and Dipole Contributions to Equilibrium Solute Segregation at Interfaces," J. Appl. Phys. 54[2] 764-778 (1983).

18. Y.-M. Chiang, A.F. Henriksen, W.D. Kingery and D. Finello, "Characterization of Grain-Boundary Segregation in MgO," J. Am. Ceram. Soc. 64[7] 387-389 (1981). et al., 1982.

19. D. McLean, Grain Boundaries in Metals, Clarendon Press, Oxford, 1957.

20. O. Stern, Z. Elektrochem. 30 508 (1924).

21. R.B. Poeppel and J.M. Blakely, "Origin of Equilibrium Space Charge Potentials in Ionic Crystals," Surf. Sci. 15[2] 507-523 (1969).

22. D.M. Duffy and P.W. Tasker, "A Calculation of the Interaction between Impurity Ions and Grain Boundaries in NiO," Phil. Mag. A 50[2] 155-169 (1984).

23. K. Luecke and K. Detert, "A Quantitative Theory of Grain Boundary Motion and Recrystallization in Metals in the Presence of Impurities," Acta Met. 5[11] 628-637 (1957).

24. E.S. Machlin, "Theory of Solute Atom Limited Grain Boundary Migration," Trans. AIME 224 1153 (1962).

25. J.C.M. Li, "High Angle Tilt Boundary - A Dislocation Core Model," J. Appl. Phys. 32 525 (1961).

26. E.P. Abraham, Surfaces and Interfaces II, J.J. Burke, N.L. Reed and V. Weiss, Eds., Syracuse University Press, p. 452, 1967.

27. R.A. Oriana, Acta Met. 7 62 (1959).

28. M. Hillert and B. Sundman, "A Treatment of the Solute Drag on Moving Grain Boundaries and Phase Interfaces in Binary Alloys," Acta Met. 24[3] 731-743 (1976).

29. M.F. Yan, "Grain Boundary Mobility of KCl," Sc.D. Thesis, M.I.T. (1976).

30. G.F. Bolling and W.C. Winegard, "Grain Growth in Zone-Refined Lead," Acta Met. 6[4] 283-287 (1958); and "Some Effects of Impurities on Grain Growth in Zone-Refined Lead," Acta Met 6[4] 288-292 (1958).

31. J.W. Rutter and K.T. Aust, "Kinetics and Morphology of Precipitation of $AuPb_3$ from Pb(Au) Solid Solution," Trans. AIME 218[8] 682-688 (1960).

32. P. Gordon and R.A. Vandermeer, pp.205-266 in Recrystallization, Grain Growth and Textures," ASM, Metals Park, Ohio (1966).

33. D. Turnbull, "Theory of Grain Boundary Migration Rates," Trans. AIME 191 661-665 (1951).

34. E.E. Underwood, Quantitative Stereology, Addison-Wesley, Reading, Mass., 1970.

35. M. Hillert, "On the Theory of Normal and Abnormal Grain Growth," Acta Met. 13[3] 227-238 (1965).

36. R.J. Brook, "Impurity Drag Effect and Grain Growth Kinetics," Scripta Met. 2[7] 375-378 (1968).

37. R.J. Brook, "Pore and Grain Growth Kinetics," J. Am. Ceram. Soc. 52[6] 339-340 (1969).

38. K.W. Lay, "Grain Growth in UO_2-Al_2O_3 in the Presence of a Liquid Phase," J. Am. Ceram. Soc. 51[7] 373-376 (1968).

39. T.J. Gray, pp.77-101 in High Temperature Oxides, Vol.5, Part IV, ed. A.M. Alper, Academic Press, New York, 1971.

40. H. Jagodzinski and H. Saalfeld, "Kationenverteilung und Strukturbeziehungen in Mg-Al-Spinellen", Z. Kristallographie, 110, 197-218 (1958).

41. N.W. Grimes, "Off-Centre Ions in Compounds with Spinel Structure", Phil. Mag., 26, 1217-26 (1972).

42. N.W. Grimes, "Antiferroelectricity among Compounds with Spinel Structure?", J. Phys. C, 6, L78-L79 (1973).

43. L. Hwang, A.H. Heuer and T.E. Mitchell, "On the Space Group of $MgAl_2O_4$ Spinel", Phil. Mag., 28, 241-243 (1973).

44. A.H. Heuer and T.E. Mitchell, "Further discussion on the Space Group of Spinel, J. Phys. C, 8, L541-L543 (1975).

45. E.J. Samuelson, "Note on the Space Group of Magnetite", J. Phys. C, 7, L115-L117, (1974).

46. C. Infante and B.E.F. Bender, "Off-Centre Displacements in Spinels: a Neutron Diffraction Examination of $MgCr_2O_4$", J. Phys. C, 6, L333-L336, (1973).

47. E. J. Samuelson and O. Steinsvoll, "On the Space Group of Spinel", J. Phys. C, 8, L427-L429 (1975).

48. J.W. Steeds and N.S. Evans, "Practical Examples of Point and Space Group Determination in Convergent Beam Diffraction," pp. 188-191, Proc. 38th Annual EMSA Meeting, ed. G.W. Bailey, Claitors Publishing Division, Baton Rouge, LA, 1980.

49. R.K. Mishra and G. Thomas, "Structural Phase Transition in the Spinel $MgAl_2O_4$", Acta Cryst., A33, 678 (1977).

50. I. Suzuki and M. Kumazawa, "Anomalous Thermal Expansion in Spinel $MgAl_2O_4$", Phys. Chem. Minerals, 5, 279-284 (1980).

51. D.M. Roy, R. Roy and E.F. Osborn, "The System $MgO-Al_2O_3-H_2O$ and Influence of Carbonate and Nitrate Ions on the Phase Equilibria", Am. J. Sci., 251, 337-361 (1953).

52. A.M. Alper, R.N. McNally, P.H. Ribbe and R.C. Doman, "The System $MgO-MgAl_2O_4$", J. Am. Ceram. Soc., 45[6], 263-268 (1962).

53. E. Sonder, "Ionic Transference Numbers and Electrical Conduction in $MgAl_2O_4$ Spinel," J. Am. Ceram. Soc. 66[1] 50-53 (1983).

54. D. Sempolinski, "The High Temperature Electrical Properties of Single Crystalline Magnesium Oxide," Sc. D. thesis, MIT, 1979.

55. J.L. Bates and J.E. Garnier, "Electrical Conductivity of $MgAl_2O_4$ and $Y_3Al_5O_{12}$," J. Am. Ceram. Soc. 64 C138-C141 (1981).

56. a) R.A. Weeks and E. Sonder, "Electrical Conductivity of Pure and Fe-Doped Magnesium-Aluminum Spinel," J. Am. Ceram. Soc. 63[1-2] 92-95 (1980).

b) E. Sonder and L.S. Darken, "The Influence of Cation Stoichiometry on the Electrical Conductivity and High-Temperature Stability of $MgO.nAl_2O_3$ Spinel," presented at the Annual Meeting of the Materials Research Society, Boston, Mass., 1983.

57. H. Schmalzreid, Solid State Reactions, 2nd Ed., Verlag Chemie, Weinheim, W. Germany, 1981, Chapter 5, and Z. phys. Chem. NF 105 47 (1977).

58. R. Lindner and A. Akerstroem, "Diffusion von Ni-63 in Nickelspinellen," Z. Physik. Chem. N. F. 18 303-307 (1958).

59. M. Halbwachs, P. Mazot, J. Woirgard, P. Veyssiere, "Investigation of the Composition Dependence on Internal Friction Spectra in the $MgAl_2O_4$-Al_2O_3 Gamma Spinel System," Rad. Effects 75 173-182 (1983).

60. G. Yamaguchi, M. Nakano and M. Tosaki, "Effects of Cation Vacancies of the Diffusion of Nickel Ions in Defective Spinels," Bull. Chem. Soc. Japan 42 2801-2807 (1969).

61. R. Dieckmann and H. Schmalzreid, "Defects and Cation Diffusion in Magnetite (I)," Ber. Bunsenges Physik. Chem. 81[3] 344-347 (1977).

62. Y. Oishi and K. Ando, "Self-Diffusion of Oxygen in Polycrystalline $MgAl_2O_4$," J. Chem. Phys. 63[1] 376-378 (1975).

63. K. Ando and Y. Oishi, "Self-Diffusion Coefficients of Oxygen Ion in Single Crystals of $MgO.nAl_2O_3$ Spinels," J. Chem. Phys. 61[2] 625-630 (1974).

64. K.P.R. Reddy and A.R. Cooper, "Oxygen Diffusion in Magnesium Aluminate Spinel," J. Am. Ceram. Soc. 64[6] 368-371 (1981).

65. K. Ando and Y. Oishi, "Effect of Ratio of Surface Area to Volume on Oxygen Self-Diffusion Coefficients Determined for Crushed MgO-Al_2O_3 Spinels," J. Am. Ceram.

Soc. 66[8] C131-C132 (1983).

66. R.J. Bratton, "Sintering and Grain Growth Kinetics of $MgAl_2O_4$," J. Am. Ceram. Soc. 54[3] 141-143 (1971).

67. M. Matsui, T. Takahashi and I. Oda, "Influence of MgO Vaporization on the Final Stage Sintering of MgO-Al_2O_3 Spinel," to appear in Advances in Ceramics.

68. S. Hafner and F. Laves, "Ordnung/Unordnung und Ultrarotabsorption, III. Die Systeme $MgAl_2O_4$-Al_2O_3 und $MgAl_2O_4$-$LiAl_5O_8$", Z. Kristallographie, 115, 321-330 (1961).

69. E. Brun and S. Hafner, "Die Elektrische Quadrupolaufspaltung von Al^{27} in Spinell $MgAl_2O_4$ und Korund Al_2O_3", Z. Kristllographie, 117, 37-62 (1962).

70. E. Stoll, P. Fischer, W. Haelg and G. Maier, "Redetermination of the Cation Distribution of Spinel ($MgAl_2O_4$) by Means of Neutron Diffraction", J. Physigue, 25, 447-448 (1964).

71. U. Schmocker, H.R. Boesch and F. Waldner, "A Direct Determination of Cation Disorder in $MgAl_2O_4$ Spinel by ESR", Phys. Lett., 40A[3], 237-238 (1972).

72. U. Schmocker and F. Waldner, "The Inversion Parameter with Respect to the Space Group of $MgAl_2O_4$ Spinels", J. Phys. C, 9, L235-L237 (1976).

73. H. Schmalzreid, "Roentgenographische Untersuchung der Cationenverteilung in Spinellphasen," Z. Phys. Chem. N. F., 28 203-219 (1961).

74. H. Schmalzreid, "Point Defects in Ternary Ionic Crystals", pp.265-303 in Progress in Solid State Chemistry, Vol. 2, ed. H. Reiss, Pergamon Press, New York, 1964.

75. A. Navrotsky and O.J. Kleppa, "The Thermodynamics of Cation Distributions in Simple Spinels", J. Inorg. Nucl. Chem., 29, 2701-2714 (1967).

76. R.F. Cooley and J.S. Reed, "Equilibrium Cation Distribution in $NiAl_2O_4$, $CuAl_2O_4$, and $ZnAl_2O_4$ Spinels," J. Am. Ceram. Soc., 55[8] 395-398 (1972).

77. H.B. Callen, S.E. Harrison, C.J. Kriessman, "Cation Distributions in Ferrospinels. Theoretical," Phys. Rev., 103[4] 851-856 (1956).

78. H.St.C. O'Neill and A. Navrotsky, "Simple Spinels: Crystallographic Parameters, Cation Radii, Lattice Energies, and Cation Distribution", Am. Miner., 68, 181-194 (1983).

79. R.K. Datta and R. Roy, "Stability of Ni_2TiO_4,", Z. Kristall., 121 410-417 (1965).

80. C.C. Wu and T.O. Mason, "Thermopower Measurement of Cation Distribution in Magnetite," J. Am. Ceram. Soc., 64[9] 520-522 (1981).

81. J.E. Grover and P.M. Orville, "The Partitioning of Cations Between Coexisting Single- and Multisite Phases with Application to the Assemblages: Orthopyroxene-Clinopyroxene and Orthopyroxene-Olivine," Geochim. Cosmochim. Acta, 33 205-206 (1969).

82. T.O. Mason and H.K. Bowen, "Electronic Conduction and Thermopower of Magnetite and Iron-Aluminate Spinels," J. Am. Ceram. Soc. 64[4] 237-242 (1981).

83. T.O. Mason and H.K. Bowen, "Cation Distribution and Defect Chemistry of Iron-Aluminate Spinels," J. Am. Ceram. Soc. 64[2] 86-90 (1981).

84. R. Dieckmann and H. Schmalzreid, "Point Defects and Cation Diffusion in Magnetite," Z. Physik. Chem. N. F. 96 331-333 (1975).

85. R. Dieckmann, T.O. Mason, J.D. Hodge, and H. Schmalzreid, "Defects and Cation Diffusion in Magnetite (III), Tracerdiffusion of Foreign Tracer Cations as a Function of Temperature and Oxygen Potential," ibid 82 778-783 (1978).

86. W.T. Petuskey, "Interdiffusion and Thermal Migration in Iron-Aluminate Spinels," Sc.D. thesis, M.I.T. (1977).

87. H.-G. Sockel and H. Schmalzreid, Ber. Bunsenges. Physik. Chem. 72 745 (1968).

88. R. Dieckmann and H. Schmalzreid, "Defects and Cation Diffusion in Magnetite (II)," ibid 81[4] 414-419 (1977).

89. W.H. Gourdin and W.D. Kingery, "The Defect Structure of MgO Containing Trivalent Cation Solutes: Shell Model Calculations," J. Mat. Sci. 14 2053-2073 (1979).

90. C.R.A. Catlow, R. James, W.C. Mackrodt and R.F.

Stewart, "Defect Energetics in α-Al_2O_3 and Rutile TiO_2," Phys. Rev. B 25[2] 1006-1026 (1982).

91. J.M. Daniels and A. Rosenzwaig, "Moessbauer Spectroscopy of Stoichiometric and Nonstoichiometric Magnetite," J. Phys. Chem. Solids 30[6] 1561-1571 (1969).

92. A.F. Henriksen, "Precipitation in MgO", Sc.D. thesis, M.I.T., 1978.

93. R.J. Bratton, "Initial Sintering Kinetics of MgAl2O4," J. Am. Ceram. Soc. 52[8] 417-419 (1969).

94. S.L.Dole, R.W. Scheidecker, L.E. Shiers, M.G. Berard, O. Hunter, Jr., "Techniques for Preparing Highly Sinterable Oxide Powders", Ames Laboratory, ERDA and Dept. Mat. Sci. and Eng., Iowa State University, unpublished report.

95. R.D. Bagley, unpublished data.

96. C.C. Wang, "Growth and Characterization of Spinel Single Crystals for Substrate Use in Integrated Electronics", J. Appl. Phys., 40[9], 3433-44 (1969).

97. G. Yamaguchi, M. Nakano, M. Tosaki, "Effects of Cation Vacancies on the Diffusion of Nickel Ions in Defective Spinels", Bull. Chem. Soc. Japan, 42[10], 2801-07 (1969).

98. B.D. Cullity, Elements of X-ray Diffraction, Addison-Wesley, Reading, Mass., 1978?, pp.367-68.

99. D.P. Birnie III and W.D. Kingery, "Rapid Quenching of Solid Ceramics," to appear in Rev. Sci. Inst.

100. R.L. Fullman, "Measurements of Particle Sizes in Opaque Bodies," Trans. AIME 191[3] 447-452 (1953).

101. J.B. VanderSande and E.L. Hall, "Applications of Dedicated Scanning Transmission Electron Microscopy to Nonmetallic Materials," J. Am. Ceram. Soc. 62[5-6] 246-254 (1979).

102. J.B. VanderSande, A.J. Garrett-Reed, T. Thorvaldsson, and Y.-M. Chiang, "Resolving Composition Variations at Interfaces by STEM," to appear in Ultramicroscopy.

103. L.D. Marks, "Electron Wavepacket Diffraction", to

appear in Acta Cryst.

104. C.A. Parker, "Fast Neutron and Electron Irradiation Damage in Magnesium Aluminate and Aluminum Oxynitride Spinels", Ph. D. thesis, M.I.T., 1984.

105. L.W. Hobbs, pp.437-480 in Introduction to Analytical Electron Microscopy, editors J.J. Hren, J.I. Goldstein, D.C. Joy, Plenum Press, New York, 1979.

106. L.W. Hobbs, "Radiation Effects in Analysis by TEM," Quantitative Electron Microscopy, eds. J.N. Chapman and A.J. Craven, SUSSP Publications Vol. 25, University of Edinburgh, Edinburgh, Scotland, 1983.

107. M.L. Knotek and P.J. Feibelman, "Stability of Ionically Bonded Surfaces in Ionizing Environments," Surf. Sci. 90 78-90 (1979).

108. J.I. Goldstein, Ch. 3 in Introduction to Analytical Electron Microscopy, eds. J.J. Hren, J.I. Goldstein and D.C. Joy, Plenum Press, New York, 1979.

109. J.I. Goldstein, J.L. Costley, G.W. Lorimer and S.J.B. Reed, SEM/1977, ed. O. Johari, IITRI, Chicago, Ill., p. 315.

110. B.L. Bracewell and W.J. VEigele, "Tables of X-ray Mass Attenuation Coefficients for 87 Elements at Selected Wavelenghts," Develop. Appl. Spectrosc. 9 357-400 (1971).

111. D.F. Kyser, Ch. 6 in ref. 108.

112. B. Bender, D.B. Williams and M.R. Notis, "Investigation of Grain-Boundary Segregation in Ceramic Oxides by Analytical Scanning Transmission Electron Microscopy," J. Am. Ceram. Soc. 63[9-10] 542-546 (1980).

113. E.L. Hall, D. Imeson and J.B. VanderSande, "On Producing High-Spatial-Resolution Composition Profiles via Scanning Transmission Electron Microscopy," Phil. Mag. A 43[6] 1569-1585 (1981).

114. P. Doig and P.E.J. Flewitt, J. Microscopy 110 107 (1977).

115. M.F. Yan, R.M. Cannon and H.K. Bowen, "Grain Boundary Migration in Ceramics," pp.276-307 in Ceramics Microstructures '76, R.M. Fulrath and J.A. Pask, Eds., Westview Press, Boulder, Colorado.

116. R.M. Cannon, unpublished work, 1980.

117. D.M. Duffy and P.W. Tasker, "A Calculation of the Interaction between Impurity Ions and Grain Boundaries in NiO," Phil. Mag. A 50[2] 155-169 (1984).

118. K. Kitazawa, T. Arima, N. Bessho, Y. Saito, K. Fueki and T. Mukaibo, "Effect of Solutes on Grain Boundary Migration Kinetics in KCl Bicrystals," Sci. Sint., 10[1] 27-33 (1978).

119. W.D. Kingery, H.K. Bowen and D.R. Uhlmann, Introduction to Ceramics, p.141, Wiley Interscience, New York, 1976.

120. M.F. Yan, R.M. Cannon, H.K. Bowen and R.L. Coble, "Grain Boundaries and Grain Boundary Mobility in Hot-Forged Alkali Halides," pp.549-569 in Deformation of Ceramic Materials, R.C. Bradt and R.E. Tressler, Plenum Press, New York, 1975.

121. D.M. Duffy and P.W. Tasker, "A calculation of the formation energies of intrinsic defects near grain boundaries in NiO," Phil. Mag. A 50[2] 143-154 (1984).

122. P.M. Kelly, A. Jostsons, R.G. Blake and J.G. Napier, "The Determination of Foil Thickness by Scanning Transmission Electron Microscopy," phys. stat. sol. (a) 31 771-780 (1975).

123. S.M. Allen, "Foil Thickness Measurements from Convergent Beam Diffraction Patterns," Phil. Mag. A 43[2] 325-335 (1981).

Biographical Note

The author was born in 1958 near Taipei, Taiwan, and immigrated with his parents to the United States in 1964. He was raised and educated in the Northeast, and has become almost completely naturalized. After graduating in 1976 from Simsbury High School in Simsbury, Connecticut, he attended M.I.T., receiving the S. B. degree in Materials Science and Engineering in 1981. Feeling inspired by undergraduate research experiences, he became a graduate student in Ceramics, and has since that time progressed towards the present degree under the supervision of Professor W. D. Kingery. He is presently author or co-author of seven scientific papers in ceramics related areas.

His non-professional interests include such mechanically inclined hobbies as motorcycling, auto repair, and wood and metal working. He is an avid and occasionally successful hunter and fisherman.